

**Quantitative Investigation of Stimulus-evoked Intrinsic Optical Signal Change in
Retinal Photoreceptors**

BY

YIMING LU

B.S., Tianjin University, 2011

M.S., Tianjin University, 2014

THESIS

Submitted as partial fulfillment of the requirements
for the degree of Doctor of Philosophy in Bioengineering
in the Graduate College of the
University of Illinois at Chicago, 2020

Chicago, Illinois

Defense Committee:

Xincheng Yao, Chair and Advisor
Dingcai Cao, Ophthalmology and Visual Sciences
John Hetling, Bioengineering
Dieter Klatt, Bioengineering
Thomas Royston, Bioengineering

ACKNOWLEDGEMENTS

First of all, I would like to express my sincere gratitude to Dr. Xincheng Yao for his instructions during my Ph.D. studies. His critical thinking and rigorous attitude towards scientific research deeply impress me. The way he designs and conducts projects and experiments sets valuable examples for me to learn from in my future researches.

I would also like to thank my committee, Dr. Dingcai Cao, Dr. John Hetling, Dr. Dieter Klatt, and Dr. Thomas Royston, for their valuable suggestions and instructions.

During my Ph.D. studies, my colleagues Dr. Taeyoon Son, Dr. Devrim Toslak, Minhaj Alam, Taehoon Kim, David Le, Guangying Ma and Mattia Castelnovo, and previous colleagues, Dr. Benquan Wang, Dr. Changgeng Liu, Dr. Yanan Zhi, Dr. Rongwen Lu, Dr. Qiuxiang Zhang and Jacopo Benedetti, offered me lots of help and guidance in both research and life.

Most importantly, I would like to thank my parents and Min Ni for their support and love. They always trust and encourage me and do their best to help me in every possible way. They give me the courage and confidence to face the challenges and help me walk through the hard times.

This dissertation was supported in part by R01EY023522, R01EY024628, P30EY001792, and Center for Clinical and Translational Science Pre-doctoral Education for Clinical and Translational Scientists Fellowship.

Y.L.

TABLE OF CONTENTS

CHAPTER I. INTRODUCTION.....	1
1.1 Background.....	2
1.1.1 Retina and photoreceptor	2
1.1.2 Phototransduction cascade.....	4
1.1.3 Electroretinogram	5
1.1.4 Intrinsic optical signal and transient retinal phototropism.....	6
1.1.5 Scanning laser ophthalmoscopy	10
1.1.6 Virtually structured detection.....	13
1.2 Overview of the dissertation research.....	16
1.2.1 Significance	16
1.2.2 Innovation	17
1.2.3 Specific Aims	19
1.2.4 Structure of the dissertation	20
CHAPTER II. STIMULUS-EVOKED OUTER SEGMENT CHANGES OCCUR BEFORE THE HYPERPOLARIZATION OF RETINAL PHOTORECEPTORS.....	22
2.1 Introduction	22
2.2 Materials and methods.....	24
2.2.1 Retinal preparation	24
2.2.2 System setup	25
2.2.3 Experimental procedure.....	26
2.2.4 Data analysis	27
2.3 Results	28
2.4 Discussion.....	34
2.5 Conclusion	36
CHAPTER III. COMPARATIVE STUDY OF WILD-TYPE AND RD10 MICE REVEALS TRANSIENT INTRINSIC OPTICAL SIGNAL RESPONSE BEFORE PHOSPHODIESTERASE ACTIVATION IN RETINAL PHOTORECEPTORS.....	38
3.1 Introduction	39
3.2 Materials and methods.....	41
3.2.1 Experimental setup	41
3.2.2 Sample preparation	42
3.2.3 Data processing.....	43
3.3 Results	44
3.4 Discussion.....	50

CHAPTER IV. LIGHT-INDUCED LENGTH SHRINKAGE OF ROD PHOTORECEPTOR OUTER SEGMENTS.....	53
4.1 Introduction	54
4.2 Methods	55
4.2.1 Sample preparation	55
4.2.2 Experimental setup	57
4.2.3 Image processing and data analysis.....	58
4.3 Results	60
4.3.1 Time-lapse light microscopy of rod OS shrinkage.....	60
4.3.2 Comparative histological study of the retina in dark- and light-adapted Eyes	62
4.3.3 Comparative TEM study of rod discs in dark- and light-adapted eyes	63
4.4 Discussion.....	66
CHAPTER V. <i>IN VIVO</i> SUPER-RESOLUTION IMAGING OF TRANSIENT RETINAL PHOTOTROPISM EVOKED BY OBLIQUE LIGHT STIMULATION	70
5.1 Introduction	70
5.2 Methods	72
5.3 Results	74
5.4 Discussion.....	79
CHAPTER VI. <i>IN VIVO</i> SUPER-RESOLUTION IMAGING OF HUMAN RETINA WITH VIRTUALLY STRUCTURED DETECTION	81
6.1 Introduction	81
6.2 Methods	83
6.3 Results	84
6.4 Discussion.....	89
CHAPTER VII. DISCUSSION AND CONCLUSION.....	92
7.1 Physiological origin of photoreceptor-LOS	92
7.2 Physical origin of photoreceptor-LOS.....	93
7.3 <i>In vivo</i> demonstration of TRP	94
7.4 <i>In vivo</i> super-resolution imaging of human retina.....	94
CITED LITERATURE	96
APPENDICES	105
VITA	120

CONTRIBUTION OF AUTHORS

Chapter II [1], IV [2] and V [3] are published manuscripts in which I was the primary author. I was responsible for experiment design, system development, data acquisition and processing, and manuscript preparation. Dr. Xincheng Yao supervised the projects and contributed to experiment design, data processing, and manuscript preparation. In Chapters II, Dr. Benquan Wang helped with experiment design and data processing. Dr. David Pepperberg helped with experiment design and manuscript preparation. In Chapter IV, Jacopo Benedetti helped with experiment design, data acquisition, and processing. In Chapter V, Dr. Changgeng Liu helped with experiment and imaging system design.

Chapter III is a manuscript submitted to Experimental Biology and Medicine and is under review. I contributed to experimental design, data acquisition and processing, and manuscript preparation. Taehoon Kim helped with experimental design and interpretation of the results. Dr. Xincheng Yao supervised this project and contributed to experimental design, data analysis, and manuscript preparation.

LIST OF TABLES

<u>Table</u>	<u>Page</u>
Table I. Means and standard deviations of the inter- and intra-disc distances measured from tip, middle and base regions of dark- and light-adapted rod photoreceptors	64

LIST OF FIGURES

<u>Figure</u>	<u>Page</u>
Fig. 1.1. Eye, retina, and photoreceptor	2
Fig. 1.2. Diagram of rod and cone outer segment	3
Fig. 1.3. Phototransduction cascade	5
Fig. 1.4. Standard ERGs recorded from dark-adapted (A) eyecup and (B) isolated retina	6
Fig. 1.5. IOS imaging in the retina	7
Fig. 1.6. TRP observed in living frog eyecup	9
Fig. 1.7. Schematic diagram of a SLO	11
Fig. 1.8. Schematic diagram of the line-scan SLO	12
Fig. 1.9. Schematic diagram of a VSD-based super-resolution SLO	16
Fig. 2.1. (A) Schematic diagram of the experiment setup. Left: A custom modified microscope with a 40X water immersion microscope and a CCD (100 fps) or a CMOS (500 fps) camera was employed for imaging. Right: The ERG recording was achieved by placing electrodes on the retina in a glass chamber (dashed square). The isolated retina was continuously superfused with physiological medium during the experiment. (B) The retina was placed with photoreceptor layer on the top and was obliquely (~20°) stimulated by visible light from the top [56]. The coordinate axes shown at the bottom were used to define the direction of ROS movement. The 90° direction represents ROS movement toward the incident stimulation	26

LIST OF FIGURES (continued)

<u>Figure</u>	<u>Page</u>
<p>Fig. 2.2. (A) Top: Representative microscopy images of ROSs acquired in intervals of 0.2 s. The white regions in the panels represent the stimulus pattern presentations. Bottom: The imaging period (5 s) had three phases: pre-stimulus (1 s), stimulus (1 s), and post-stimulus (3 s) phases. (B) Dynamic magnitude changes of ROS movements corresponding to the retinal images in A. Enlarged microscopy image of ROSs acquired at time 0.4 s (C) and the corresponding movement magnitude (D) and direction (E) maps. (F) Time course of the mean magnitude of ROS movements. (G) Full-field ERG recorded from the isolated retina. The shaded areas in F and G indicate the stimulus duration</p>	29
<p>Fig. 2.3. (A) Representative ROS image acquired at a frame speed of 500 fps. Time course of the averaged mean movement magnitudes of ROSs (B1), and averaged ERGs (C1) acquired from ten different retinal locations. (B2) Enlarged picture of the dashed square in B1. (C2) Enlarged picture of the dashed square in C1. The red triangles in B2 and C2 indicate the onset times determined by the 3-δ threshold of ROS movement and ERG a-wave, respectively. Each data point shown in C2 (sampling rate of the original data: 10 kHz) represents the value exhibited at the end of a given 2-ms interval. Gray areas in B1 and C1 show standard deviations. Shaded areas in B1, B2, C1, and C2 represent stimulation periods</p>	31

LIST OF FIGURES (continued)

<u>Figure</u>	<u>Page</u>
Fig. 2.4. Comparison of ROS movements and ERGs between control groups (superfusion with Ringer's medium) and the low-sodium group (superfusion with low-sodium medium)	32
Fig. 2.5. Averaged ROS movements (A) and ERGs (B) of control (A1, B1), low-sodium (A2, B2), and recovery (A3, B3) groups	34
Fig. 3.1. Schematic diagram of experiment setup	41
Fig. 3.2. (A) Representative microscopic images of a PN16 mouse retina acquired with a 0.5-s interval. The white rectangle in the second frame shows the visible stimulus pattern with a duration of 0.5s. (B) Temporal sequence of IOS maps corresponding to the data in (A). Each panel represents an average of all 50 IOS maps acquired during the 0.5-s interval indicated by the time axis at the bottom. (C) Enlarged single-frame IOS maps acquired after the onset of stimulus with an imaging speed of 100 frames/s. The time axis at the bottom indicates the acquisition time. (D) Time course of the mean magnitude of IOS responses. The shaded area indicates the stimulus duration. Scale bars represent 10 μm	44
Fig. 3.3. Comparison of IOS responses between WT and rd10 groups at P14 and P16	46
Fig. 3.4. Averaged IOS responses from WT and rd10 mice at P14 and P16 and the corresponding statistical characterization	47

LIST OF FIGURES (continued)

<u>Figure</u>	<u>Page</u>
Fig. 3.5. Averaged IOS maps acquired at 0.5 s after the onset of stimulus from WT and rd10 mice	49
Fig. 4.1. (A) Representative light microscopic images of a single isolated rod OS acquired with an interval of 0.5 seconds. To better show the light-evoked OS shrinkage, the base of the rod OS in each image is aligned horizontally as shown by the black solid line at the bottom. The black-dashed line at the top represents the position of the rod OS tip at time -1 second. Scale bars (in white) represent 5 μ m. (B) Enlarged picture of the white rectangle in A. Scale bars (in white) represent 2 μ m. (C) Time course of the averaged rod OS shrinkage in both length and diameter acquired from eight different rod OSs. Colored areas accompanying the curves represent the standard deviations. Shaded area indicates the 1-second stimulation period	61
Fig. 4.2. Histological images of eyecups from the dark-adapted eye (A), and the light-adapted eye (B)	63
Fig. 4.3. TEM study of rod OSs	65
Fig. 5.1. (a) Schematic of the line-scan ophthalmoscope for in vivo super-resolution imaging. The illumination for retinal imaging is produced by a SLD. The line profile of illumination scanned across the retina is produced by the cylindrical lens. L1–L4 are lenses with focal lengths of 80, 400, 80, and 25 mm, respectively. The black-dashed line represents the virtual optical axis for a perpendicular stimulation on the retina. The oblique stimulation is then achieved by applying	

an “off-axis” setup in the stimulation path. (b) Illustration of the oblique stimulation and retina: right-side view (left), front view (middle), and top view (right) of the oblique stimulation and retina. The black-dashed rectangles represent the imaging area on the photoreceptor layer of retina. (a) and (b) Share the same coordinates	72
Fig. 5.2. In vivo TRP evoked by a localized oblique stimulation	74
Fig. 5.3. Spatiotemporal dynamics of in vivo TRP evoked by localized oblique stimulation	76
Fig. 5.4. Characteristics of photoreceptor movement correlated with stimulation intensities	78
Fig. 6.1. Schematic diagram of the imaging system setup	83
Fig. 6.2. Comparative in vivo imaging of human photoreceptors	86
Fig. 6.3. (a) A representative VSD image with intra-frame distortions at the bottom of the image. Focus is at the photoreceptor layer. (b) The absolute retinal shift in each sub-frame image, with the first sub-frame image as a reference. (c) VSD image after the registration of intra-frame distortions. (d) Magnified view of the red-dashed rectangle in (a) to show the image distortions. (e) Magnified view of the blue-dashed rectangle in (b) to show the registration performance. Scanning direction was along Y-axis. Scale bars represent ~50 μm on retina	87
Fig. 6.4. Comparison of single-frame EWF and VSD images acquired at different retinal locations with focus at the photoreceptor layer	89

LIST OF ABBREVIATIONS

AMD	Age-related macular degeneration
AO	Adaptive optics
CCD	Charge-coupled device
cGMP	Cyclic guanosine monophosphate
DR	Diabetic retinopathy
ELM	External limiting membrane
TEM	Transmission electron microscope
ERG	Electroretinogram
FWHM	Full width half maximum
FOV	Field of view
GCL	Gangling cell layer
GMP	Guanosine monophosphate
ILM	Internal limiting membrane
INL	Inner nuclear layer
IOS	Intrinsic optical signal
IPL	Inner plexiform layer
IS	Inner segment
LED	Light emitting diode
NA	Numerical aperture
NFL	Nerve fiber layer
NIR	Near-infrared
OCT	Optical coherence tomography

ONL	Outer nuclear layer
OPL	Outer plexiform layer
OS	Outer segment
PD	Photodiode
PDE	Phosphodiesterase
PN	Postnatal day
rd10	Retinal degeneration 10
RP	Retinitis pigmentosa
RPE	Retinal pigment epithelium
SCE	Stiles-Crawford effect
SD-OCT	Spectral-domain optical coherence tomography
SLD	Superluminescent diode
SLO	Scanning laser ophthalmoscope
SNR	Signal-to-noise ratio
TRP	Transient retinal phototropism
VSD	Virtually structured detection
WT	Wild type

SUMMARY

Retinal photoreceptors are critical for the vision formation. Many eye diseases, such as age-related macular degeneration (AMD) and retinitis pigmentosa (RP), affect the physiology of photoreceptors at their early stage. As functional abnormalities can happen before the visible structural distortions, functional assessment of photoreceptors is important for early detection and treatment assessment of the eye diseases. Intrinsic optical signal (IOS) imaging of retinal photoreceptors measures the intrinsic optical property changes in the photoreceptors activated by visible light stimulation. In conjunction with advanced imaging technologies, such as scanning laser ophthalmoscopy (SLO) and optical coherence tomography (OCT), functional IOS imaging promises a noninvasive, objective assessment of photoreceptor functionality with high spatial and temporal resolution.

Photoreceptor-IOS has been demonstrated in multiple animal models and human eye with different optical imaging modalities. However, its physiological and anatomic principles have not been well understood. In our previous studies, the photoreceptor-IOS presented a rapid response after the onset of visible stimulation, indicating a close relationship with the early phases of phototransduction cascades that happen within the outer segment of photoreceptor. This dissertation research is designed to investigate the physiological and structural origin of the IOS-correlated photoreceptor outer segment changes and their spatiotemporal properties. Different optical imaging systems and experimental protocols were developed and utilized for this dissertation research.

To investigate the physiological origin of photoreceptor-IOS, comparative studies with low-sodium physiological medium perfusion were first performed on isolated retina

tissues. The low-sodium medium perfusion of the retina intervenes in the phototransduction cascade but retains its early phase, which happens on/near the discs in the outer segment. Time-lapsed light microscopy was employed to monitor the spatiotemporal dynamics of transient retinal phototropism (TRP), which is a major contributor of photoreceptor-IOS. The results showed that TRP persisted in the low-sodium medium perfusion and therefore suggested its physiological origin to the early phase of phototransduction which is before the hyper-polarization of photoreceptor membrane.

To further demonstrate the physiological origin of photoreceptor-IOS in the early phototransduction cascade, mouse model with retinal degeneration was employed to clarify the role of cyclic guanosine monophosphate (cGMP) phosphodiesterase (PDE) in the IOS formation. Photoreceptor-IOS responses in wild-type and retinal degeneration 10 (rd10) mice were compared at different post-natal days. The results showed that the spatial and temporal dynamics of photoreceptor-IOS were not affected by the PDE deficiency in rd10 mice, suggesting a physiological origin correlated to the activation of rhodopsin and/or transducin.

As the physiological studies indicated a disc-based origin of photoreceptor-IOS, transmission electron microscopy (TEM) was adopted to illustrate the structural differences in the disc and inter-disc space between the dark- and light-adapted rod photoreceptors. The statistical analysis showed that the inter-disc distance was significantly shorter in light-adapted samples while the intra-disc distances were similar in both dark- and light-adapted samples, indicating the reduction of the inter-disc space is the physical origin of the rod outer segment shrinkage.

In vivo TRP was further demonstrated in animal eyes by using a line-scan scanning laser ophthalmoscopy with a virtually-structured-detection (VSD) based super-resolution technology. The line-scan imaging modality and the VSD method facilitated an *in vivo* recording of photoreceptor activities with high temporal and spatial resolution. Our experiments showed that stimulus-evoked TRP can be clearly observed in living animal eyes. Further data analysis revealed that stimulation with higher intensity corresponded to a faster TRP response, in terms of onset time and time-to-peak. However, the peak magnitude of TRP was not significantly affected by the change in stimulation intensity.

To further investigate the IOS responses in human eye, an imaging technology with high spatial and temporal resolution is necessary considering the aberration and the involuntary movement of the human eye. A VSD-based super-resolution ophthalmoscope with a line-scan imaging modality was designed and constructed for *in vivo* human retinal imaging. Unambiguous identification of photoreceptor mosaic was achieved with cellular-level spatial resolution and millisecond-level temporal resolution. The results demonstrated that VSD-based super-resolution technology provides a compact and cost-efficient method for *in vivo* human retinal imaging and paves the road for the *in vivo* investigation of human IOS in the future.

In summary, the researches in this dissertation enhanced our understanding of IOS mechanisms, established a platform for further studies on human IOS, and provided insight for better instrument and stimulation protocol designs to pursue clinical applications of functional IOS imaging of retinal photoreceptors.

CHAPTER I. INTRODUCTION

Age-related macular degeneration (AMD) is a leading cause of vision loss in the United States. By 2020, there will be about 2.95 million people affected by AMD [4]. An early diagnosis of AMD is of great importance to preserve vision and save the medical costs. Currently, the clinical hallmark of AMD is the appearance of drusen in the retina [5,6]. However, it alone cannot provide enough information for the assessment of AMD and the healthiness of retina may have been affected at/near the lesion [7,8]. In principle, physiological disorders must occur in diseased cells, before detectable abnormalities of retinal morphology. A functional screening of retina can provide earlier diagnosis about the onset of AMD. Moreover, it has been demonstrated that AMD affects the retinal photoreceptors at its early stage [9]. Therefore, an objective assessment of photoreceptor functionality can enable an early diagnosis of AMD.

Conventional methods, such as electroretinogram and Amsler grid test, have limited spatial resolution and specificity of retinal functionality screening [10,11]. Intrinsic optical signal (IOS) of retinal photoreceptors reflects the intrinsic optical property changes, such as light scattering, polarization, and absorption fluctuation, in the photoreceptors activated by visible light stimulation [12,13]. Therefore, photoreceptor-IOS promises an objective and specific assessment of photoreceptor functionality. However, clinical application of IOS is still challenging as the mechanism of IOS is still not well clarified. Moreover, a convenient approach for high spatiotemporal resolution imaging of human photoreceptor morphology is still not clinically available. This dissertation research is designed to quantitatively investigate the physiological and anatomical mechanisms of the photoreceptor-IOS and develop a compact and cost-efficient method for human retinal

imaging with high spatiotemporal resolution. We expect the researches in this dissertation will contribute to the future clinical deployment of functional IOS imaging.

1.1 Background

1.1.1 Retina and photoreceptor

Retina is located at the back of the eye (Fig.1.1). It is almost transparent and has an overall thickness of ~150 - 300 μm in human eye. When the light enters the eye, it passes through the cornea, pupil, lens and focuses at the retina. Inside of retina, the photons go through the retinal nerve fiber layer (NFL), ganglion cell layer (GCL), inner plexiform layer (IPL), inner nuclear layer (INL), outer nuclear layer (ONL), outer plexiform layer (OPL), and arrive at the photoreceptor layer. Different retinal layers are formed by cell bodies and/or dendrites of different neurons, such as ganglion cell, amacrine cell, bipolar cell, horizontal cell, and photoreceptor. Each type of cell has its own function and the collaboration of them are necessary for the vision formation [14-16].

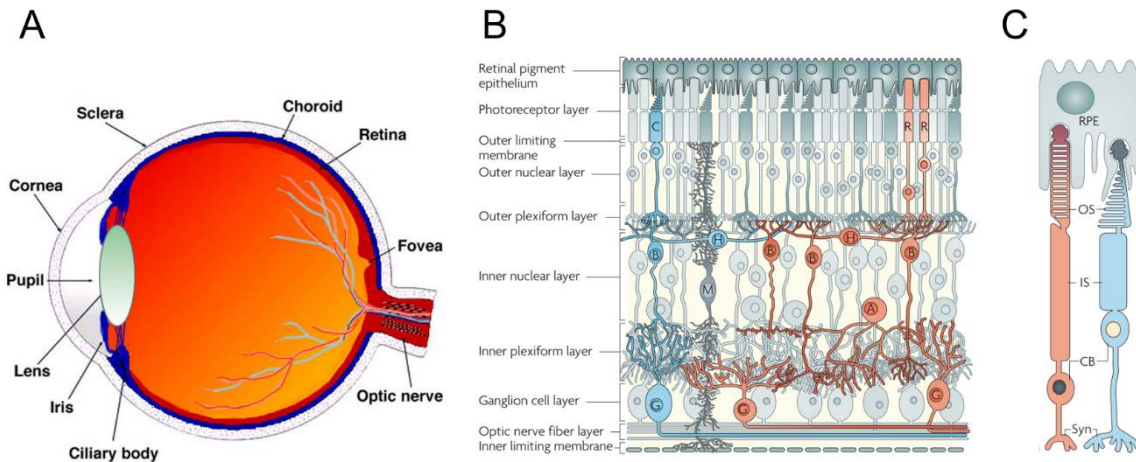


Fig.1.1. Eye, retina, and photoreceptor. (A) The anatomy of human eye. (B) Diagram of retina showing different retinal neurons and layers. (C) Two types of photoreceptor: rod and cone. The cell on the left is a rod and the one the left is a cone. OS: outer segment. IS: inner segment. CB: cell body. Syn: synapse. RPE: retinal pigment epithelium. The rod and cone outer segment are connected with the RPE cells. (A) is reprinted from [15] with permission. (B) and (C) are reprinted from [14] with permission.

The photoreceptor is the first step of vision formation. Photon energy is converted into electro-physiological signal by photoreceptors through the phototransduction cascade. There are two types of photoreceptor: rod and cone. The rod photoreceptors are sensitive to light and are responsible for the scotopic vision. While the cone photoreceptors are active at bright environment (photopic vision) and are responsible of color vision. In human eye, cones are also responsible for high spatial acuity of vision [16,17].

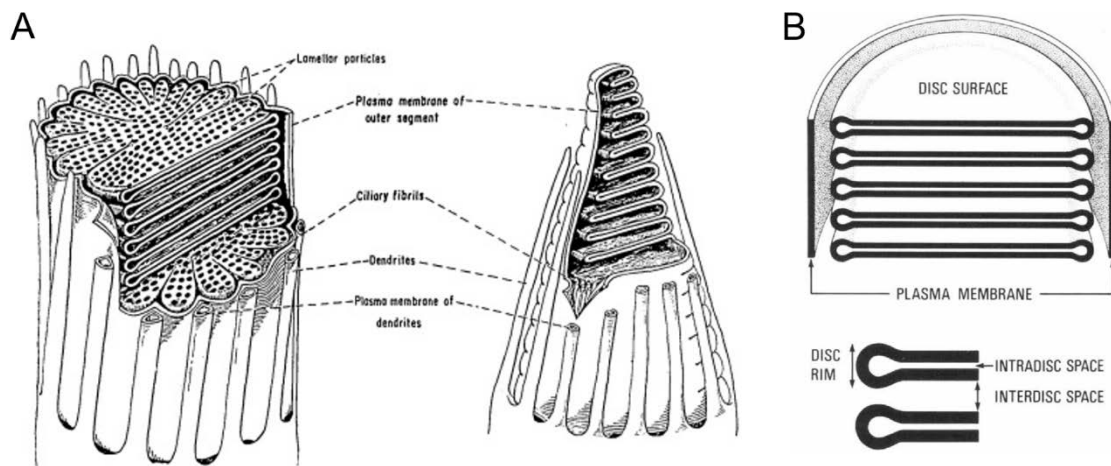


Fig.1.2. (A) Diagram of rod and cone outer segment. Left panel shows the inner structure of a rod outer segment. The rod outer segment is constructed of double-membrane disc stacks. Each disc is sealed off by an independent rim structure. The whole disc stack is enclosed in a plasma membrane continuous with that of the inner segment. In the cone, the lamellar structure is constructed by the repeated infoldings of the plasma membrane. (B) Diagram showing a cross-sectional view of the rod outer segment discs. The space within a disc is termed as intra-disc space. The space between two adjacent discs is termed as inter-disc space. (A) is reprinted from [18] with permission. (B) is reprinted from [19] with permission.

The photoreceptor structure contains outer segment, inner segment, cell body, and synapse. As shown in Fig.1.2, the rods and cones have different outer segment structures. The rod outer segment has a cylindrical shape and is filled with lamellar structure of discs. Each disc is an independent structure of lipid bilayer which is unconnected to the ciliary plasma membrane. The cone outer segment has a cone shape and the disc is formed by continuous membrane of the cilium that extends longitudinally over the outer segment

plasma membrane [19,20]. The outer segment discs carry visual pigments (rhodopsin for rod and cone opsins for cone) and other transduction proteins that are necessary for the phototransduction [18]. Both rod and cone inner segment contain mitochondria, ribosomes, and membranes where opsins are produced and transported to the outer segment discs. The cell body contains the nucleus of the photoreceptor cell. The synapses transmit the physiological signals of photoreceptors to second-order neurons, such as bipolar cells and horizontal cells [21].

1.1.2 Phototransduction cascade

The phototransduction cascade is a chain reaction that converts photon energy to electrophysiological signals. The overall process includes the sequential activation of rhodopsin, G-protein (transducin), and cyclic guanosine monophosphate (cGMP) phosphodiesterase (PDE) [22,23].

As shown in Fig. 1.3, the early phase of phototransduction cascade happens inside of the photoreceptor outer segments. In rod, when photons arrive at the outer segment, they first be absorbed by the rhodopsins which are embedded in the discs. The photon energy isomerizes the chromophore of the rhodopsin and activates rhodopsin as an enzyme (Step 1 in Fig.1.3). The activated rhodopsin diffuses and contacts with a G-protein (transducin) which is also embedded in the disc membrane. The G-protein is then activated, and its α -subunit is released and attached with a molecule of GTP from the cytoplasm (G_{α} -GTP). During the process, the activated status of rhodopsin is not altered by its interaction with G-protein. Therefore, it further interacts with multiple molecules of G-protein by diffusion while the rhodopsin is still active (Step 2 in Fig.1.3). The G_{α} -GTP then activates the PDE by binding to its regulatory γ -subunit (Step 3 in Fig.1.3). The

activated PDE hydrolyzes the cytoplasmic cGMP (Step 4 in Fig.1.3). The decrease of cGMP concentration leads to the closure of the cGMP-gated ion channels on the cell membrane, blocking the influx of ions (~85% Na^+ , rest are Ca^{2+} and Mg^{2+}), and the hyperpolarization of cell membrane (Step 5 in Fig.1.3). The alteration of membrane electrical potential status is transmitted to the inner segment, cell body, and synapses along the photoreceptor cell membrane. By receiving the electrical signal, the photoreceptor synapses release signaling proteins, i.e., glutamate, and thus deliver the electro-physiological signal to the next level neurons (e.g. bipolar cell) [22,24].

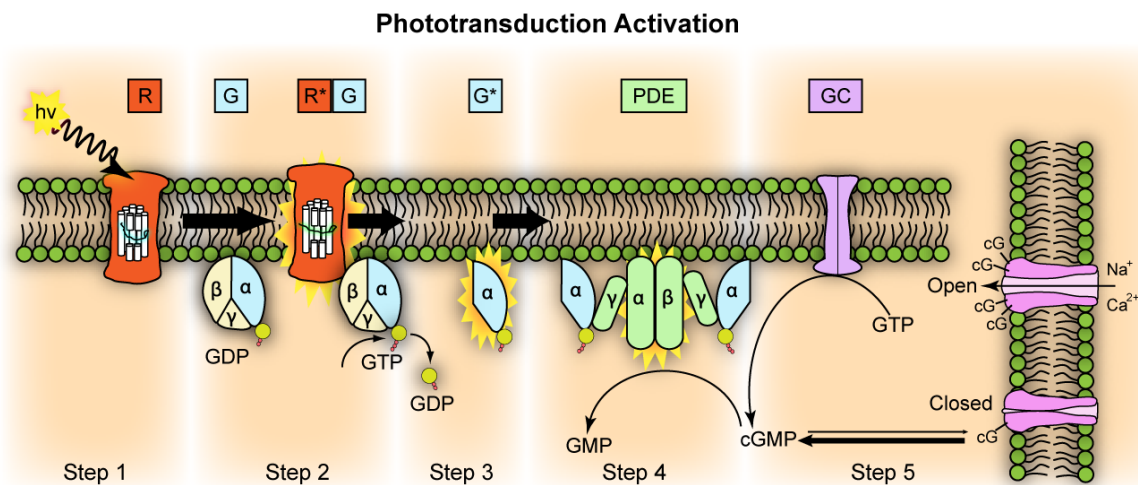


Fig.1.3. Phototransduction cascade. Step 1: Rhodopsin (R) is activated as R^* by absorbing a photon ($h\nu$). Step 2: R^* contacts molecules of the heterotrimeric G protein (G) and catalyzes the exchange of GDP for GTP. Step 3: The active form G -GTP (G^*) is produced. Step 4: Two G^* s bind to the γ subunits of PDE, thereby activating the hydrolysis of cGMP. Step 5: The consequent decrease in cytoplasmic concentration of cGMP leads to closure of the cGMP-gated ion channels and blockage of the inward flux of Na^+ and Ca^{2+} , resulting the hyperpolarization of cell membrane. Reprinted from [25] with permission.

1.1.3 Electroretinogram

Electroretinogram (ERG) records the electrical activities of the eye when a visible light stimulation is delivered to the eye [26]. It has been regarded as a golden standard of reflecting retinal physiology and widely used in clinics as a standard tool for the diagnosis

of various retinal diseases, e.g. AMD [27], retinitis pigmentosa (RP) [10,28], and congenital stationary night blindness [29]. A standard waveform of ERG is shown in Fig.1.4 [30]. The ERG waveform contains three major components, a-wave, b-wave, and c-wave. The ERG a-wave reflects in the hyperpolarization of photoreceptors [31,32]. The ERG b-wave reflects the cellular activities that are post-synaptic to the photoreceptors, majorly the depolarization of Müller cells [33,34]. The ERG c-wave is correlated with the activity of retinal pigment epithelial (RPE) cells [35].

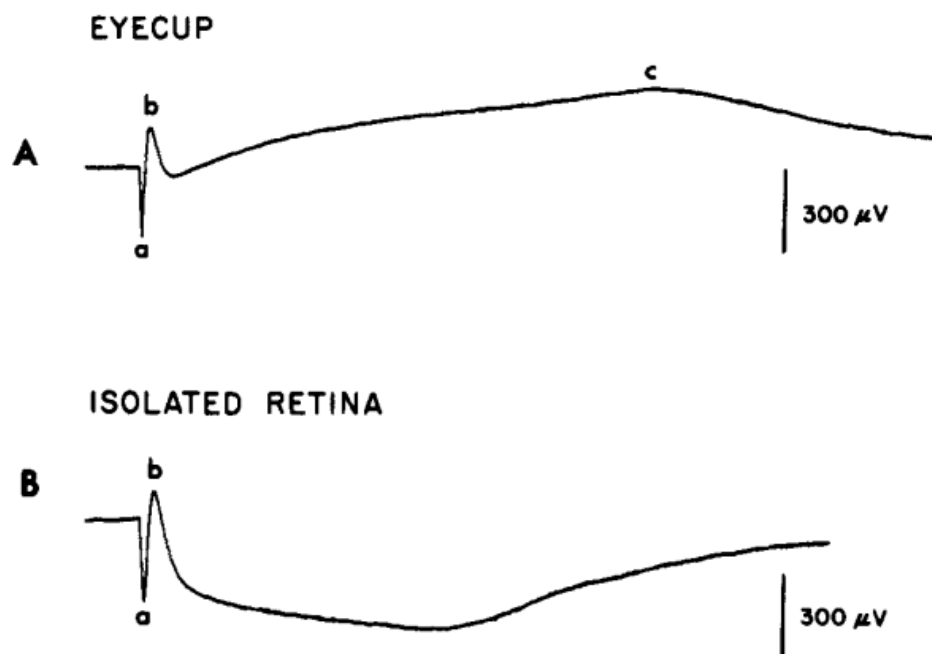


Fig.1.4. Standard ERGs recorded from dark-adapted (A) eyecup and (B) isolated retina, of skate eyes. ERG a-, b-, and c-wave can be identified. Reprinted from [30] with permission.

1.1.4 Intrinsic optical signal and transient retinal phototropism

Though ERG has been used as a valuable tool for monitoring the electro-physiology of retina, its spatial resolution and specificity are limited [10,36]. A reliable identification of localized retinal dysfunction/disease requires an objective assessment of retinal

physiology at a high resolution. The imaging of the stimulus-evoked intrinsic optical signal (IOS) promises an evaluation of retinal physiology at high spatiotemporal resolution. In principle, IOS reflects the stimulus-evoked optical property changes of biological tissue. For example, transient light scattering and birefringence changes, have been demonstrated in endocrine cells [37,38], brain cortex [39,40], and other neural tissues [41-43]. As IOS images are constructed through dynamic differentiation of time-lapse optical images recorded before, during and after the stimulation delivery, concurrent structural and functional assessment can be naturally achieved at a high spatiotemporal resolution. Retinal IOS has been observed in different animal models with different imaging modalities [44-48]. With the recent development of optical imaging technologies, such as optical coherence tomography (OCT) and scanning laser ophthalmoscopy (SLO), IOS has been demonstrated in human eye [49-51].

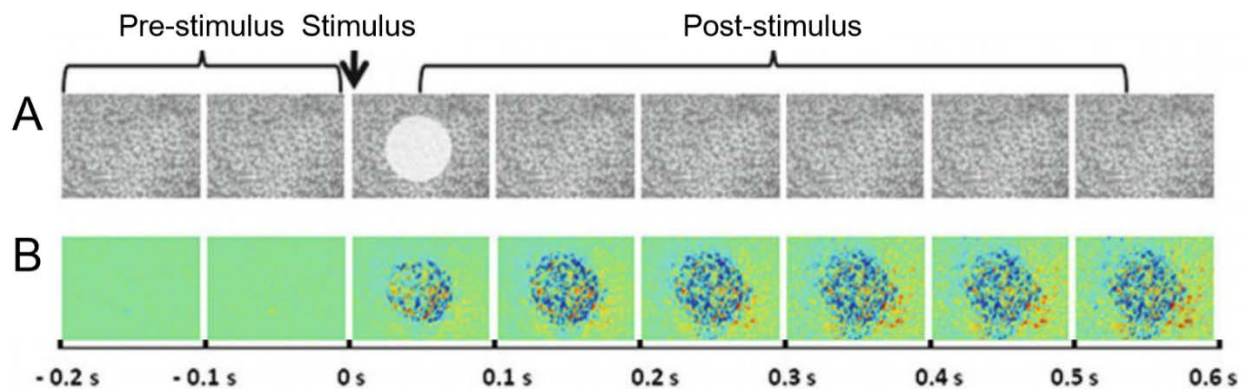


Fig.1.5. IOS imaging in the retina. (A) Time-lapse microscopic images of isolated retina. The recording trial contains three periods: pre-stimulus, stimulus, and post-stimulus phase. The white circle in the third frame shows the visible stimulus pattern. (B) Reconstructed IOS and images based on the raw images in (A). The blue and red color represents negative and positive IOS signals. Reprinted from [48] with permission.

Fig.1.5 shows representative retinal images and corresponding IOS maps. Detailed information of IOS processing can be found in our previous publications [48,52]. A brief description is presented here. For each recording trial of retinal images, it contains three

phases, a pre-stimulus phase, a stimulus phase, and a post-stimulus phase. The IOS can be processed based on the retinal images:

$$IOS_t(x, y) = \frac{\Delta I_t(x, y)}{\bar{I}_{pre}(x, y)} = \frac{I_t(x, y) - \bar{I}_{pre}(x, y)}{\bar{I}_{pre}(x, y)}$$

where $IOS_t(x, y)$ represents the IOS map with a frame index of t , $\bar{I}_{pre}(x, y)$ represents the mean intensity map of all images recorded during the pre-stimulus phase, and $I_t(x, y)$ is the retinal image with a frame index of t . A $3\text{-}\delta$ threshold and a temporal window filter were applied to suppress potential spatial and temporal noise contributions to the IOS map. For the $3\text{-}\delta$ threshold, a pixel with coordinate (x_k, y_k) in a retinal image $I_t(x, y)$ will be regarded as reflecting IOS when $I_t(x_k, y_k) > \bar{I}_{pre}(x_k, y_k) + 3 \cdot \delta_{pre}(x_k, y_k)$ or $I_t(x_k, y_k) < \bar{I}_{pre}(x_k, y_k) - 3 \cdot \delta_{pre}(x_k, y_k)$, where $\delta_{pre}(x_k, y_k)$ is the standard deviation of all pre-stimulus images. For the temporal window filter with an n -frame window size, $I_t(x_k, y_k) \cdots I_{t+n}(x_k, y_k)$ should consistently meet the $3\text{-}\delta$ threshold to include $I_t(x_k, y_k)$ for IOS calculation.

However, the inner mechanism of IOS is still not well clarified. In our previous studies, photoreceptor outer segment changes elicited by an oblique or unbalanced stimulation were observed in isolated retina, retinal slice and eyecup of animal models []. Such changes presented a general direction towards the stimulation. Therefore, it was termed as transient retinal phototropism (TRP). Fig.1.6 shows *in vitro* TRP observed in a living frog eyecup with OCT and an oblique stimulation. The magnitude and movement direction of the photoreceptor outer segments were quantified by using optical flow algorithm [53]. A robust TRP was observed within the stimulated retinal area and the direction of outer

segment distortions were consistent with the stimulation direction. Our further analysis showed that TRP is a predominant contributor of IOS [54,55].

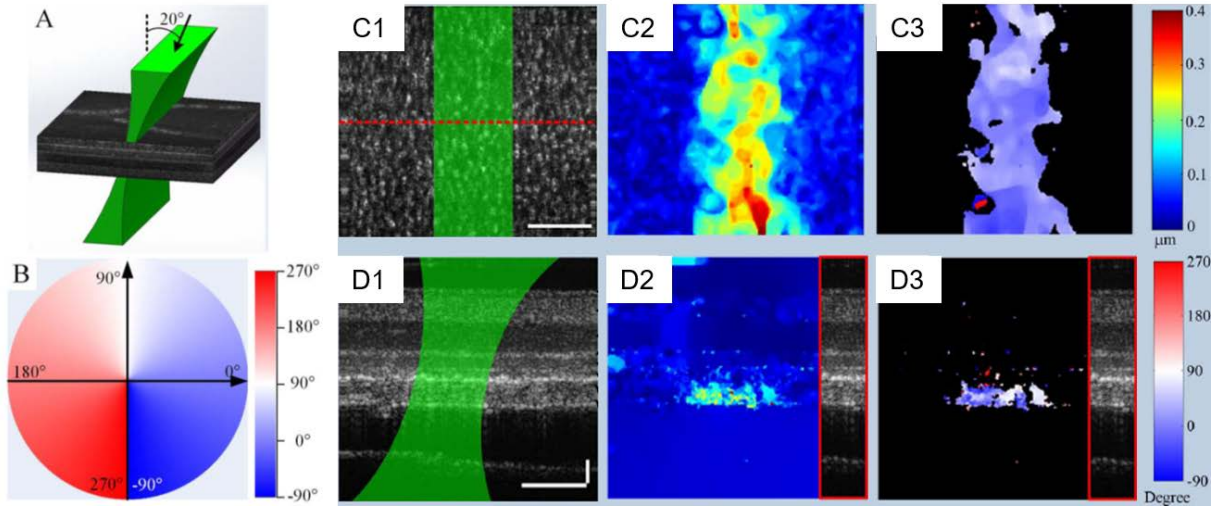


Fig.1.6. TRP observed in living frog eyecup. (A) An oblique stimulation with an angle of $\sim 20^\circ$ was delivered to the retina to elicit TRP. (B) The angle map of the TRP direction. (C1) *En face* view of the eyecup. (C2) TRP magnitude map corresponding to (C1). (C3) TRP direction map corresponding to (C1). (D1) OCT image of the retina. The imaging location is identified by the red dashed line in (C1). TRP (D2) magnitude map and (D3) direction map, corresponding to (D1). The green areas in (C1) and (D1) represent the oblique stimulation. Reprinted [56] from with permission.

In this dissertation, we further explored the physiological and anatomic mechanism of TRP-correlated outer segment changes with quantitative analysis. Different parameters including onset time, amplitude and time-to-peak were obtained from TRP temporal-magnitude curves and used for quantitative analysis of retinal physiological responses. The onset time is determined as the earliest time point when the corresponding TRP magnitude is larger than the $3\text{-}\sigma$ threshold. The amplitude is determined as the peak value of the TRP temporal-magnitude curve, which is generated by average all the TRP responses in the field of view (FOV), and the corresponding time point is determined as time-to-peak.

1.1.5 Scanning laser ophthalmoscopy

Scanning laser ophthalmoscopy (SLO) has been used to provide fundus photography with high spatial and temporal resolution. The basic structure of a SLO is shown in Fig. 1.7. The light source is usually a laser diode (LD), light-emitting diode (LED), or superluminescent laser diode (SLD). The illumination light generated by the light source goes through the collimator, relay lenses, a beam splitter, and arrives at the scanning mirror. The illumination light is then reflected by the scanning mirror and goes through another set of relay lens before reaching the eye. For a perfect eye, the parallel light formed by the ophthalmic lens (L4 in Fig. 1.7) focuses as a point on the retina. By controlling the relative angle of the scanning mirror, the illumination point will scan across a certain area of the retina, i.e., field of view (FOV). For a 2D scanning, usually a pair of scanning mirror is required to achieve the scanning in both X and Y direction. The reflected light from the retina is then de-scanned by the scanner before relayed to the image plane at the detector. Compared with conventional fundus camera, the illumination light is focused as a point at the sample plane. Therefore, the reflection light is majorly from the scanning point and the adjunct sample structures contribute minimum noise (scattering light) to the signal detection. Therefore, SLO can provide better contrast, signal-to-noise ratio (SNR), and spatial resolution [57].

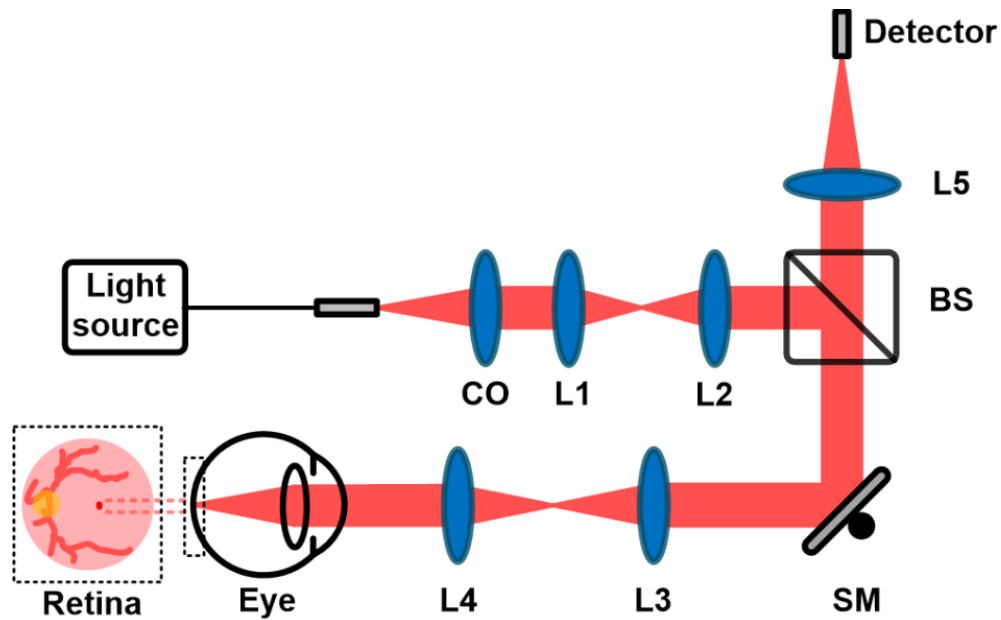


Fig. 1.7. Schematic diagram of a SLO. CO: collimator. L1 – L5: achromatic lenses. BS: beam splitter. SM: scanning mirror. The illumination light is focused as a point on the retina.

Human retinal imaging suffers from the eye movements. Usually, when performing the retinal imaging, the subject is required to look at a fixation target and maintain the stationary of eye. However, there are still involuntary eye movements that can cause severe image distortions. The most common involuntary eye movements are drifts (< 30 arcminutes/s ($\sim 150 \mu\text{m/s}$)), tremors ($40 - 100$ Hz) and microsaccades (~ 40 Hz) [58,59]. To solve the artifacts caused by the involuntary eye movements, improving imaging speed and employing image registration are two mostly used methods. As the highest frequency of involuntary eye movements is around 100 Hz, the retina images can be basically free from most of the eye movement-associated distortions when the imaging speed is ≥ 200 Hz, based on the Nyquist sampling law. For time-lapse recording of retinal images, image registration is also used to remove the position shift between individual images and facilitate a static FOV [60-62].

In this dissertation, a SLO based on a line-scan imaging modality was developed to achieve a fast imaging of retina (Fig. 1.8). Details of the system are introduced in Chapter VI. The near-infrared (NIR) illumination light is produced by a SLD with center wavelength at 830 nm. Because of the “NIR window” of biological tissue, the NIR light has relatively low absorption ratio before it reaches the retina. The SLD has an additional advantage of having the high power and the low coherence. The line-scan imaging modality is realized by using a cylindrical lens. The cylindrical lens focuses the illumination light into a single line instead of a focal point. Therefore, the imaging speed can be dramatically improved by scanning the illumination line across the retina. Correspondingly, a 2D CMOS camera, instead of a point detector, such as photodiode (PD) or photomultiplier tube (PMT), was used to record the reflect light from eye. The 2D camera is used to further facilitate the super-resolution imaging.

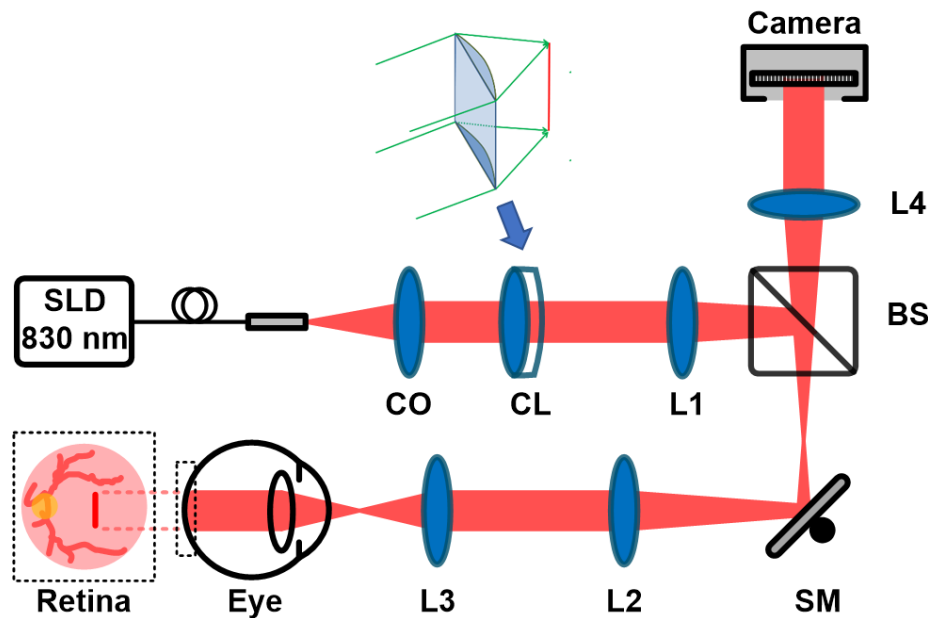


Fig. 1.8. Schematic diagram of the line-scan SLO. CO: collimator. CL: cylindrical lens. L1 – L5: achromatic lenses. BS: beam splitter. SM: scanning mirror. The cylindrical lens is used to condense the light into a focused line. The illumination line is swept across the retina by a scanning mirror.

1.1.6 Virtually structured detection

The virtually structured detection (VSD) based super-resolution technique originates from the structured illumination microscopy (SIM) [63,64]. In SIM, sinusoidal striped illumination patterns are projected onto the sample. The wide-field image of SIM can be expressed as:

$$p(x, y) = \{[h_{il}(x, y) \otimes m(x, y)]s(x, y)\} \otimes h_{de}(x, y) \quad (1)$$

where $p(x, y)$ is the SIM wide-field image, $h_{il}(x, y)$ and $h_{de}(x, y)$ are the point spread function (PSF) of the illumination and detection path, respectively, $m(x, y)$ represents the sinusoidal modulation function, \otimes represents convolution, and $s(x, y)$ represents the sample. In the frequency domain:

$$\tilde{p}(f_x, f_y) = \{[\tilde{m}(f_x, f_y)\tilde{h}_{il}(f_x, f_y)]\tilde{s}(f_x, f_y)\}\tilde{h}_{de}(f_x, f_y) \quad (2)$$

As the modulation function $m(x, y)$ has an expression of:

$$m(x, y) = 1 + \cos[2\pi f_0(x \cos \theta + y \sin \theta) + \alpha] \quad (3)$$

where f_0 is the carrier frequency of the modulation, θ and α are the rotation angle and constant phase of the modulation pattern, respectively. The corresponding Fourier transformation is:

$$\begin{aligned} \tilde{m}(f_x, f_y) = & \delta(f_x, f_y) + \frac{1}{2}\delta(f_x - f_0 \cos \theta, f_y - f_0 \sin \theta)e^{i\alpha} \\ & + \frac{1}{2}\delta(f_x + f_0 \cos \theta, f_y + f_0 \sin \theta)e^{-i\alpha} \end{aligned} \quad (4)$$

Therefore,

$$\begin{aligned} \tilde{p}(f_x, f_y) = & \tilde{h}_{il}(f_x, f_y) \left[\tilde{s}(f_x, f_y) + \frac{1}{2}\tilde{s}(f_x - f_0 \cos \theta, f_y - f_0 \sin \theta)e^{i\alpha} \right. \\ & \left. + \frac{1}{2}\tilde{s}(f_x + f_0 \cos \theta, f_y + f_0 \sin \theta)e^{-i\alpha} \right] \end{aligned} \quad (5)$$

the $\tilde{s}(f_x - f_0 \cos \theta, f_y - f_0 \sin \theta)$ and $\tilde{s}(f_x + f_0 \cos \theta, f_y + f_0 \sin \theta)$ in Equation (5) show that the high-frequency components of the sample $\tilde{s}(f_x, f_y)$, which are beyond the diffraction limit, are shifted into the passband of the optical imaging system. As additional frequencies are involved, the reconstructed sample images (through inverse Fourier transformation) present improved resolution. However, the illumination fringes of SIM are achieved by manipulating sophisticated mechanical grids with specific phases. During the SIM imaging, the sample is also required to be static to maintain a stable phase relationship. Therefore, a direct application of SIM to *in vivo* retinal imaging is challenging.

To overcome the problem, the VSD technique was proposed [65,66]. Different from conventional SIM, which is usually combined with wide-field microscopy, VSD is implemented with scanning imaging system, for example, SLM and OCT, and the modulation is realized in the detection beam digitally. Fig. 1.9 shows the VSD-based super-resolution SLM. The overall structure is similar with a conventional SLM. However, the reflection signal from the sample at each scanning point is recorded by a 2D camera, instead of a single-element detector (e.g. photodiode or photomultiplier tube), and stored as a sub-frame image. To achieve a sinusoidal intensity modulation, a digital mask is superimposed on each of the sub-frame image with a corresponding phase. The modulated sub-frame image can be expressed as:

$$I_{ms}(x, y; x_0, y_0) = I_s(x, y; x_0, y_0)m(x, y) \quad (6)$$

where $I_s(x, y; x_0, y_0)$ is the sub-frame image recorded from the scanning position (x_0, y_0) on the sample, and $I_{ms}(x, y; x_0, y_0)$ is the modulated sub-frame image by the digital mask $m(x, y)$. As the mask is superimposed digitally, the intensity modulation can be either positive or negative:

$$m(x, y) = \cos[2\pi f_0(x \cos \theta + y \sin \theta) + \alpha] \quad (7)$$

The modulated sub-frame images are then spatially integrated, and the values are assigned to the corresponding positions on the image plane:

$$p(x_0, y_0) = \iint I_{ms}(x, y; x_0, y_0) dx dy \quad (8)$$

Substituting Equation (6) to Equation (8), the image can be expressed as:

$$p(x, y) = h_{il}(x, y) \otimes \{[h_{de}(x, y) \otimes m(x, y)]s(x, y)\} \quad (9)$$

In frequency domain:

$$\begin{aligned} \tilde{p}(f_x, f_y) = \tilde{h}_{il}(f_x, f_y) & \left[\frac{1}{2} \tilde{s}(f_x - f_0 \cos \theta, f_y - f_0 \sin \theta) e^{i\alpha} \right. \\ & \left. + \frac{1}{2} \tilde{s}(f_x + f_0 \cos \theta, f_y + f_0 \sin \theta) e^{-i\alpha} \right] \end{aligned} \quad (10)$$

Therefore, the shifted sample spectrum $\tilde{s}(f_x - f_0 \cos \theta, f_y - f_0 \sin \theta)$ and $\tilde{s}(f_x + f_0 \cos \theta, f_y + f_0 \sin \theta)$ can be obtained by applying digital masks with two different phases, i.e., α_1 and α_2 . Compared Equation (9) with Equation (1), VSD image is equivalent to SIM image if $h_{il}(x, y)$ and $h_{de}(x, y)$ are assumed to be similar. Therefore, VSD technique can achieve a super-resolution imaging without using physical modulation methods. Moreover, the direct current component in Equation (5) is removed in Equation (10) thanks to the digital mask applied in VSD methods. The removal of the direct current component can significantly enhance the contrast and signal-to-noise ratio (SNR) [66].

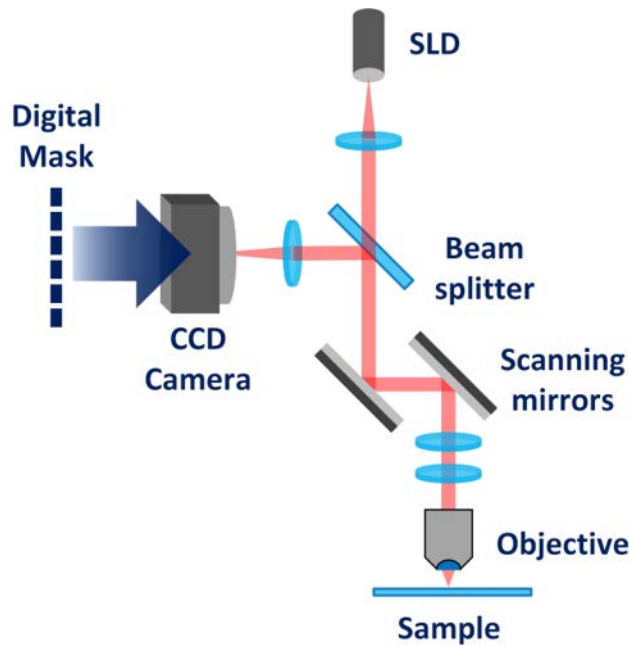


Fig. 1.9. Schematic diagram of a VSD-based super-resolution SLO. The illumination light is generated by a SLD and focused as a point on the sample. A pair of scanning mirror facilitates a scanning across the sample. The reflectance light is collected by the objective and delivered to a 2D camera. After acquiring the image of each scanning point, a digital mask is applied to each image for the VSD processing.

1.2 Overview of the dissertation research

1.2.1 Significance

Retinal photoreceptors are neurons in which phototransduction takes place and light is converted to electrophysiological signals. It is known that AMD can impair photoreceptors and cause vision loss. Therefore, early detection of AMD is critical to preserve photoreceptor function. Currently, the presence of structural distortions, such as drusen in the retinal pigment epithelium (RPE) and Bruch's membrane complex, are regarded as the clinical hallmark of AMD [6]. As physiological abnormalities can happen before physical distortions, a method that can assess the functionality of photoreceptors is more desirable for early diagnosis. Conventional psychophysical and electrophysiological methods, such as Amsler grid test, visual acuity test, and ERG, have limited signal

specificity and/or spatial resolution. Therefore, a high-resolution method for the objective examination of photoreceptor physiology is needed to advance early diagnosis of AMD.

The transient photoreceptor-IOS is reconstructed through high-resolution optical images of the retina using a dynamic differential method, reflecting the stimulus-evoked changes of the optical properties of the retina. Therefore, IOS imaging can naturally provide an objective assessment of photoreceptor functionality with high spatiotemporal resolution. Photoreceptor-IOS has been observed in many animal models and human retinas [46,48,50,51]. However, its mechanism has not been well clarified, which defers a clear plan to optimize the instrumental design and experimental protocol for the IOS imaging. Our previous animal studies demonstrated that stimulus-evoked morphological changes of photoreceptor outer segments could be an important contributor to the photoreceptor-IOS [52,54-56]. Therefore, this dissertation is designed to investigate the physiological and physical properties of photoreceptor-IOS and provide theoretical foundation and technical support for the future clinical applications.

1.2.2 Innovation

The innovativeness of this study is that it uses novel experimental designs, unique stimulation protocols, and multiple imaging modalities to investigate the mechanisms and properties of the photoreceptor-IOS.

(a) Comparative study of the physiological and anatomical origin of the light-induced photoreceptor-IOS: Low-sodium medium perfusion and a retinal degeneration mouse model were used to demonstrate the physiological origin of photoreceptor-IOS. Transmission electron microscopy (TEM) were used to demonstrate the origin of the light-induced photoreceptor structural change at nanometer-level for the first time. The low-

sodium medium perfusion of the retina intervenes in the phototransduction cascade but retains its early phase, which happens on/near the discs in the outer segment. Therefore, comparative studies between control and low-sodium medium perfusion group can demonstrate the physiological origin of photoreceptor-IOS. The retinal degeneration 10 (rd10) mouse model has a spontaneous PDE deficiency in the rod photoreceptors. Thus, the rd10 mouse model provides an opportunity to illustrate the role of PDE in the IOS formation. Comparative TEM studies were performed on dark- and light-adapted photoreceptors to determine the light-induced changes of the lamellar structure of discs at a subcellular level.

(b) *In vivo* demonstration of stimulus-evoked TRP: The stimulus-evoked structural changes of photoreceptors were observed *in vivo* for the first time. A fast VSD-based super-resolution ophthalmoscope was employed to provide unambiguous imaging of photoreceptors. To elicit TRP, the stimulation was obliquely delivered to the retina by using an off-axis setup of the stimulation path. The spatiotemporal properties of TRP were further investigated.

(c) *In vivo* super-resolution imaging of human retina: Human eye suffers from a strong aberration and a relatively low numerical aperture (NA). Thus, an unambiguous identification of retinal structures, such as photoreceptors, is challenging. The VSD-based technique provided a compact, cost-efficient and phase-artifact-free method for super-resolution imaging of human retina. A line-scan imaging modality was employed to improve the imaging speed and reduce the artifacts caused by human involuntary eye movements.

1.2.3 Specific Aims

Aim 1: To investigate the physiological and anatomical origins of the light-induced photoreceptor outer segment changes. This aim is to demonstrate the physiological correlation between the light-induced outer segment changes and phototransduction of rod photoreceptor, and the anatomical origin of the outer segment structural changes at a sub-cellular level. We employed perfusion with a low-sodium physiological solution to verify TRP when the rod outer segment membrane hyperpolarization, which is a step of phototransduction, was suppressed. Comparative photoreceptor-IOS experiments were performed between wild-type (WT) and rd10 mouse model. Quantitative analysis of the spatiotemporal distribution of photoreceptor-IOS responses in WT and rd10 mouse model was conducted to show the photoreceptor-IOS changes induced by the PDE deficiency. Transmission electron microscopy (TEM) was further adopted to illustrate the structural differences in the disc and inter-disc space between the dark- and light-adapted rod photoreceptors.

Aim 2: To demonstrate *in vivo* imaging of the transient retinal outer segment changes in an animal model. This aim is to verify the stimulus-evoked TRP in frog (*Rana pipiens*) eyes *in vivo*. An *in vivo* demonstration of TRP is necessary considering the difference between *in vitro* and *in vivo* environments may affect the observation/formation of TRP. We employed a virtually-structural-detection (VSD) based super-resolution ophthalmoscopy and a line-scan modality to provide an unambiguous identification of photoreceptors and a milli-second level temporal resolution. Oblique stimulations with various intensities and corresponding time-magnitude courses were used to illustrate the properties of *in vivo* TRP.

Aim 3: To demonstrate *in vivo* super-resolution imaging in human retina. This aim is to demonstrate a compact and cost-efficient method for *in vivo* imaging of human retina with high spatiotemporal resolution. To achieve a high spatial resolution, VSD technique was used to provide a super-resolution imaging of retina. To achieve a high temporal resolution that minimizes the artifacts caused by the involuntary eye movements (~100 Hz), a scanning laser ophthalmoscopy (SLO) with a line-scan imaging modality was employed to provide a fast imaging speed (>200 frames/s).

1.2.4 Structure of the dissertation

Five studies were designed and conducted in this dissertation research. The overall structure of this dissertation covers from fundamental biophysical studies and the *in vivo* experimental validations to investigate both the basic mechanisms and the technical feasibility of the *in vivo* imaging of the photoreceptor-IOS responses.

The study in Chapter II was designed to understand the phototransduction-correlated physiological origin of the stimulus-evoked TRP. Freshly isolated retinas were perfused with regular and low-sodium physiological medium, respectively. The hyperpolarization of the photoreceptor outer segments was successfully abolished by the low-sodium medium perfusion. But the TRP responses persisted. The experimental results and further data analysis indicate that the early phases of the phototransduction cascade, which occur prior to the hyperpolarization of photoreceptor outer segments, contribute to the TRP.

The study in Chapter III was designed to further locate the physiological origin of photoreceptor-IOS within the early, disc-based phototransduction cascade. Comparative studies between WT and rd10 mouse model show that the photoreceptor-IOS responses

were not significantly reduced in the rd10 retina, suggesting an earlier physiological origin of photoreceptor-IOS than the activation of PDE.

In Chapter IV, the anatomic origin of TRP was investigated by using TEM. As TEM can provide nanometer-level spatial resolution, the lamellar structure of outer segment discs was compared between light- and dark-adapted retinas. The statistic analysis reveals that the reduction of inter-disc distance, i.e., the space between discs, is correlated with the overall shrinkage of rod outer segment.

Chapter V presents the *in vivo* imaging of TRP in frog eye. An oblique stimulation was delivered to the retina to evoke the TRP, and a VSD-based super-resolution line-scan SLO was employed to monitor the retinal dynamics. The successful observation of *in vivo* TRP, on one hand, promises a biomarker for the functional assessment of photoreceptors, and on the other hand, demonstrates the feasibility of using VSD technique combined with a line-scan SLO to achieve a super-resolution of retinal structures.

The application of VSD technique and line-scan SLO was further pushed to human study in Chapter VI. A line-scan SLO system was constructed for human retinal imaging. The sub-frame images recorded by the two-dimensional (2D) camera further facilitated a registration of intra-frame distortions. With the VSD technique applied, photoreceptors can be clearly identified at different retinal locations.

Chapter VII summarized the studies in this dissertation and discussed future studies and clinical applications of the photoreceptor-IOS.

CHAPTER II. STIMULUS-EVOKED OUTER SEGMENT CHANGES OCCUR BEFORE THE HYPERPOLARIZATION OF RETINAL PHOTORECEPTORS

(Previously published as Yiming Lu, Benquan Wang, David R. Pepperberg, and Xincheng Yao, Stimulus-evoked outer segment changes occur before the hyperpolarization of retinal photoreceptors, Biomedical Optics Express 8, 38-47 (2017) [1])

Abstract: Transient retinal phototropism (TRP) has been predominantly observed in rod photoreceptors activated by oblique visible light stimulation. Dynamic confocal microscopy and optical coherence tomography (OCT) have revealed rod outer segment (ROS) movement as the physical source of TRP. However, the physiological source of ROS movement is still not well understood. In this study, concurrent near-infrared imaging of TRP and electroretinogram (ERG) measurement of retinal electrophysiology revealed that ROS movement occurs before the onset of the ERG a-wave, which is known to reflect the hyperpolarization of retinal photoreceptors. Moreover, substitution of normal superfusing medium with low-sodium medium reversibly blocked the photoreceptor ERG a-wave, but largely preserved the stimulus-evoked ROS movements. Our experimental results and theoretical analysis indicate that early, disc-based stages of the phototransduction cascade, which occur before the hyperpolarization of retinal photoreceptors, contribute to the TRP associated ROS movement.

2.1 Introduction

Transient retinal phototropism (TRP) has been observed in both amphibian (frog) and mammalian (mouse) retinas illuminated by oblique visible light [54]. High-resolution microscopy revealed that the TRP is dominated by rod photoreceptors. Functional optical

coherence tomography (OCT) located the anatomic source to rod outer segment (ROS) [56]. Our recent studies with retina slices, which enable a cross-sectional view of mouse and frog photoreceptors, confirmed the ROS movement as the physical mechanism of TRP [55]. This TRP provides a reasonable explanation for the Stiles–Crawford effect (SCE) [67] being predominantly observed in cones and not rods. In other words, the loss of luminous efficiency caused by oblique stimulation may be compensated by the phototropic movement of ROSs. Although the stimulus-evoked property of TRP indicates a cause-and-effect relationship between phototransduction and TRP, the physiological mechanism underlying TRP remains unclear. Previous studies of isolated ROS [68,69] and of isolated intact retina [70,71] have shown that in response to a visible flash, photoreceptors exhibit an intrinsic near-infrared scattering signal. As the ROS movement represents a morphological change in the retina, it is logical to hypothesize that the phototropic response of ROSs is a key component of the light-scattering signal [72], i.e., TRP may also originate from the ROSs. Our previous studies showed that the onset time of the intrinsic optical signal (IOS) precedes the onset time of the electroretinographic (ERG) a-wave, which reflects the hyperpolarization of photoreceptor outer segments (OS) [52,73], and the rod dominant phototropism was suggested to be a primary contributor to the IOS [54,74]. Therefore, we further hypothesized that the onset of TRP occurs earlier than cell hyperpolarization in the phototransduction cascade. To investigate the physiological origin of TRP, we have employed a modified Ringer's medium with sodium ions substituted by choline to maintain a condition of shut-off of rod circulating current and, thus, of suppressed stimulus-evoked hyperpolarization of the rods and signal transmission to downstream neurons (e.g., bipolar cells) [22,75,76]. Choline-substituted

medium achieves the shut-off of the circulating dark current because choline, unlike sodium, does not pass through cyclic guanosine monophosphate (cGMP) gated ion channels. Thus, if TRP has a receptor origin, it should persist during superfusion with low-sodium medium. Furthermore, the TRP, if resulting from receptor events upstream from the closure of cGMP-gated ion channels, might develop on a time scale faster than that of the ERG a-wave, which largely reflects the decrease in circulating current through cGMP-gated ion channels.

2.2 Materials and methods

2.2.1 Retinal preparation

Both leopard frogs (*Rana Pipiens*) and mice (*Mus musculus*) have been used to demonstrate stimulus-evoked ROS movement [55]. We selected frog retinas for this study because frog photoreceptors are relatively large and allow unambiguous observation of individual photoreceptors. Therefore, quantitative analysis of ROS movement can be readily implemented. The retinal preparation procedure has been reported in our previous publications [77]. Briefly, leopard frogs were euthanized by decapitation followed by double-pithing after dark adaptation for more than eight hours. The eyes were then enucleated and hemisected along the equator with fine scissors. A circular section of the retina with a diameter of about 6 mm was separated from the retinal pigment epithelium (RPE) and isolated from the back of the eye. Next, the isolated retina was positioned in a chamber (Fig.1A) with the OS of the photoreceptor facing upward and was continuously superfused with oxygenated Ringer's medium at room temperature (18~20 °C). The Ringer's medium contained 110.0 mM NaCl, 2.5 mM KCl, 1.6 mM MgCl₂, 1.0 mM CaCl₂, 22.0 mM NaHCO₃, and 10.0 mM D-glucose, pH 7.3~7.4. The low-sodium medium was

prepared by replacing the NaCl in the Ringer's medium with 110.0 mM choline chloride [70]. All procedures for preparation and study of the retina were performed in a dark room with dim red-light illumination. All experiments were performed following the protocols approved by the Animal Care Committee (ACC) at the University of Illinois at Chicago, and conformed to the statement on the use of animals in ophthalmic and vision research, established by the Association for Research in Vision and Ophthalmology (ARVO).

2.2.2 System setup

As shown in Fig. 2.1(A), the imaging system was based on a modified NIR light microscope (BX531WI, Olympus, Japan) with a 40X water immersion objective lens (UMPLFLN40XW, NA 0.8, Olympus, Japan). A CCD camera (pixel size: $7.4\ \mu\text{m} \times 7.4\ \mu\text{m}$; Pike, Allied Vision, Exton, PA) was employed for image acquisition. The acquisition rate was set to 100 frames per second (fps) with a frame resolution of 400×400 pixels. To specify the onset time of ROS movements, the CCD camera was replaced by a CMOS camera (pixel size: $6.5\ \mu\text{m} \times 6.5\ \mu\text{m}$; Neo 5.5, Andor Technology Ltd, Belfast, Ireland), providing an acquisition rate of 500 fps with a frame resolution of 431×122 pixels. A fiber-coupled light-emitting diode (LED) with a central wavelength at 550 nm (bandwidth: ~ 200 nm) was connected to the microscope to provide oblique light stimulation (angle: $\sim 20^\circ$, Fig. 2.1(B)). The stimulus pattern projected onto the retina was a rectangular area (Figs. 2.1(B) and 2.2(A)) of dimensions $19.8\ \mu\text{m} \times 252\ \mu\text{m}$ that covered about two rod photoreceptors in the lateral direction. The stimulus intensity was empirically set to $\sim 1.13 \times 10^8$ photon/ $\mu\text{m}^2/\text{s}$ to enable robust ROS movement. Full-field ERG recording [78] was implemented by placing differential electrodes on the top and bottom of the retina (Fig. 2.1(A), dashed square). The recorded ERG signal (sampling rate: 10 kHz) was processed

by a physiological amplifier (DAM 50, World Precision Instruments, Sarasota, FL) with a gain of 1,000 and a bandpass of 0.1 Hz to 10 kHz. The amplified ERG response was digitized using a 16-bit DAQ card (NI PCIe-6351, National Instruments, TX) and was sent to the computer for display and storage. The image acquisition, stimulation, and ERG recording were hardware-synchronized and software-controlled by a custom-designed Labview (National Instrument, TX) program.

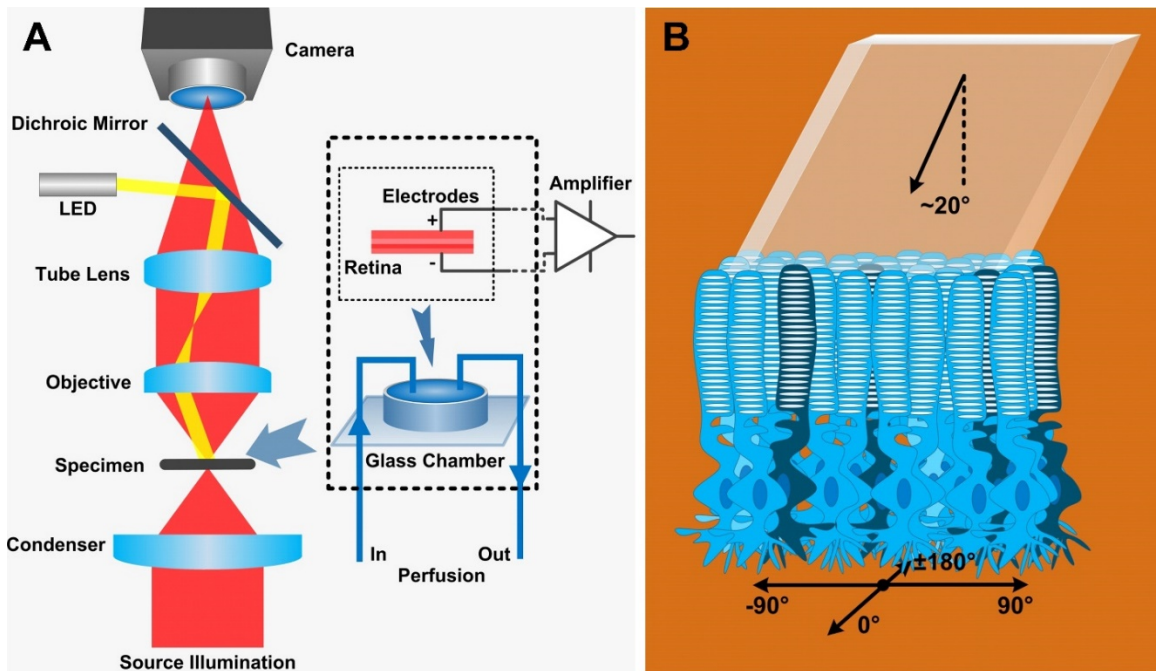


Fig. 2.1. (A) Schematic diagram of the experiment setup. Left: A custom modified microscope with a 40X water immersion microscope and a CCD (100 fps) or a CMOS (500 fps) camera was employed for imaging. Right: The ERG recording was achieved by placing electrodes on the retina in a glass chamber (dashed square). The isolated retina was continuously superfused with physiological medium during the experiment. (B) The retina was placed with photoreceptor layer on the top and was obliquely ($\sim 20^\circ$) stimulated by visible light from the top [56]. The coordinate axes shown at the bottom were used to define the direction of ROS movement. The 90° direction represents ROS movement toward the incident stimulation.

2.2.3 Experimental procedure

To investigate retinal physiological responses, the retina was consecutively superfused with Ringer's solution, low-sodium solution and then Ringer's solution again. Each

superfusion period lasted 20 minutes, allowing a complete replacement of the previous superfusion medium and sufficient retinal recovery, and was followed by a five-second imaging period. During the imaging period, the superfusion was suspended to provide a static imaging environment. Each imaging period was composed of three phases, including a 1.0-s pre-stimulus phase, a 1.0-s stimulus phase, and a 3.0-s post-stimulus phase.

2.2.4 Data analysis

The methods employed for the quantification of ROS movements and the segmentation of active areas were as described previously [56]. An optical flow algorithm [53] was employed to generate a movement magnitude map (Figs. 2.2(B) and 2.2(D)) and a movement direction map (Fig. 2.2(E)) for each acquired retinal image. Based on the magnitude map, a threshold was automatically calculated using Otsu's method [79]. Those pixels that had a higher movement magnitude than the threshold constituted active areas and the rest were inactive areas. The inactive areas on the direction map were then set to blue to highlight the active areas.

The temporal dynamics of the ROS movement magnitude was investigated by calculating the time course of the mean movement magnitude of the ROSs in each frame. The calculation of the mean movement magnitude was similar to that previously used for the computation of IOSs [52,73]. The primary procedures were the following: a $3\text{-}\delta$ threshold and a temporal window were applied to exclude potential spatial and temporal noise contributions. For the $3\text{-}\delta$ threshold, a pixel (p) with coordinator index (x_p, y_p) on a magnitude map with frame index k was assumed to reflect the signal if its intensity $I_k(x_p, y_p)$ satisfied

$$I_k(x_p, y_p) > \bar{I}_{pre}(x_p, y_p) + 3\delta_{pre}(x_p, y_p) \quad (11)$$

where $\bar{I}_{pre}(x_p, y_p)$ represents the mean intensity of the pixels with same index (x_p, y_p) in all pre-stimulus magnitude maps and $\delta_{pre}(x_p, y_p)$ represents the standard deviation. The temporal window was further employed to eliminate random movements that may have had higher magnitudes than the 3δ threshold but were not stimulus-related in magnitude map k . That is, we used this temporal window to examine whether $I_k(x_p, y_p), \dots, I_{k+n}(x_p, y_p)$ were consistently above the 3δ threshold and n was the frame number within the temporal window. Finally, a mean ROS movement magnitude, representing an overall movement level in frame k , was calculated by averaging all $I_k(x, y)$ s that, by the above criterion, were taken to be ROS movement signals, and a magnitude-time curve (Fig. 2.2(F)) was obtained by aligning the mean ROS movement magnitudes together according to the time sequence.

2.3 Results

Figure 2.2 shows imaging data (Figs. 2.2(A) - 2.2(E)), and time courses of stimulus-evoked ROS movement (Fig. 2.2(F)) and the ERG response (Fig. 2.2(G)) obtained in a representative experiment. This experiment involved superfusion only with normal Ringer's solution, and an image acquisition rate of 100 fps. The Fig. 2.2(A) images show the mosaic pattern of ROS. The Fig. 2.2(A) images were obtained before, during and after a 1-s stimulus, and Fig. 2.2(C) shows replicates, at higher magnification, the image obtained at time 0.4 s. The Fig. 2.2(B) data show, in color-coded fashion, the image by image determination of ROS movement for the Fig. 2.2(A) images. The Fig. 2.2(B) ROS movement image obtained at time 0.4 s, and the color key that applies to the Fig. 2.2(B) data are shown in Fig. 2.2(D). The color-coded Fig. 2.2(E) image shows the direction of

ROS movement corresponding to the Fig. 2.2(D) image. As shown respectively in Figs. 2.2(F) and 2.2(G), the stimulus evoked a rapidly rising mean movement of the ROS and an ERG response that contained a negative-going a-wave followed by a positive-going b-wave.

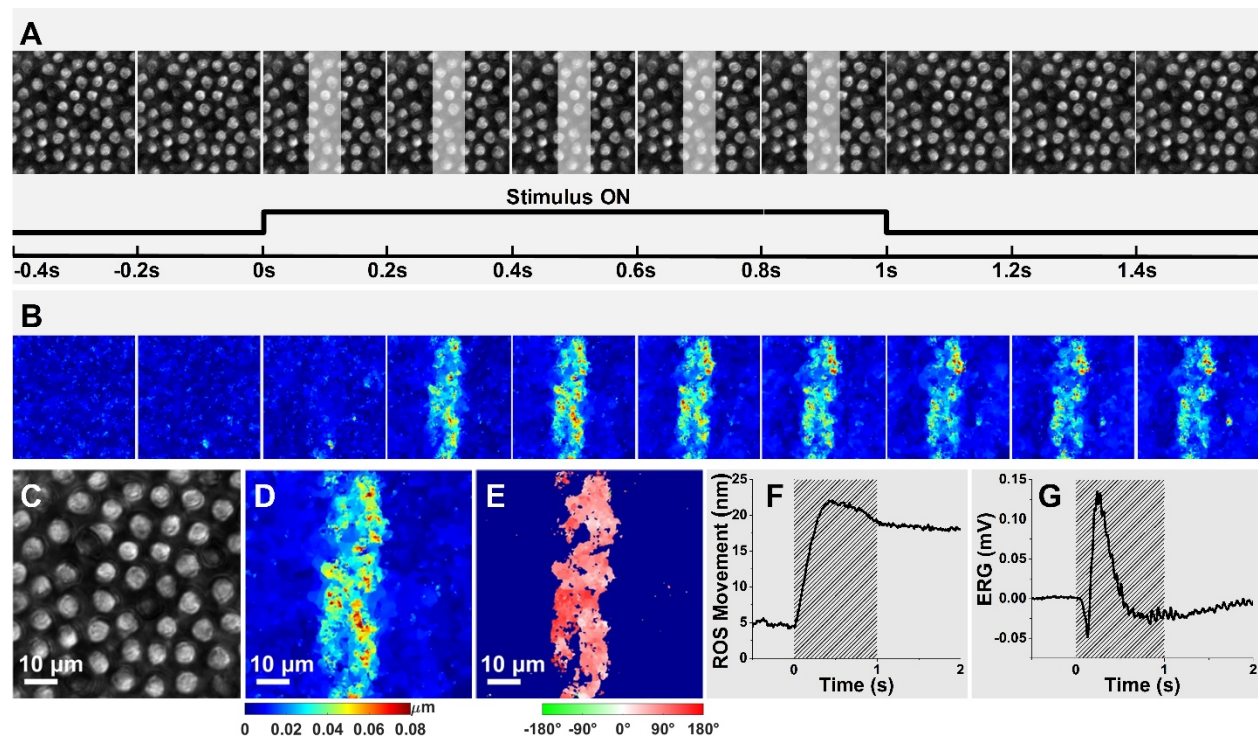


Fig. 2.2. (A) Top: Representative microscopy images of ROSs acquired in intervals of 0.2 s. The white regions in the panels represent the stimulus pattern presentations. Bottom: The imaging period (5 s) had three phases: pre-stimulus (1 s), stimulus (1 s), and post-stimulus (3 s) phases. (B) Dynamic magnitude changes of ROS movements corresponding to the retinal images in A. Enlarged microscopy image of ROSs acquired at time 0.4 s (C) and the corresponding movement magnitude (D) and direction (E) maps. (F) Time course of the mean magnitude of ROS movements. (G) Full-field ERG recorded from the isolated retina. The shaded areas in F and G indicate the stimulus duration.

A key objective of this study was to investigate the relative times of onset of the stimulus-evoked ROS movement and development of the ERG a-wave. Figure 2.3, which shows results obtained from a single representative retina, addresses this topic of relative timing of the ROS movement and the ERG a-wave response. To compare the time courses of these responses with an imaging temporal resolution exceeding that of Fig.

2.2 experiment, the imaging field in the Fig. 2.3 experiment was confined to a smaller area (Fig. 2.3(A)) of ROSs, allowing a higher image acquisition rate (500 fps), i.e., a 2-ms temporal resolution. Signal denoising was performed by averaging the magnitude-time curves of ROS movements and ERGs acquired from ten different locations of the retina. Figs. 2.3(B1) and 2.3(C1) display the averaged magnitude of ROS movements and ERGs over time. Figs. 2.3(B2) and 2.3(C2) provide enlarged illustration for the dashed squares in Figs. 2.3(B1) and 2.3(C1), respectively. For the ROS movements, the corresponding time of the first frame that had a mean movement magnitude larger than the $3\text{-}\delta$ threshold (mean plus three standard deviations) was assumed to be the onset time. The criterion also applied for estimating the onset time of the ERG a-wave. The onset times (red triangles in Figs. 2.3(B2) and 2.3(C2)) of ROS movements and ERGs were 10 ms and 38 ms, respectively, indicating a 28-ms delay for ERG a-wave onset.

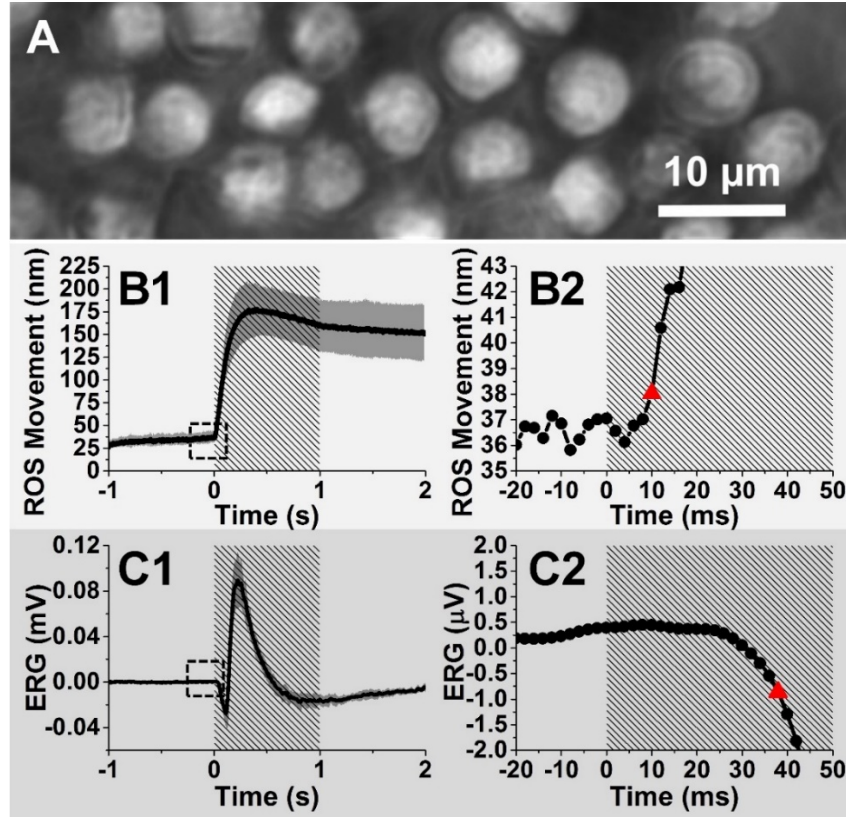


Fig. 2.3. (A) Representative ROS image acquired at a frame speed of 500 fps. Time course of the averaged mean movement magnitudes of ROSs (B1), and averaged ERGs (C1) acquired from ten different retinal locations. (B2) Enlarged picture of the dashed square in B1. (C2) Enlarged picture of the dashed square in C1. The red triangles in B2 and C2 indicate the onset times determined by the $3\text{-}\sigma$ threshold of ROS movement and ERG a-wave, respectively. Each data point shown in C2 (sampling rate of the original data: 10 kHz) represents the value exhibited at the end of a given 2-ms interval. Gray areas in B1 and C1 show standard deviations. Shaded areas in B1, B2, C1, and C2 represent stimulation periods.

In order to further investigate the relationship between the stimulus-evoked ROS movement and the electrophysiological response, we conducted comparative experiments with the retinas superfused with control Ringer's medium and low-sodium medium. During the experiment, the imaging area was fixed on the same location of the retina (Figs. 2.4(A1), 2.4(B1) and 2.4(C1)), avoiding possible differences in retinal responses caused by different retinal locations. Retinal images acquired at time 0.4 s (when ROSs usually have the maximum displacement) and their corresponding

photoreceptor movement magnitude maps and direction maps are shown in Figs. 2.4(A1) - 2.4(A3), 2.4(B1) - 2.4(B3) and 2.4(C1) - 2.4(C3), respectively.

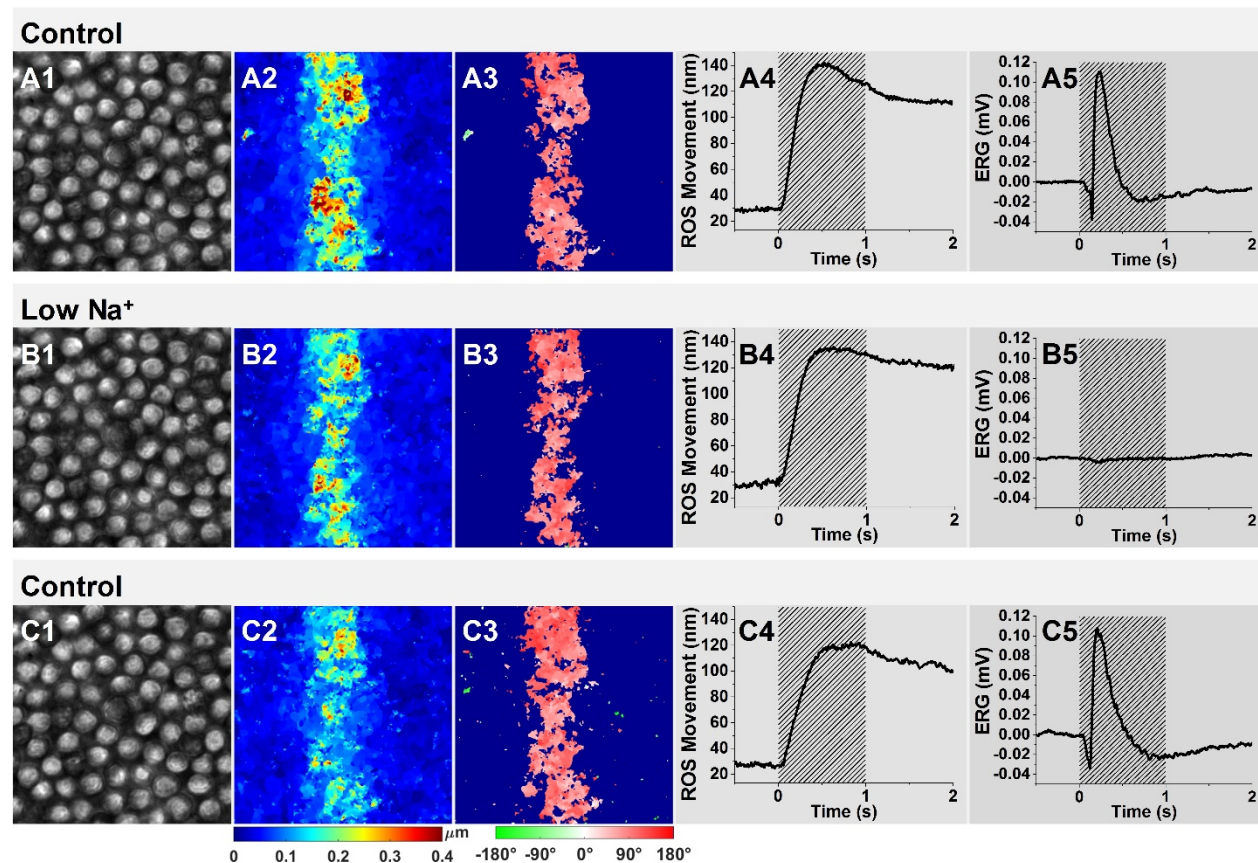


Fig. 2.4. Comparison of ROS movements and ERGs between control groups (superfusion with Ringer's medium) and the low-sodium group (superfusion with low-sodium medium). The retina superfusion followed a sequence of Ringer's medium superfusion (control group), low-sodium medium superfusion (low Na⁺ group), and Ringer's medium superfusion (control group). Representative ROS images acquired from the same area of the retina before (A1), during (B1) and after (C1) superfusion with the low-sodium medium. Representative movement magnitude maps and movement direction maps, before (A2, A3, respectively), during (B2, B3, respectively) and after (C2, C3, respectively) superfusion with the low-sodium medium. Time course of the mean movement magnitude of ROSs and ERGs acquired before (A4, A5, respectively), during (B4, B5, respectively) and after (C4, C5, respectively) the low-sodium superfusion. The magnitude maps (A2, B2 and C2) and direction maps (A3, B3 and C3) were calculated from the retinal images acquired at 0.4 s after the onset of the stimulus in the different groups.

As shown in Figs. 2.4(A2), 2.4(B2) and 2.4(C2), robust ROS movements were observed in the retina superfused with both normal medium and low-sodium medium. At

the same time, the movement direction was centered near 90° (Figs. 2.4(A3), 2.4(B3) and 2.4(C3)), showing that the stimulated rod photoreceptors swung toward the direction of the stimulus. The coordinates of the movement angle are shown in Fig. 2.1(B).

Figs 2.4(A4), 2.4(B4) and 2.4(C4) show time courses of the magnitude values of ROS movements. The waveforms of all three panels exhibited a stable and flat stage prior to flash presentation, a rapid rise upon the initiation of the flash stimulus, and a peak value at about 0.5 s.

As illustrated in Figs. 2.4(A4), 2.4(B4) and 2.4(C4), substitution of low-sodium medium did not substantially affect either the time course or the peak amplitude of the ROS movement period. However, the ERG responses were totally abolished by low-sodium medium (Fig. 2.4(B5)) and recovered essentially fully upon return of normal medium (Fig. 2.4(C5)).

Figure 2.5 illustrates ROS movement and ERG data obtained from a group of six retinas, including the retina described in Fig. 2.4. In each panel of Fig. 2.5, the mean ROS movement or ERG trace (black waveform) is accompanied by the standard deviations of data about the mean (gray areas). For the ROS movement data as well as the ERG data, the relationship of the standard deviation amplitudes to the mean waveform indicates general similarity of the results obtained from different retinas.

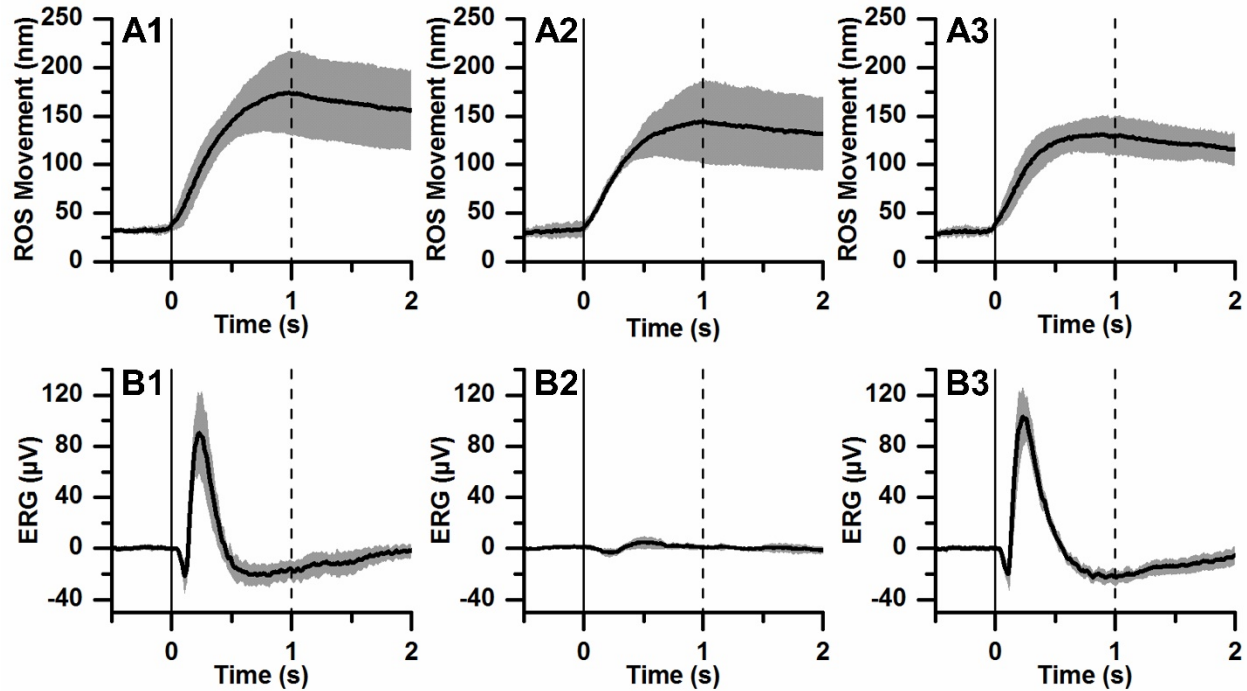


Fig. 2.5. Averaged ROS movements (A) and ERGs (B) of control (A1, B1), low-sodium (A2, B2), and recovery (A3, B3) groups. Each trace is the average of data obtained from 6 frog retinas. The gray area that accompanies each trace illustrates standard deviation. Vertical solid and dashed lines show stimulus onset and offset, respectively.

2.4 Discussion

In this study, we have investigated the relationship between the stimulus-evoked ROS movement and the ERG a-wave. In the presence of normal Ringer's solution, we found that the onset of ROS movement occurs earlier (~28 ms) than the onset of the ERG a-wave response (Fig. 2.3). We hypothesized that ROS movement is driven by signals/processes in the photoreceptors that are upstream from light-induced closure of the photoreceptor cGMP-gated ion channels. To test this hypothesis, we measured the effect of treatment with low-sodium medium, a condition that suppresses ERG a-wave generation. As shown in Figs. 2.4 and 2.5, our findings that the low-sodium treatment largely preserves both the peak amplitude and time course of ROS movement provide strong evidence that the events underlying ROS movement do not depend on cGMP-

gated ion channel closure. Rather, these events are tied directly or indirectly to the upstream, disc-based phototransduction steps that involve the sequential activation of rhodopsin, transducin and cGMP phosphodiesterase (PDE). As shown in Figs. 2.4 and 2.5, we observed that superfusion with low-sodium medium has little or no effect on the onset time of the ROS movement response. This observation argues against an effect of channel closure (i.e. ERG a-wave development) in either accelerating or delaying initiation of the ROS movement. An earlier study, employing OCT to characterize IOSs in the intact eye of frog, showed that onset of the stimulus-evoked IOS response can occur as early as 4 ms after flash initiation (Fig. 2.4(C) in [73]). This interval is shorter than the 10-ms onset time determined for ROS movement in the present work. Because the previous and present studies differ in several respects, including the investigation of intact eye vs. isolated retina, OCT vs. microscopy system, and possible differences in photostimulation efficiency, the extent to which the presently measured ROS movement accounts for the previously measured overall IOS remains to be determined. For isolated retina, this issue can be addressed in future work by using either a camera with higher frame acquisition rate, or other high-speed imaging techniques such as high-speed confocal [47,52,80,81] or OCT [56,73] systems.

It is interesting to consider our data in the context of the possibility that the blockage of rod circulating current can provide osmotic and therefore structural changes within the photoreceptor [82,83]. The preservation of stimulus-evoked ROS movement in low-sodium medium argues against the possibility that an osmotic change tied to a light-induced change in closure of cGMP-gated ion channels underlies the ROS response. However, remaining open possibilities include stimulus-evoked rhodopsin-, transducin-,

and/or PDE-dependent permeability changes [84-86], compression of disc membranes [87], and the distribution of the phospholipids in the disc membranes [88]. As TRP clearly depends on a structural perturbation of the OS, these possibilities offer possible avenues for investigating the basis of TRP at a subcellular level.

This study has involved the recording of stimulus-evoked retinal responses from isolated retina. We selected isolated retina as the experimental preparation for two reasons. First, isolated retina (in comparison with eyecup preparation or intact eyes) allows a more precise and efficient control of the bathing environment. Second, the free distal ends of ROSs, realized by separation of the retina from the RPE, enable a direct view of, and facile quantification of, the ROS movements. However, it is important to clarify that the movement magnitude of the photoreceptors in the isolated retina may differ from that in the natural condition in which the ROSs interface with the RPE. For pursuing *in vivo* investigation, we are constructing a super-resolution ophthalmoscope, based on virtually structured detection (VSD) [89-91].

2.5 Conclusion

This study reports a comparative investigation of TRP associated ROS movement and electrophysiological dynamics in the retina stimulated by oblique visible light. Our experimental results and theoretical analysis suggest that early, disc-based stages of the phototransduction cascade, which occur before hyperpolarization, contribute to the TRP-associated movement of rod photoreceptors. As TRP reflects a functional response of the retina to a light stimulus, further study of the TRP mechanism will not only benefit in-depth understanding of photoreceptor physiology, but also may provide a valuable biomarker for advanced diagnosis of retinal diseases.

Acknowledgment

The authors thank Professor Klaus Peter Hofmann for his helpful comments on this manuscript, and Mr. Marek T. Mori for mechanical design and manufacturing. This research was supported in part by NIH grants R01 EY023522, R01 EY024628, P30 EY001792, and R21 EY023430; by NSF grant CBET-1055889; by Research to Prevent Blindness (New York, NY); and by the Daniel F. and Ada L. Rice Foundation (Skokie, IL).

CHAPTER III. COMPARATIVE STUDY OF WILD-TYPE AND RD10 MICE REVEALS TRANSIENT INTRINSIC OPTICAL SIGNAL RESPONSE BEFORE PHOSPHODIESTERASE ACTIVATION IN RETINAL PHOTORECEPTORS

(Manuscript under review. Submitted as Yiming Lu, Taehoon Kim, and Xincheng Yao, Comparative study of wild-type and rd10 mice reveals transient intrinsic optical signal response before phosphodiesterase activation in retinal photoreceptors, Experimental Biology and Medicine (2019))

Abstract: Transient intrinsic optical signal (IOS) has been observed in stimulus-evoked retinal photoreceptors. This study is to compare IOS changes in wild-type (WT) and retinal degeneration 10 (rd10) mouse retinas, to evaluate the effect of cyclic guanosine monophosphate phosphodiesterase (PDE) on photoreceptor-IOS. Time-lapse near-infrared light microscopy was employed to monitor the spatiotemporal dynamics of the IOS responses in freshly isolated retinas activated by visible light stimulation. Comparative IOS recordings were conducted at postnatal days 14 (P14) and P16. At P14, IOS magnitudes and spatiotemporal dynamics in WT and rd10 retinas were similar, indicating that the PDE deficiency in rd10 did not affect the formation of photoreceptor-IOS. At P16, IOS magnitude in rd10 significantly decreased compared to that in WT, suggesting the IOS sensitivity to the photoreceptor degeneration in rd10. Our experimental results and theoretical analysis indicate that early disc-based stages of the phototransduction cascade before the activation of PDE may contribute to the formation of the photoreceptor-IOS responses; and the IOS can be a sensitive biomarker for objective assessment of retinal function.

3.1 Introduction

Functional assessment of retinal physiology is important for early detection and treatment assessment of eye diseases, such as age-related macular degeneration (AMD), diabetic retinopathy (DR), and retinitis pigmentosa (RP) [9,92,93]. Electroretinogram (ERG) can be used for objective evaluation of the retinal function. However, it provides limited spatial resolution and signal specificity [78]. Intrinsic optical signal (IOS) imaging of retina measures the stimulus-evoked intrinsic optical property changes, such as light scattering, polarization, and absorption fluctuation, in the retina activated by visible light stimulation[74]. In conjunction with advanced imaging technologies, such as optical coherence tomography (OCT), scanning laser ophthalmoscopy (SLO) and adaptive optics, functional IOS imaging promises a noninvasive, objective and high-resolution method to evaluate retinal physiological function [12,50,51].

Retinal IOS responses have been demonstrated in different animal models and human eyes with various optical imaging modalities [44,49,94,95]. Rapid IOS has been consistently observed in retinal photoreceptors, and slow IOS changes have been reported correlated with inner retinal neural response and hemodynamics [12]. The photoreceptor-IOS occurs almost right away, < 4 ms after the initiation of retinal stimulation [46,73]. Transient photoreceptor outer segment (OS) changes have been demonstrated to have a close correlation with the rapid photoreceptor-IOS [54,95]. Comparative ERG study of freshly isolated retina further revealed that such conformational changes happen before the hyperpolarization of the photoreceptors [1]. These experimental observations suggested that the rapid photoreceptor-IOS has a physiological origin in the upstream, disc-based phototransduction cascade steps,

including the sequential activation of rhodopsin, transducin and cyclic guanosine monophosphate (cGMP) phosphodiesterase (PDE) [21,22,24].

In this study, a retinal degeneration mouse model $Pde6b^{rd10}$ (rd10) was used to test if the PDE is involved in the production of transient photoreceptor-IOS. The rd10 mouse model has a spontaneous mutation in the gene of the β -subunit of PDE (β -PDE) in the rod photoreceptors [96]. The deficiency of PDE causes the accumulation of cGMP and results in the degeneration of rod photoreceptors due to the excessive influx of cations. However, as the rods still express <40% of endogenous PDE in the rd10 mouse, it has a relatively delayed onset of photoreceptor degeneration [96]. Before postnatal days 15 (P15), the relative expression level of rhodopsin and transducin in rd10 mouse are similar with that in the wild-type (WT) mouse. Additionally, the difference between relative cell death ratios in WT and rd10 mouse are also insignificant in the first two postnatal weeks [96,97]. In comparison, the relative expression level of PDE in rd10 mouse is about 21% – 28% of that in the WT mouse during P12 - P14 [96]. Therefore, a comparative study between WT and rd10 mice before P15 can specifically reveal the effect of PDE deficiency on the photoreceptor-IOS. WT and rd10 mice at P14 were selected for comparative IOS imaging study to test the effect of PDE on the photoreceptor-IOS. Furthermore, the retinal degeneration process in rd10 mouse starts from P16 – P18 [96-98]. Thereafter, the relative expression level of rhodopsin and transducin significantly decreases in the rd10 mouse compared to that in the WT mouse. Histological changes of the retina have been consistently observed in rd10 mouse since P16 [99,100]. To demonstrate the impact of early retinal degeneration process on the photoreceptor-IOS, comparative IOS imaging study of WT and rd10 retinas at P16 was conducted.

3.2 Materials and methods

3.2.1 Experimental setup

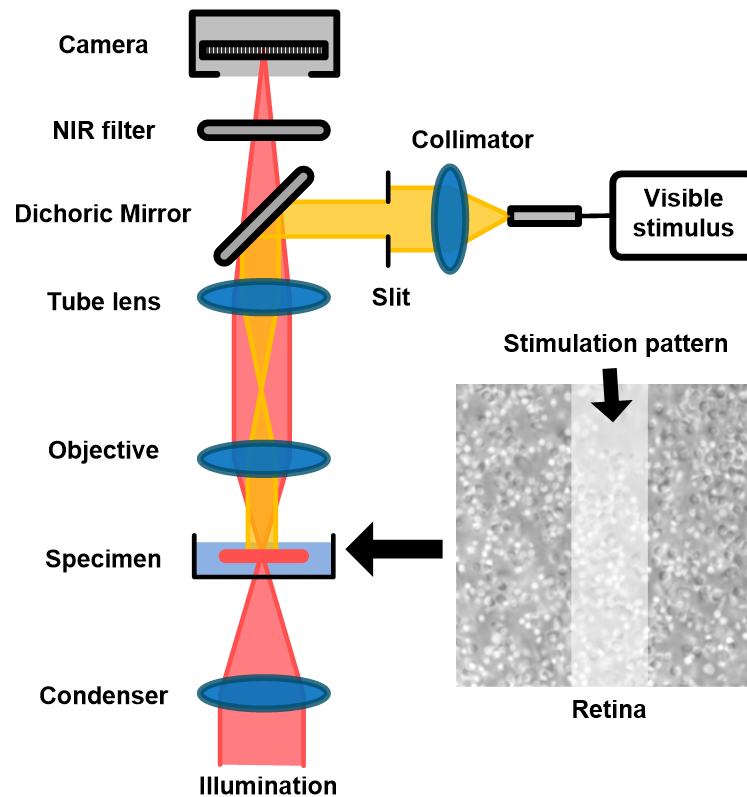


Fig. 3.1. Schematic diagram of experiment setup. A custom modified microscope, with a 60x objective and a CMOS camera (16 bits depth and 100 frames/s), was used for retinal imaging. During the experiment, the photoreceptor outer segment (OS) tips were facing upward and the retina was oxygenated with physiological solution (pH 7.4 and 35~37°C). A rectangular stimulus pattern, generated by a slit and a LED at visible wavelength, was projected to the retina for localized stimulus. The stimulus duration was 500 ms for all the experiments.

Figure 3.1 illustrates the schematic diagram of the experimental setup. The imaging system is based on a modified NIR light microscope (BX531WI, Olympus) with a 60X objective lens (LUMPLanFL60X, NA 0.9, Olympus). A fiber-coupled light-emitting diode (LED) at visible wavelength (center wavelength: 550 nm, bandwidth: ~200 nm) was used to provide retinal stimulation. The stimulus light was collimated and then coupled into the microscope. A slit with its conjugate plane at the sample plane was employed to generate

a rectangular stimulus pattern ($\sim 12 \mu\text{m} \times 56 \mu\text{m}$) at the center of the field of view. The stimulus intensity was set to $\sim 3.6 \times 10^9$ photon/ $\mu\text{m}^2/\text{s}$ with a duration of 500 ms during the experiment. A perfusion system was employed to perfuse the retina with oxygenated bicarbonate-buffered Ames medium (pH 7.4 and $35 \sim 37^\circ\text{C}$) during the experiment. The perfusion was suspended during the image recording to minimize the effect of fluid fluctuation on the image quality. The retinal images were recorded by a CMOS camera (pixel size: $6.5 \mu\text{m} \times 6.5 \mu\text{m}$, Neo 5.5, Andor Technology) with an imaging speed of 100 frames/s and a frame resolution of 512×512 pixels. The stimulus light source and the image recording system were electronically synchronized and controlled by a custom-designed LabView (National Instrument) platform.

3.2.2 Sample preparation

WT mice (57BL/6J, The Jackson Laboratory) and rd10 mice (B6.CXB1-Pde6b^{rd10}/J, The Jackson Laboratory) at P14 and P16 were used in this study. Both WT and rd10 mice were maintained in standard housing conditions under a 14/10-hour light-dark cycle. For each postnatal day, 12 WT mice and 12 rd10 mice with no significant difference in body size and weight were selected for experiments. All the mice were dark-adapted for more than 6 hours before the experiment. The isolation of mouse retina has been reported in our previous study [101]. Briefly, enucleated eyeball from anesthetized mouse was hemisected along the equator with fine scissors. The retina was then carefully isolated from the retinal pigment epithelium (RPE) and separated from the back of the eye. The isolated retina was transferred to a chamber for IOS imaging with the OS tip of the photoreceptor facing upward. As the photoreceptors degenerate first in rd10 mouse model, such setup allows an unambiguous identification of the structural change of

photoreceptors and a reliable identification of the IOS responses from photoreceptors. All the procedures were performed in oxygenated bicarbonate-buffered Ames medium (pH 7.4 and 35 ~ 37 °C). To ensure the consistency of the observations, retinal images were all acquired from the retinal locations close to the optical nerve head [98] and the imaging plane was focused at the photoreceptor OS layer. All the procedures were conducted in a dark room with minimum level of red-light illumination. All experiments were performed following the protocols approved by the Animal Care Committee (ACC) at the University of Illinois at Chicago and conformed to the statement on the use of animals in ophthalmic and vision research, established by the Association for Research in Vision and Ophthalmology (ARVO).

3.2.3 Data processing

Figure 3.2 shows representative retinal images and corresponding IOS maps. Each recording trial contains three phases, a 1.0-s pre-stimulus phase, a 0.5-s stimulus phase, and a 3.5-s post-stimulus phase. The IOS can be processed based on the retinal images:

$$IOS_t(x, y) = \frac{|\Delta I_t(x, y)|}{\bar{I}_{pre}(x, y)} = \frac{|I_t(x, y) - \bar{I}_{pre}(x, y)|}{\bar{I}_{pre}(x, y)} \quad (12)$$

where $IOS_t(x, y)$ represents the IOS map with a frame index of t , $\bar{I}_{pre}(x, y)$ represents the mean intensity map of all images recorded during the pre-stimulus phase, and $I_t(x, y)$ is the retinal image with a frame index of t . A 3- δ threshold and a temporal window filter were applied to suppress potential spatial and temporal noise contributions to the IOS map. For the 3- δ threshold, a pixel with coordinate (x_k, y_k) in a retinal image $I_t(x, y)$ will be regarded as reflecting IOS when $I_t(x_k, y_k) > \bar{I}_{pre}(x_k, y_k) + 3 \cdot \delta_{pre}(x_k, y_k)$ or $I_t(x_k, y_k) < \bar{I}_{pre}(x_k, y_k) - 3 \cdot \delta_{pre}(x_k, y_k)$, where $\delta_{pre}(x_k, y_k)$ is the standard deviation of

all pre-stimulus images. For the temporal window filter with an n -frame window size, $I_t(x_k, y_k) \cdots I_{t+n}(x_k, y_k)$ should consistently meet the $3\text{-}\delta$ threshold to include $I_t(x_k, y_k)$ for IOS calculation. In this study, $n = 3$ was used considering the signal-to-noise ratio of IOS responses.

3.3 Results

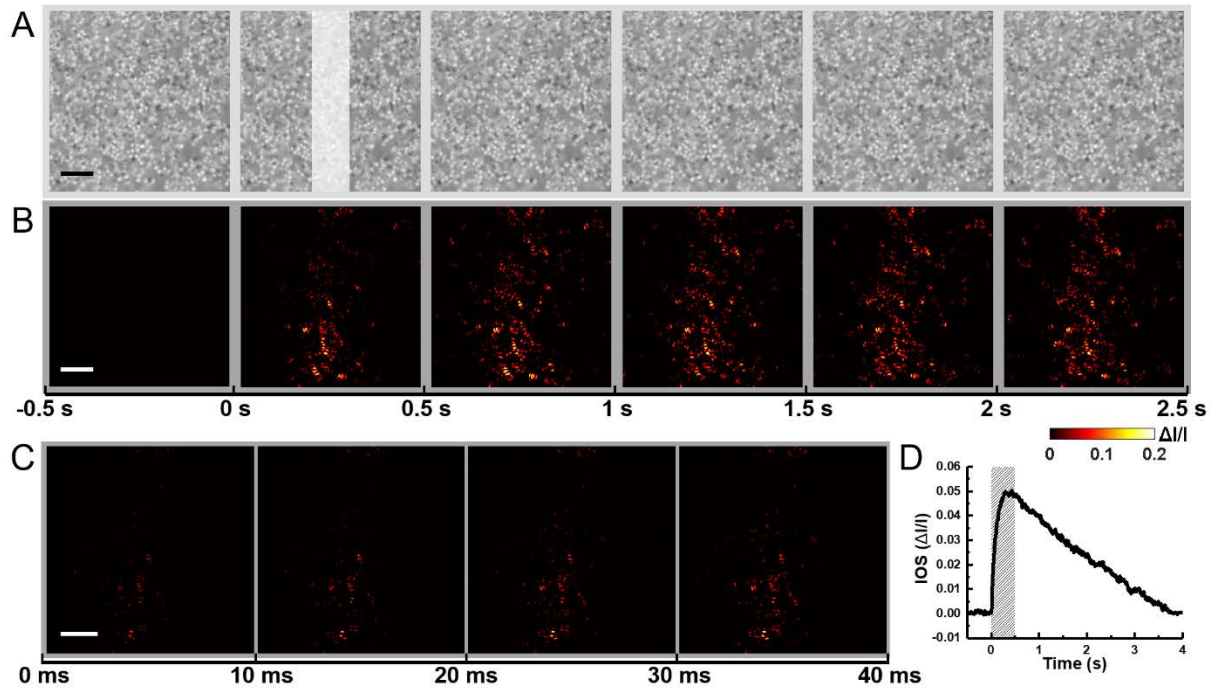


Fig. 3.2. (A) Representative microscopic images of a PN16 mouse retina acquired with a 0.5-s interval. The white rectangle in the second frame shows the visible stimulus pattern with a duration of 0.5s. (B) Temporal sequence of IOS maps corresponding to the data in (A). Each panel represents an average of all 50 IOS maps acquired during the 0.5-s interval indicated by the time axis at the bottom. (C) Enlarged single-frame IOS maps acquired after the onset of stimulus with an imaging speed of 100 frames/s. The time axis at the bottom indicates the acquisition time. (D) Time course of the mean magnitude of IOS responses. The shaded area indicates the stimulus duration. Scale bars represent 10 μm .

Figure 3.2(A) shows a representative sequence of retinal images acquired from a P16 mouse. Individual photoreceptor OS tips can be clearly identified. Figure 3.2(B) shows the corresponding IOS image sequence. Each illustrated frame is an average of 50 IOS

maps acquired during the 0.5-s interval. Figure 3.2(C) shows the sequence of immediate IOS responses after the onset of stimulus at a temporal resolution of 10 ms. As shown in the Figure 3.2(C), rapid photoreceptor-IOS occurred almost immediately, within 10 ms after the onset of stimulus. Moreover, the IOS intensities increased and its spatial distribution broadened over time. To quantify the temporal dynamics of IOS responses, a magnitude-time curve of IOS responses was obtained by averaging the IOS intensities in each IOS map and aligning them together following the time sequence (Figure 3.2(D)). The waveform of the curve shows that the flash stimulus evoked a robust photoreceptor-IOS with a peak at ~ 0.4 s. Additionally, the IOS intensities gradually recovered to baseline in the post-stimulus phase.

To test the effect of PDE deficiency on the IOS formation, we performed comparative studies of WT and rd10 mice at P14 (Figures 3.3(A) and 3.3(B)) and P16 (Figures 3.3(C) and 3.3(D)). At P14, the overall structure of photoreceptors remained similar between WT and rd10 mice (Figure 3.3(A1) and 3.3(B1)). The spatial distribution of IOS responses in both groups were mainly confined within the stimulus pattern, and the IOS magnitudes were also relatively similar (Figure 3.3(A2) and 3.3(B2)). Figure 3.3(A3) and 3.3(B3) show time courses of the IOS magnitude values. IOS waveforms in both WT and rd10 presented a flat stage prior to flash delivery, a rapid rise upon the initiation of the flash stimulus, a peak before the shutoff of the stimulus, and a recovery to baseline at ~ 2 s. The similarities between Figures 3.3(A2) and 3.3(B2), and Figures 3.3(A3) and 3.3(B3) indicate that the PDE deficiency in rd10 mouse retina did not affect the formation of IOS responses.

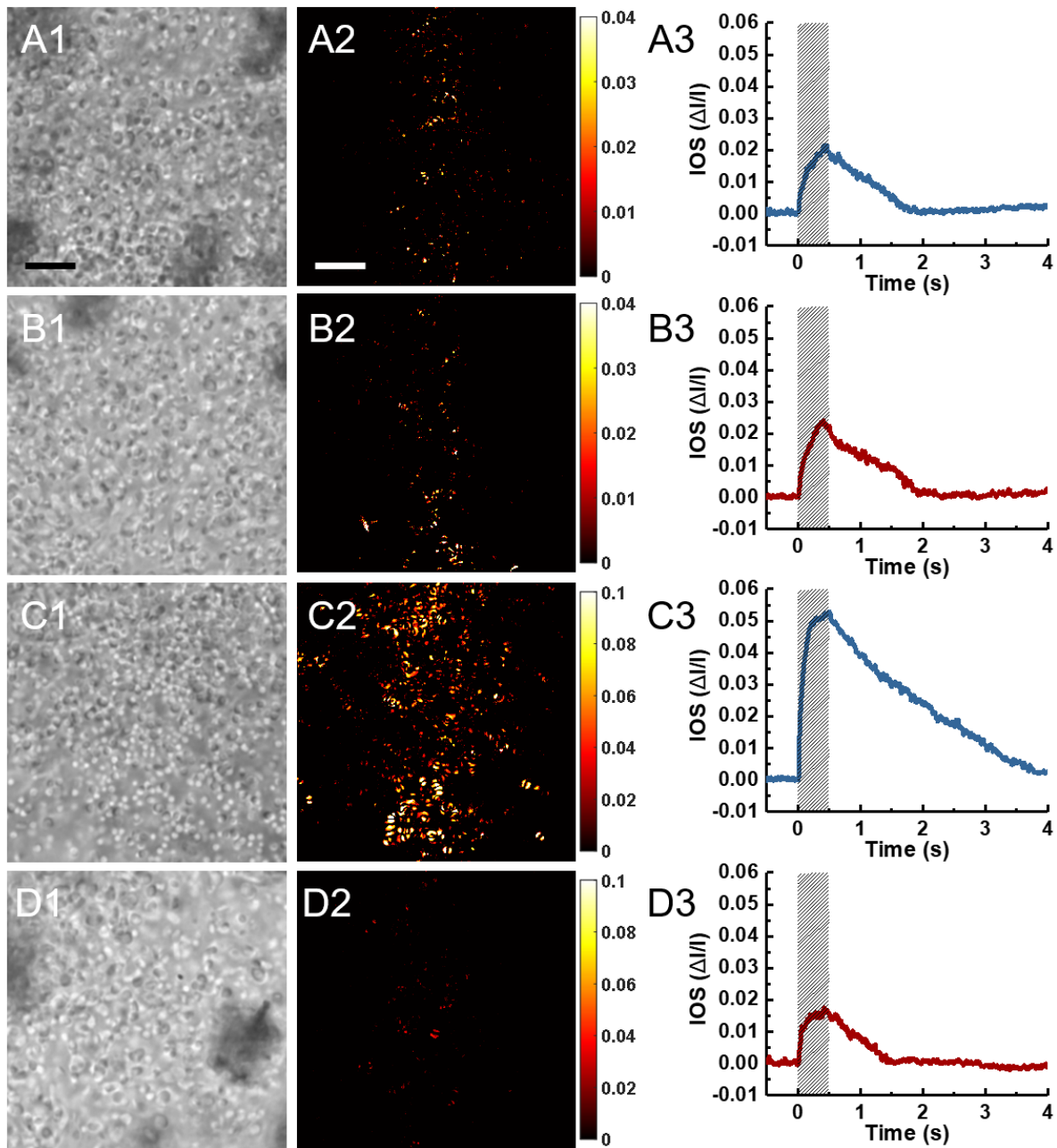


Fig. 3.3. Comparison of IOS responses between WT and rd10 groups at P14 and P16. (A) Representative retinal images (left) and IOS map obtained at 0.5 s (middle), and time course of mean IOS magnitude (right), acquired from a WT mouse retina at P14. (B) Representative results acquired from a rd10 mouse retina at P14. (C) Representative results acquired from a WT mouse retina at P16. (D) Representative results acquired from a rd10 mouse retina at P16. Scale bars represent 10 μm . Shaded areas indicate stimulus duration.

As shown in Figures 3.3(C1) and 3.3(D1), differences between the photoreceptor structures in WT and rd10 mouse retinas emerged at P16. Though some photoreceptor tips can still be identified in the rd10 mouse retina at P16, the spatial distribution and intensity of IOS responses exhibited significant attenuation in the rd10 mouse retina (Figure 3.3(D2)), compared to that in WT mouse retina (Figure 3.3(C2)). The magnitude-time curve of IOS responses in rd10 mouse retina (Figure 3.3(D3)) also shows a significantly lower peak value, compared to that in WT mouse retina (Figure 3.3(C3)).

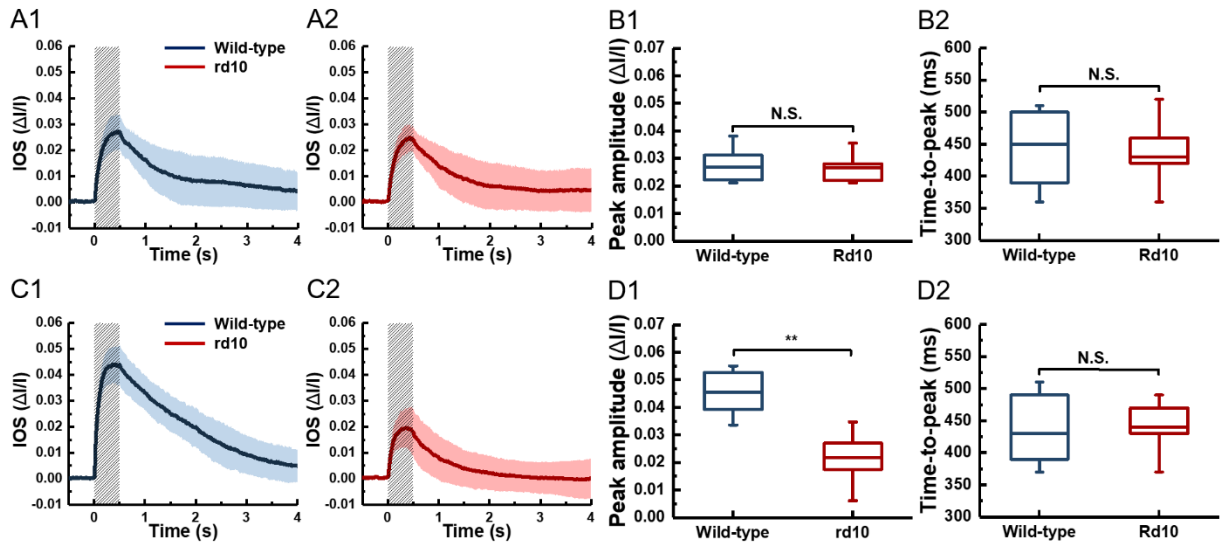


Fig. 3.4. Averaged IOS responses from WT and rd10 mice at P14 and P16 and the corresponding statistical characterization. Averaged magnitude-time curve of IOS responses from 12 WT mouse retinas (A1) and 12 rd10 mouse retinas (A2) at P14. (B1) and (B2) are statistics of peak amplitudes and time-to-peaks corresponding to the data shown in (A1) and (A2), respectively ($n = 12$, N.S. = not significant). Averaged magnitude-time curve of IOS responses from 12 WT mouse retinas (C1) and 12 rd10 mouse retinas (C2) at P16. (D1) and (D2) are statistics of peak amplitudes and time-to-peaks corresponding to the data shown in (C1) and (C2), respectively ($n = 12$, N.S. = not significant, $**p < 0.05$). Significance was determined by a two-sample t-test with equal variance assumed. The normality of data was determined using Kolmogorov-Smirnov test. Each solid curve in (A) and (C) represents the mean values, and the accompanied colored area represents the corresponding standard deviations, of the IOS responses. The gray shaded areas represent stimulus duration.

To further confirm the observation, we repeated the experiment on 12 WT and 12 rd10 mice retinas at both P14 and P16, including the retinas shown in Figure 3.3. The results are shown in Figure 3.4. In each panel of Figures 3.4(A) and 3.4(C), the solid curve is the mean of all IOS magnitude-time curves from 12 retinas and the accompanied colored area represents the standard deviations of data about the mean. For all the IOS data, the relationship of the standard deviation amplitudes to the mean waveform indicates a general similarity of the results obtained from different retinas. As the waveforms shown in Figures 3.4(A1) and 3.4(A2), the IOS responses in WT and rd10 mouse retinas were similar at P14. However, the WT mouse retinas showed significantly stronger IOS responses than rd10 mouse retinas at P16. To better demonstrate the similarity/difference of IOS responses between WT and rd10 group at each postnatal day, peak amplitude (the maximum value of the IOS magnitude) and time-to-peak (time taken to reach the peak amplitude) of the IOS waveforms were statistically analyzed. The results in Figures 3.4(B1) and 3.4(B2) show that there was no significant IOS difference between WT and rd10 mice at P14. For P16, the IOS peak amplitudes of WT mice retinas were significantly higher than that in the rd10 mice retinas (Figure 3.4(D1)), while the time-to-peaks still showed no significant difference (Figure 3.4(D2)). The results are consistent with the previous observations in Figure 3.3.

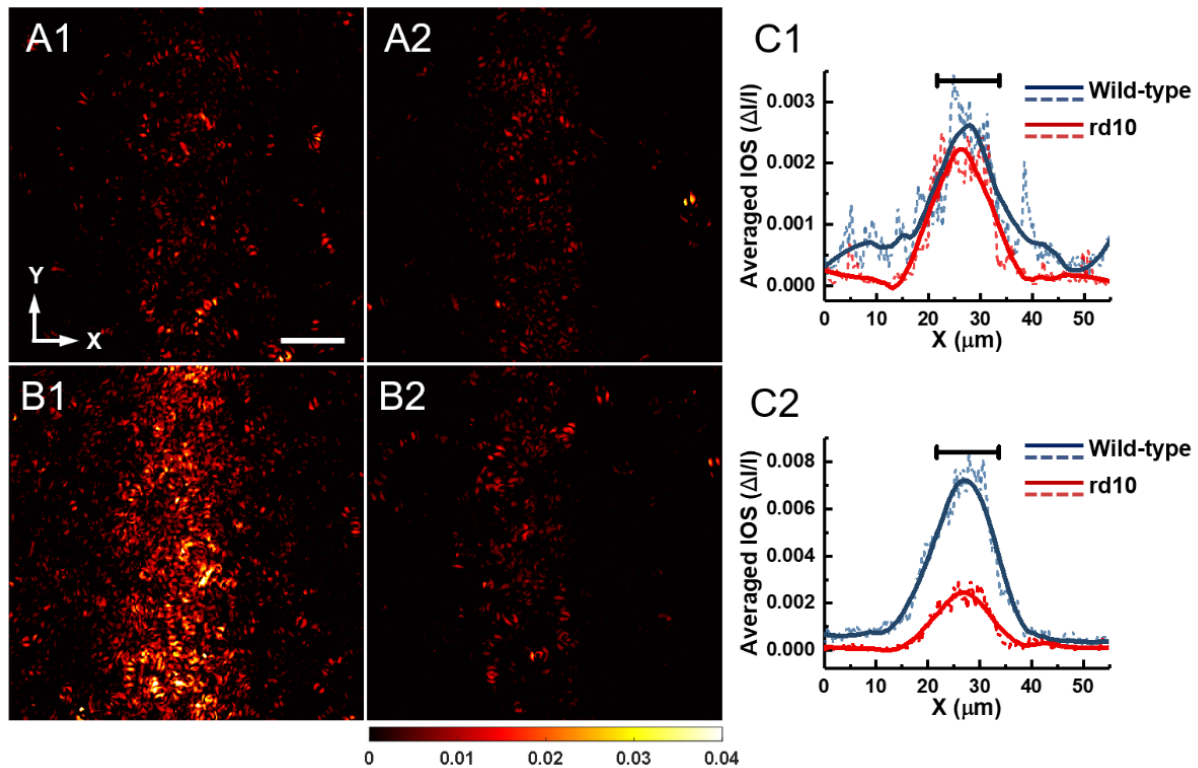


Fig. 3.5. Averaged IOS maps acquired at 0.5 s after the onset of stimulus from WT and rd10 mice. Each panel is an average of IOS maps from 12 retinal samples. Averaged IOS map of WT (A1) and rd10 (A2) mice at P14, and WT (B1) and rd10 mice (B2) at P16. (C) Intensity profiles of the IOS maps averaged along Y-direction. The dashed curves represent raw profile of the mean intensity. The solid curves represent the corresponding profiles smoothed by 40 points. Mean intensity profiles of WT and rd10 mice at P14 (C1) and P16 (C2). The black bars at the top represent the width of stimulus pattern (~12 μm).

Figure 3.5 shows the averaged IOS maps in WT and rd10 groups at time 0.5 s. Each panel in Figure 3.5 shows averaged data from 12 retina samples. At P14, the spatial distribution of IOS responses in WT group (Figure 3.5(A1)) was similar to that in rd10 group (Figure 3.5(A2)). The majority of the active pixels are within the stimulus pattern. At P16, the distribution of IOS responses in the WT group appeared wider in the X-direction and presented overall higher intensities compared to the rd10 group. To better quantify the difference in the spatial distribution of IOS responses, each panel was averaged in the Y-direction and converted as an intensity profile in the X-direction (dashed curves in Figures

3.5(A3) and 3.5(B3)). To better show the spatial distribution of IOS responses, the intensity profiles were smoothed by an empirical 40-point rolling window (solid curves in Figures 3.5(A3) and 3.5(B3)) with which the background perturbations can be sufficiently reduced but the overall shape of the profile can be reasonably maintained. At P14, the full-width-half-maximum (FWHM) value of the smoothed IOS intensity profiles in WT and rd10 group are $\sim 14.6 \mu\text{m}$ and $\sim 14.2 \mu\text{m}$, respectively. At P16, the FWHM values of the smoothed IOS intensity profiles for WT and rd10 group are $\sim 14.8 \mu\text{m}$ and $\sim 12.35 \mu\text{m}$, respectively. The results show that the spatial distributions of the IOS responses in WT and rd10 group were similar at P14. But at P16, the spatial distribution of the IOS responses in rd10 were compressed compared to that in WT group.

3.4 Discussion

In this study, we compared the IOS responses in WT and rd10 retinas at P14 to investigate the effect of PDE deficiency on the photoreceptor-IOS formation. As the rod degeneration starts at around P16 in rd10 mouse, comparative IOS imaging at P14 can isolate the impact of PDE deficiency from other degeneration factors (P15 was not considered to avoid the potential overlap with the degeneration process). A key observation was that the IOS responses in rd10 mice were similar with that in WT mice at P14. As shown in Figure 3.4(A), the overall waveform of the mean IOS curve and the amplitudes of the corresponding standard deviations about the mean in the WT group were generally similar with that in the rd10 group. Further statistical analysis about two descriptive parameters of the curves, peak amplitude and time-to-peak, confirmed that the IOS responses in WT and rd10 group were similar in terms of IOS magnitude and time course. The spatial spread of the IOS patterns, reflected by the averaged intensity

profiles (Figure 3.5(C1)), show that the IOS responses had a similar spatial distribution in WT and rd10 group. Such similarities in the temporal dynamics and the spatial distribution of the IOS responses between WT and rd10 groups indicate that the PDE deficiency in rd10 rods did not affect the formation of IOS responses.

Previous *in vivo* IOS imaging with a high-speed OCT (1250 frames/s) has demonstrated that the photoreceptor-IOS had an onset time of ~1.1 ms, suggesting a signal origin in the early, disc-based phototransduction steps which includes the activation of rhodopsin, transducin, and PDE [46]. As the relative concentration of rhodopsin: transducin: PDE is ~100:10:1, PDE is the rate-limiting factor for the disc-based phototransduction cascade [21,23]. The stimulus employed in this study has an intensity ($\sim 3.6 \times 10^9$ photon/ $\mu\text{m}^2/\text{s}$) that was sufficient to activate most of the PDEs at millisecond level in both WT and rd10 rods at P14 [21,102]. If the IOS responses are directly originated from or tightly correlated with the activity of PDE, we expect that a higher level of activated PDE in WT rods would contribute to a faster formation of IOS responses, reflected by a steeper rising phase and a shorter time-to-peak value of the IOS time courses, compared to that in the rd10 rods. However, our data show that there was no significant difference between the time-to-peak values of the IOS in WT and rd10 mice (Figure 3.4(B1)). Based on these results, we speculate that the IOS responses have a disc-based physiological origin that is upstream from the activation of PDE in the phototransduction cascade, including the activation of rhodopsin and transducin.

In a previous OCT study, the thickness of the total retina and the photoreceptor layer (from Bruch's membrane to the inner nuclear layer/outer plexiform layer interface) showed observable but slight difference between WT and rd10 retinas at P16 [100], while

the IOS responses in WT and rd10 mice presented significant difference at P16 in this study. It demonstrates that the IOS responses are tightly correlated with the integrity of photoreceptor functionality and can be more sensitive to the early degeneration process than the morphological distortion due to the PDE-associated retinal degeneration.

In conclusion, our experimental study and theoretical analysis indicate that early, disc-based stages of the phototransduction cascade, which are upstream from the activation of PDE, can primarily contribute to the formation of the photoreceptor-IOS responses. The IOS promises a sensitive biomarker for objective assessment of the functional integrity of retinal photoreceptors. Functional IOS imaging may advance the diagnosis and treatment management of eye diseases, such as AMD and RP, which are known to damage retinal photoreceptors.

Funding

This research was supported in part by NIH grants R01 EY030101, R01 EY023522, P30 EY001792; by unrestricted grant from Research to Prevent Blindness; by Richard and Loan Hill endowment.

CHAPTER IV. LIGHT-INDUCED LENGTH SHRINKAGE OF ROD PHOTORECEPTOR OUTER SEGMENTS

(Previously published as Yiming Lu, Jacopo Benedetti, Xincheng Yao. Light-induced length shrinkage of rod photoreceptor outer segments. *Translational Vision Science & Technology*;7(6):29 (2018) [2])

Abstract: This study was designed to verify light-induced outer segment (OS) length shrinkage of rod photoreceptors and to characterize its anatomic source at disc-level resolution. Frog (*Rana pipiens*) retinas were used for this study. Time-lapse light microscopy of freshly isolated OSs was employed to test transient rod OS changes at 10 ms temporal resolution. Histological light microscopy of dark- and light-adapted retinas was used to confirm light-induced rod OS length changes; and transmission electron microscopy (TEM) was used to quantify light-driven structural perturbation of rod OSs at disc level resolution. Time-lapse light microscopy images verified transient length shrinking responses in freshly isolated rod OSs. Histological light microscopy images confirmed reduced rod OS lengths in light-adapted retinas, compared to that of dark-adapted retinas. TEM images disclosed shortened inter-disc distances in light-adapted retinas compared to dark-adapted retinas. Light-induced rod OS length shrinkage was confirmed using time-lapse light microscopy of isolated rod OSs and histological light microscopy of dark- and light-adapted retinas. TEM revealed that the rod OS length shrinkage was correlated to the light-driven decrease of the space between individual discs, not the disc thickness itself.

4.1 Introduction

Retinal photoreceptors are the cells in which phototransduction converts the light to electrophysiological signals. The process of phototransduction involves multiple cascaded chemical reactions that take place either on the discs or within their compartments in the outer segments (OSs) of the photoreceptors, including the sequential activation of rhodopsin/conopsin, G-protein and phosphodiesterase (PDE), and the hydrolysis of cyclic guanosine monophosphate (cGMP). The decrease in the intracellular cGMP concentration then results in hyperpolarization of the retinal photoreceptors [22,24,75]. Meanwhile, such chemical reactions are accompanied by structural perturbations that may produce stimulus-evoked intrinsic optical signal (IOS) changes in animal [68,70,72,74,86] and human retinas [49]. It is known that rod photoreceptors are more vulnerable than cone photoreceptors in age-related macular degeneration (AMD) [5,9] and retinitis pigmentosa (RP) [103]. Recently, light-induced rod OS shrinkage and orientation movement have been observed in frog and mouse retinas [3,55]. OCT study has also revealed OS shrinkage in human retinas during light adaptation [104]. Comparative microscopy study has indicated that the light-induced OS change can be a primary contributor to the stimulus-evoked IOS [54], and functional IOS distortions have been detected in animal retinas with retinal degeneration [101] and laser-produced dysfunction [52]. Therefore, a better understanding of rod OS responses offers the opportunity for functional imaging of rod physiology to assist with early diagnosis of retinal diseases. Comparative electrophysiological studies of freshly isolated retinas further revealed that such rod OS changes happen before hyperpolarization of the photoreceptors, indicating a disc-based physiological origin [1]. However, whether the

physical origin of OS shrinkage is due to OS discs or interdisc space changes is still unknown.

This study was designed to investigate the light-induced conformational changes of rod OSs at a disc level. Frog (*Rana pipiens*) retinas were selected for this study as the frog rod photoreceptors are relatively large in diameter (~5 - 8 μm) [105] compared to mouse rod photoreceptors (~1 - 3 μm in diameter) [106], allowing unambiguous observations of OSs and relatively precise measurement of the changes in size. Multiple imaging modalities were applied in this study to explore the light-induced shrinkage of rod OSs. Time-lapse light microscopy was first employed to demonstrate the dynamic changes of freshly isolated rod OSs evoked by a visible light stimulus. Comparative histological imaging of dark- and light-adapted retinas were used to confirm the light-induced OS shrinkage. Transmission electron microscopy (TEM) of dark- and light-adapted retinas was employed to investigate the rod OS changes at disc resolution.

4.2 Methods

4.2.1 Sample preparation

Retinal samples from leopard frogs (*Rana pipiens*) were used for this study. For time-lapse microscopic imaging, eight isolated rod OSs were obtained from the isolated retinas of four dark-adapted frogs (Figs. 4.1A, 4.1B). Isolation of the retina was carried out following the protocol that has been reported in our previous publications [1,54]. Individual rod OSs were dissociated from the retina by finely chopping the retina with a razor blade and gently shaking the suspension solution containing the retinal cells and tissues[107,108]. The entire sample preparation was performed in oxygenated Ringer's solution containing 110.0 mM NaCl, 2.5 mM KCl, 1.6 mM MgCl_2 , 1.0 mM CaCl_2 , 22.0 mM

NaHCO₃, 10.0 mM D-glucose with pH 7.3 ~ 7.4 at room temperature (~20 °C). The isolated rod OSs were then transferred to a chamber filled with Ringer's solution for dynamic light microscopic imaging.

For histological imaging analysis, two groups of complete retina-RPE-choroid-sclera complexes, that is, eyecups, were obtained from seven dark-adapted and seven light-adapted frogs (one eyecup from each frog), respectively. The eyecups were then immediately immersed in a fixative solution containing 4% para-formaldehyde (p-FA) and 1% glutaraldehyde (GA) buffered with 0.1 M sodium phosphate, pH 7.3 [109]. All eyecups were fixated for at least 48 hours before cryo-sectioning. For the dark-adapted group, all the procedures were performed in a dark room under dim red light. After fixation, each eyecup was transferred from fixative to 300 μ L 2.3 M sucrose buffered with 0.1 M sodium phosphate (pH 7.3 at 4 °C) for 1 hour and was then embedded and quickly frozen in an optimal cutting temperature compound (Tissue-Tek; Sakura Finetek, Torrance, CA) to facilitate the cutting procedure. After cutting, the retinal samples were thawed, washed, and stained for light microscopic imaging [110].

Another set of cryo-sectioned retinal samples, containing five dark-adapted and five light-adapted retinal samples from 10 different frogs, were further processed for TEM study. The thawing and washing process had been demonstrated to have negligible effect upon photoreceptor ultrastructure, and the acquired images were comparable in quality and the measurements were consistent with other published results [109,111-114]. After being thawed and washed, the retinal samples underwent a secondary fixation (osmication) as the lipid-rich structures (including membranes) were not well preserved by aldehydes [115]. This secondary fixation was performed using osmium tetroxide

(OsO₄), which also helped to stabilize proteins. Samples were then dehydrated through a graded series of ethanol (30%, 50%, 70%, 90%, 95%, and 100%) and were cut with an ultramicrotome diamond knife (Leica Ultracut UCT; Leica Micro- systems, Buffalo Grove, IL) to obtain slices with ~70 nm thickness. Subsequently, specimens were placed on carbon-coated copper grids and stained with alcoholic uranyl acetate [116]. Samples were finally stained with saturated methanolic uranyl acetate (5 minutes) and Venable and Coggeshall's lead citrate (5 minutes) [109]. All experiments in this research followed the protocols approved by the Animal Care Committee (ACC) at the University of Illinois at Chicago, and conformed to the statement on the Use of Animals in Ophthalmic and Vision Research, established by the Association for Research in Vision and Ophthalmology (ARVO).

4.2.2 Experimental setup

A NIR light microscope (BX531 WI; Olympus, Center Valley, PA) with a 60X water immersion objective (UMPLFLN60XW; Olympus, Center Valley, PA) and a CCD camera (Neo 5.5; Andor Technology, Concord, MA) were used to record the light-evoked responses of isolated rod OSs. The visible stimulus was provided by a fiber-coupled light emitting diode (LED; central wavelength: 550 nm, bandwidth: ~200 nm) and was then coupled into the microscope to illuminate the whole sample. The stimulus intensity was empirically set to $\sim 1.13 \times 10^8$ photon/ $\mu\text{m}^{-2}/\text{s}^{-1}$ to enable a robust shrinkage of rod OS. The image acquisition rate was set to 100 frames per second and each imaging trial lasted 3 seconds, including a 1-second pre-stimulus phase, a 1-second stimulus phase, and a 1-second post-stimulus phase. The CCD camera and LED were hardware-synchronized and software-controlled by a custom-designed LabView (National Instrument, Austin, TX)

program. The histological images of retina slices were acquired using a light microscope (Axiovert 100M; Zeiss, Thornwood, NY) and a 20X objective (PlanNeofluar; Zeiss, Thornwood, NY). TEM imaging was achieved using a TEM (JEM-1220; JEOL, Peabody, MA) at 120 kV fitted with a LaB6 electron source and a CCD camera (Es1000W 11MP; Gatan, Weinheim, Germany).

4.2.3 Image processing and data analysis

In the time-lapse light microscopic study, the time course of the shrinkage magnitude of rod OS length and diameter was used to reveal the stimulus-evoked morphological changes of rod OSs (Fig. 4.1(C)). For each recording trial, the length and diameter of the isolated rod OS in each image were measured. Therefore, 300 pairs of the lengths and diameters of the rod OS under monitoring were obtained throughout the experiment with a temporal resolution of 10 ms. The magnitude of rod OS length or diameter shrinkage at a certain time point was considered as the difference between the rod OS length or diameter in the corresponding image and that of the first image.

Both OS and inner segment (IS) lengths were obtained from rod photoreceptors with an intact structure in the histological images of retinas. As the histological images of retinas presented clear structures of retinal cells and different retinal layers (Figs. 4.2(A) and 4.2(B)), the rod OS length was defined as the axial distance between the OS tip and OS/IS intersection, and the rod IS length was the distance between the external limiting membrane (ELM) and the OS/IS intersection. The images were acquired from similar retinal locations (~1.8 mm) relative to the optical nerve head in each eye to avoid intrinsic differences of retinal structures due to different retinal regions. Approximately 20 rod photoreceptors from each eye were selected for measurement. A total number of 260

measurements from 14 eyes (seven dark-adapted and seven light-adapted) were further processed for statistical analysis.

In TEM study, rod OSs with relatively uniform structure (as indicated by black-dashed rectangles in Figs. 4.3(A1) – 4.3(A3)) were first selected from TEM images with low magnification (4 kX). These rod OSs then underwent imaging with high magnification (150 kX) and local regions with parallel discs (Fig. 4.3(B)) presented were further selected for inter- and intradisc distance measurement. As shown in Figure 4.3(D), the interdisc distance is defined as the distance between the disc membranes of two adjacent discs, and the intradisc distance is defined as the thickness, including the lipid bilayers, of the disc. The TEM images used for measurements were acquired at magnifications of 150 kX with a pixel resolution of 0.36 nm/pixel. Each TEM image was divided into 400 subwindows and 10 of them were randomly selected for measurement to minimize the personal preference of the observer. Given the nanometer level resolution of TEM, edges of the discs could be clearly identified, which further enabled solid quantification of geometric variations of the discs. One interdisc distance and one intradisc distance was then obtained from each of the 10 subwindows. The inter- and intradisc distances were further categorized into three groups, that is, tip, middle, and base, according to the corresponding disc location in the rod OS (Fig. 4.3(A1)). As a result, a total of ~1000 measurements of interdisc distance were obtained and the same amount of measurements of intradisc distances were evenly collected from the tip, middle, and base regions of 62 individual rods of five dark-adapted and five light-adapted retinal samples (e.g., ~160 measurements of intradisc distances from the tip region of dark-adapted rod

OS). Kolmogorov-Smirnov tests were performed to validate the normality of the measurements. Data sets were expressed as the mean and standard deviation.

Based on the measurements obtained from histological and TEM images of rod OSs, the shrinkage ratio was defined to investigate the relationship between the overall rod OS shrinkage and the structural perturbation of disc stacks, respectively. In the histological study, the light-induced shrinkage ratio was defined as:

$$(\overline{OSL}_D - \overline{OSL}_L) / \overline{OSL}_D \quad (13)$$

where \overline{OSL}_D is the averaged rod OS length in dark-adapted samples and \overline{OSL}_L is the averaged rod OS length in light-adapted samples. In the TEM study, the light-induced shrinkage ratio in a disc stack containing N discs was defined as:

$$[N \cdot (d_{interD} + d_{intraD}) - N \cdot (d_{interL} + d_{intraL})] / [N \cdot (d_{interD} + d_{intraD})] \quad (14)$$

where d_{interD} and d_{interL} are the interdisc distance in dark- and light-adapted samples, respectively, and d_{intraD} and d_{intraL} are the intradisc distances in dark- and light-adapted samples, respectively.

4.3 Results

4.3.1 Time-lapse light microscopy of rod OS shrinkage

In this study, time-lapse light microscopy was employed to provide direct observation of the rod OS length shrinkage evoked by a visible light stimulus. Figure 1(A) shows time-lapse light microscopic images of a representative single isolated rod OS obtained before, during, and after a 1-second stimulus. The onset time of the stimulus was set as time 0 second. Figure 4.1(B) provides an enlarged illustration of the images of the rod OS tips indicated by the white rectangle in Figure 4.1(A). As shown in Figure 4.1(B), the increased

distance between the tip of the rod OS and the black-dashed line demonstrates a significant length shrinkage of the rod OS after the onset of the stimulus (also see the Supplementary Movie 1 and 2). The averaged magnitude of rod OS length and diameter shrinkage over time (from eight isolated rod OSs from four retinas) are shown in Figure 4.1(C). The waveform of the length shrinkage shows a stable and flat stage before the stimulus presentation and a rapid rise upon the stimulus initiation, indicating the length shrinkage is directly correlated with the stimulus. However, the flat waveform of the diameter shrinkage showed that the rod OS diameter was not affected by the stimulation and maintained a consistent scale during the experiment. The relationship of the standard deviation amplitudes to the mean waveform reflects a general similarity of the stimulus-evoked responses observed from different rod OSs.

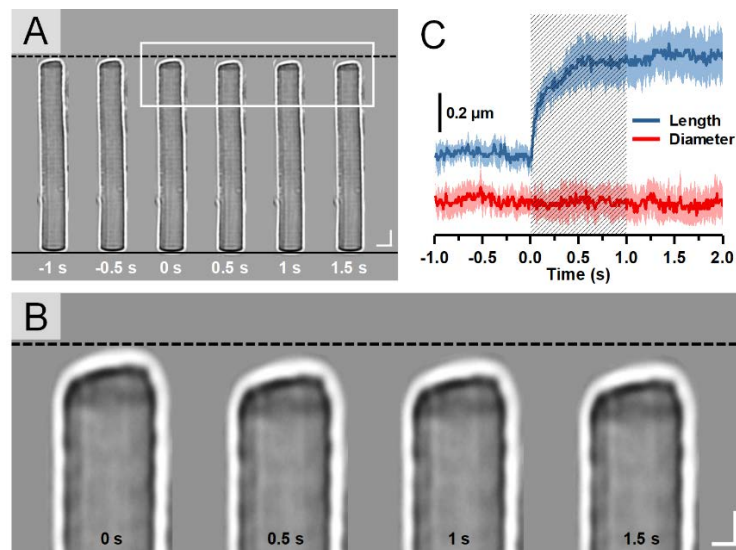


Fig. 4.1. (A) Representative light microscopic images of a single isolated rod OS acquired with an interval of 0.5 seconds. To better show the light-evoked OS shrinkage, the base of the rod OS in each image is aligned horizontally as shown by the black solid line at the bottom. The black-dashed line at the top represents the position of the rod OS tip at time -1 second. Scale bars (in white) represent $5\ \mu\text{m}$. (B) Enlarged picture of the white rectangle in A. Scale bars (in white) represent $2\ \mu\text{m}$. (C) Time course of the averaged rod OS shrinkage in both length and diameter acquired from eight different rod OSs. Colored areas accompanying the curves represent the standard deviations. Shaded area indicates the 1-second stimulation period.

4.3.2 Comparative histological study of the retina in dark- and light-adapted Eyes

To verify the light-induced length shrinkage of rod OSs in the intact retina, histological examinations were conducted on dark- and light-adapted frog eyes. Figures 4.2(A) and 4.2(B) show representative transmission microscopic images of eyecup slices from dark- and light-adapted eyes, respectively. As shown in the images, two retinas exhibited a similar overall thickness and comparable locations of the ELM and outer plexiform layer (OPL). As Bruch's membrane (BrM) layers in the two images were horizontally aligned (marked by the red-dashed line), the light-adapted retina presented significantly increased distances between the rod OS tips (marked by the yellow- dashed line) and BrM, compared to that of the dark- adapted retina (the distance between green- and red-dashed lines). To validate the reliability and repeat- ability of the observations, the lengths of rod OSs were measured from a total of 260 retinal locations in seven pairs of dark- and light-adapted frog eyes. The corresponding rod IS length was also measured from the same retinal locations as a reference. The statistical results shown in Figures 4.2(C) and 4.2(D) revealed that rod OS lengths were significantly reduced in light-adapted eyes ($51.8 \pm 4.5 \mu\text{m}$) compared to those of dark-adapted eyes ($56.9 \pm 3.9 \mu\text{m}$). However, the differences between rod IS lengths were not significant ($24.4 \pm 3.1 \mu\text{m}$ and $25.4 \pm 3.6 \mu\text{m}$ in dark- and light-adapted eyes, respectively).

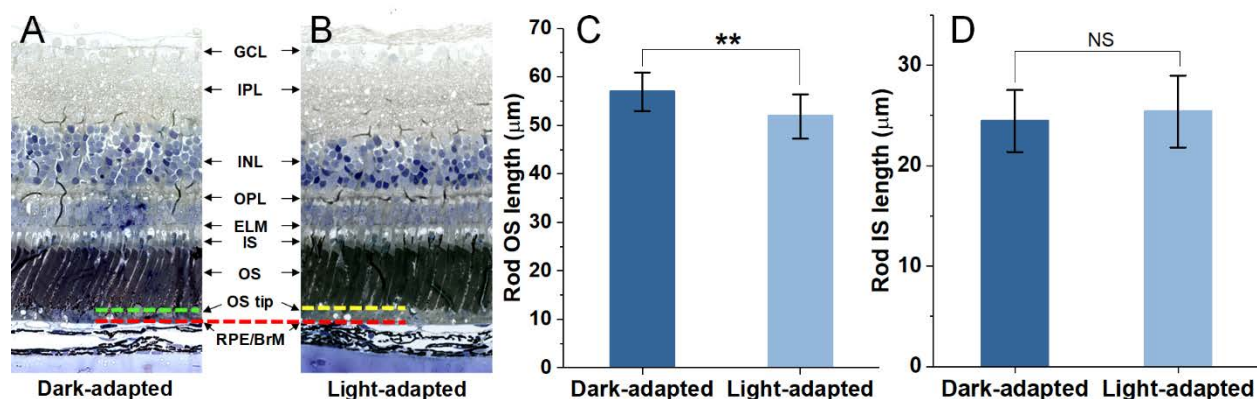


Fig. 4.2. Histological images of eyecups from the dark-adapted eye (A), and the light-adapted eye (B). The green dashed line in A and the yellow-dashed line in (B) represent the general position of OS tips in dark- and light-adapted samples, respectively. The red-dashed line indicates BrM. Statistics of rod OS length (C) and IS length (D) in dark- and light-adapted samples. For each group of data, a total of ~130 measurements were obtained from seven retinas. Data are the mean and standard deviation. Significance was determined with two-tailed Student's t-test with ** $p < 0.05$; NS, not significant. GCL, ganglion cell layer; IPL, inner plexiform layer; INL, inner nuclear layer; RPE, retinal pigment epithelium.

4.3.3 Comparative TEM study of rod discs in dark- and light-adapted eyes

As previous time-lapse light microscopic and histological studies have confirmed the light-induced length decreases in rod OSs, the following aim of this study was to disclose the anatomic source of the rod OS shrinkage on a subcellular level. Our previous studies suggested the conformational change of rod OSs was correlated with the phototransduction cascades on or adjacent to the discs. Therefore, we hypothesized the overall rod OS shrinkage was related to the perturbation of the lamellar structure of the rod discs. To verify the hypothesis, comparative TEM studies were conducted on rod OSs under light- and dark-adapted conditions. Figures 4.3(A1) to 4.3(A3) show representative overall views of the photoreceptors under TEM in which individual rods can be clearly identified. Figure 4.3(B) shows the well-preserved lamellar structure of the discs in the white rectangle in Figure 4.3(A3), obtained with high TEM magnification. Figures 4.3(C1) and 4.3(C2) are representative TEM images of disc stacks in the dark- and light-adapted

rod OSs, respectively. To provide a direct impression of how light illumination changed the lamellar structure of the discs, two blue bars, with each bar covering 15 discs, were placed in the images with their bottoms horizontally aligned. The blue bar in the light-adapted rod OS is significantly shorter in length, compared with that in the dark-adapted rod OS, indicating the light adaptation reduced the length of the disc stacks. As shown in Figure 4.3(D), to demonstrate whether the reduction in length came from the distance between the discs (interdisc distance), the disc itself (intradisc distance) or from both, the inter- and intradisc distances were measured in both dark- and light-adapted samples and statistically compared to illustrate the difference. Further, the inter- and intradisc distances were compared based on their relative locations, that is, tip, middle, or base region (Fig. 4.3(A1)), in the rod OSs. The means and standard deviations of the measurements are summarized in Table 4.1. As shown in Figures 4.3(E1) to 4.3(E3), the statistical analysis demonstrated that the light illumination resulted in a significant decrease in the interdisc distances from all three regions and the overall interdisc distance, but barely affected the intradisc distances.

Table 4.1. Means and standard deviations of the inter- and intra-disc distances measured from tip, middle and base regions of dark- and light-adapted rod photoreceptors.

		Tip	Middle	Base	Avg.
Dark-adapted	Inter-disc	7.15 ± 1.64	6.98 ± 1.40	7.69 ± 1.55	7.38 ± 1.61
	Intra-disc	14.71 ± 2.07	14.17 ± 1.67	14.36 ± 1.98	14.46 ± 1.92
Light-adapted	Inter-disc	5.04 ± 0.99	5.17 ± 1.02	5.55 ± 1.34	5.28 ± 1.21
	Intra-disc	14.18 ± 1.60	14.43 ± 1.32	14.62 ± 1.60	14.36 ± 1.51

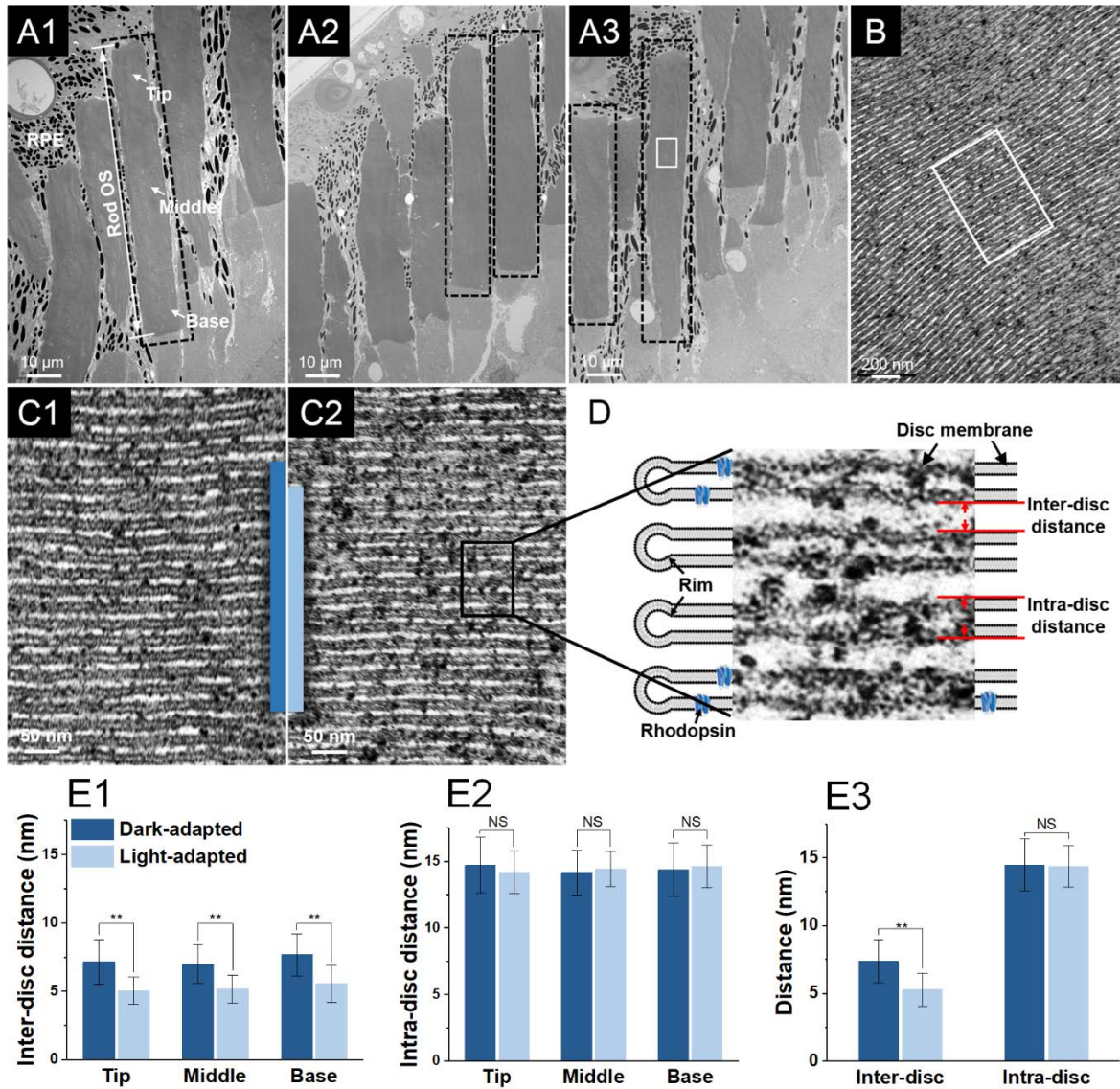


Fig. 4.3. TEM study of rod OSs. (A1–A3) Representative TEM images of a frog retina, including photoreceptors, RPE cells, and melanosomes (black particles), at low magnification (4 kX). The tip, middle, and base regions of the rod OSs are as indicated in A1. The black-dashed rectangles demonstrate the rod OSs with relatively uniform structure. (B) TEM image of the lamellar structure of discs in the white rectangle in A3 obtained with a magnification of 150 kX. (C1) Enlarged image of the discs in the white rectangle in B (dark-adapted sample). (C2) Corresponding TEM image of the discs from a light-adapted sample, obtained with same TEM magnification. (D) Cartoon and TEM image illustration of the rod OS discs and the corresponding inter- and intradisc distances. Statistics of interdisc distances (E1) and intradisc distances (E2) in the tip, middle, and base regions of rod OSs in dark- and light-adapted samples. $n = 5$ for each bar. (E3) Statistics of inter- and intradisc distances in dark- and light-adapted samples. $n = 5$ for each bar. Data are the mean and standard deviation. Significance was determined with a two-tailed Student's *t*-test with ** $p < 0.05$; NS, not significant.

4.4 Discussion

In this study, we employed multiple imaging modalities to explore the anatomic source of light-correlated rod OS shrinkage. Using time-lapse light microscopy, we directly observed robust length shrinkage in single isolated rod OSs when a visible light stimulus was applied (Fig. 4.1). As the rod IS was absent in this experiment, we verified that the rod OS itself can trigger the shrinkage. However, as the behavior of rod photoreceptors could be vulnerable in an *in vitro* environment, the light-induced structural changes were further investigated in the intact retina by comparing the histological sections of retinas from dark- and light-adapted eyes. Benefiting from the high spatial resolution of light microscopic images, the structure of the retina can be clearly identified, enabling precise measurement of rod OS and IS lengths. The statistical analysis proved that light illumination introduced a significant length decrease in rod OSs but did not affect the length of rod ISs. Moreover, the rapid time course, that is, almost immediate onset time of the shrinkage, and the rapid time-to-peak of the shrinkage shown in Figure 4.1(C) do not favorably support the possible causes related to the relatively slow physiological processes, such as translocation of signaling proteins [117] and apical process of RPE cells [110,118]. Combining these observations, our results suggested that the mechanical origin of OS length shrinkage was within the OS.

To further explore the structural changes within the rod OSs, TEM was employed to provide images of disc stacks with resolution at the nanometer level. TEM images obtained in this study exhibited the lamellar structure of the rod discs and provided clear identification of the disc membranes and the spaces within the discs (white areas between disc membranes) (Figs. 4.3(B), 4.3(C1), 4.3(C2)) [19]. Two dimensions, the inter- and

intradisc distance, that is, the thickness of the disc and distance between the discs, were then quantified to illustrate the perturbation. To reflect the general configuration of the discs, OS regions with the structure of paralleled discs were selected to measure the inter- and intradisc distances for our statistical analysis. Sampling from these regions principally guaranteed the continuity and reliability of the measurements by avoiding structural distortions caused by artifacts from the sample preparation. We also noted that the fixation processing during the retinal preparation could potentially introduce dimensional changes to the samples, but its influence on the reliability of the result was minimized as all our dark- and light-adapted samples underwent exactly the same fixation procedures. The structure of rod OS discs presented, and the inter- and intradisc distance measured in this study were also consistent with previous publications [112,113,119,120]. As a result, the interdisc distance was found to present a significant shrinkage rather than the intradisc distance. In addition, the inter- and intra-disc distances at different locations, that is, tip, middle, and base regions, of the rod OSs were compared. The results showed that a significant decrease was consistently observed in the interdisc distances of all three regions, indicating the shrinkage was a general phenomenon along the axial direction of the rod OSs. Therefore, the rod OS shrinkage observed in this study was caused by the reduction of interdisc space, not changes in the discs themselves that were related with osmotic volume change [82] or lateral expansion of the disc membranes proposed in previous studies [87].

The shrinkage ratio of rod OSs obtained in the histological study was similar to that of the disc stacks in the TEM study. As defined by equations (1) and (2), the shrinkage ratio of rod OSs in the histological study was ~ 0.089 and the shrinkage ratio of disc stacks in

the TEM study was ~ 0.101 (calculated by the means of corresponding data). As the disc stacks (include both inter- and intradisc space) occupy most of the photoreceptor OS, such similarity further suggests that the overall rod OS length shrinkage was correlated with the reduction of the space between discs. Because the rhodopsin, transducin and PDE are anchored to the lipid bilayer of the disc, the shrinkage in the interdisc space then must have a more direct correlation with the cascaded reactions happening between the discs.

Furthermore, different from the shrinkage in rod OS length, we did not observe any reliable changes in the diameters of the isolated rod OSs before, during, or after the light stimulus, indicating the total volume of the rod OS was reduced during the shrinkage (Fig. 4.1(C)). However, the reduction in rod OS volume was unlikely related to the intracellular osmotic change caused by the light-induced closure of cGMP-gated ion channels. Evidence can be found in our previous observation of persistent light-induced rod OS movement, which was associated with unbalanced OS shrinkage, in a low-sodium medium [1]. Therefore, the interdisc space shrinkage is probably not a consequence of the blockage of rod circulating current and must have a more complicated mechanism [83,119,121].

In summary, this study confirmed the light-induced rod OS shrinkage with multiple imaging modalities and demonstrated its anatomical origin was correlated with a reduction of the interdisc space, instead of the thickness of the disc itself, in the rod OS. Better understanding of the principle behind the OS shrinkage will not only benefit our knowledge of the phototransduction, but also may provide insights for instrument design to achieve functional imaging of photoreceptor physiology.

Acknowledgements

The authors thank Xiang Shen at Lions of Illinois Eye Research Institute for the cryo-section of the retinal sample, and Figen A. Seiler at the Research Resource Center of UIC for the retinal sample preparation and TEM imaging. Supported by NIH grants R01 EY023522, R01 EY024628, and P30 EY001792; by an unrestricted grant from Research to Prevent Blindness; and by Richard and Loan Hill endowment.

CHAPTER V. *IN VIVO* SUPER-RESOLUTION IMAGING OF TRANSIENT RETINAL PHOTOTROPISM EVOKED BY OBLIQUE LIGHT STIMULATION

(Previously published as Yiming Lu, Changgeng Liu, Xincheng Yao, *In vivo* super-resolution imaging of transient retinal phototropism evoked by oblique light stimulation, Journal of Biomedical Optics 23(5), 050502 (2018) [3])

Abstract: Rod-dominated transient retinal phototropism (TRP) has been observed in freshly isolated retinas, promising a noninvasive biomarker for objective assessment of retinal physiology. However, *in vivo* mapping of TRP is challenging due to its subcellular signal magnitude and fast time course. We report here a virtually structured detection-based super-resolution ophthalmoscope to achieve subcellular spatial resolution and millisecond temporal resolution for *in vivo* imaging of TRP. Spatiotemporal properties of *in vivo* TRP were characterized corresponding to variable light intensity stimuli, confirming that TRP is tightly correlated with early stages of phototransduction.

5.1 Introduction

It has been well established that many eye diseases, such as age-related macular degeneration (AMD) and retinitis pigmentosa (RP), can impair retinal photoreceptors and inner neurons to cause vision loss [5,92]. As physiological abnormalities may occur before detectable morphological distortions, functional imaging of retinal physiology is essential for early diagnosis of eye diseases and reliable assessment of treatment outcomes. Although psychophysical and electrophysiological methods can be used for functional examination of the visual system, they suffer from low signal specificity or insufficient spatial resolution [122-125]. Therefore, a high-resolution method for objective

examination of photoreceptor physiology is desirable to advance early diagnosis of AMD, RP, etc. Particularly, rod photoreceptors are known to be more vulnerable, compared with cone photoreceptors, in early AMD and RP [5,92].

Rod-dominated transient retinal phototropism (TRP) has been recently observed in freshly isolated amphibian and mammal retinas stimulated by oblique visible light illumination [54]. Functional OCT of living eye-cups and time-lapse microscopy of retinal slices revealed that TRP has an anatomic origin within the outer segment (OS) [56], presumably caused by localized shrinkage of rod OSs [55]. Comparative electrophysiological investigation into isolated retina further identified the physiological source of TRP to the phototransduction processes before hyperpolarization of the rod photoreceptor [1]. Therefore, TRP provides a noninvasive biomarker for objective assessment of rod function, promising a high-resolution method for early detection of AMD, RP, etc. However, *in vivo* mapping of the rod-dominated TRP is challenging due to its rapid time course and subcellular movement magnitude [1,54,55].

We recently demonstrated a super-resolution scanning laser ophthalmoscope for *in vivo* imaging of frog retina [126]. The custom-designed ophthalmoscope employed virtually structured detection (VSD) to achieve subcellular level spatial resolution, and it combined a rapid line-scan strategy to realize millisecond-level temporal resolution. In this paper, we report the first *in vivo* observation of TRP using the VSD-based line-scan super-resolution ophthalmoscope. Temporal dynamics of *in vivo* TRP correlated with variable stimulus intensities was characterized to verify the physiological origin of TRP [127].

5.2 Methods

Adult northern leopard frogs (*Rana Pipiens*) were used for this study. The frogs were first dark-adapted for at least 4 hours prior to *in vivo* imaging and then anesthetized through the skin. After confirmation of anesthesia, the frog was fixed in a custom-built holder and the pupils were fully dilated with topical atropine (1%) and phenylephrine (2.5%) for *in vivo* imaging. All experiments in this research were performed following the protocols approved by the Animal Care Committee at the University of Illinois at Chicago, and conformed to the statement on the use of animals in ophthalmic and vision research, established by the Association for Research in Vision and Ophthalmology.

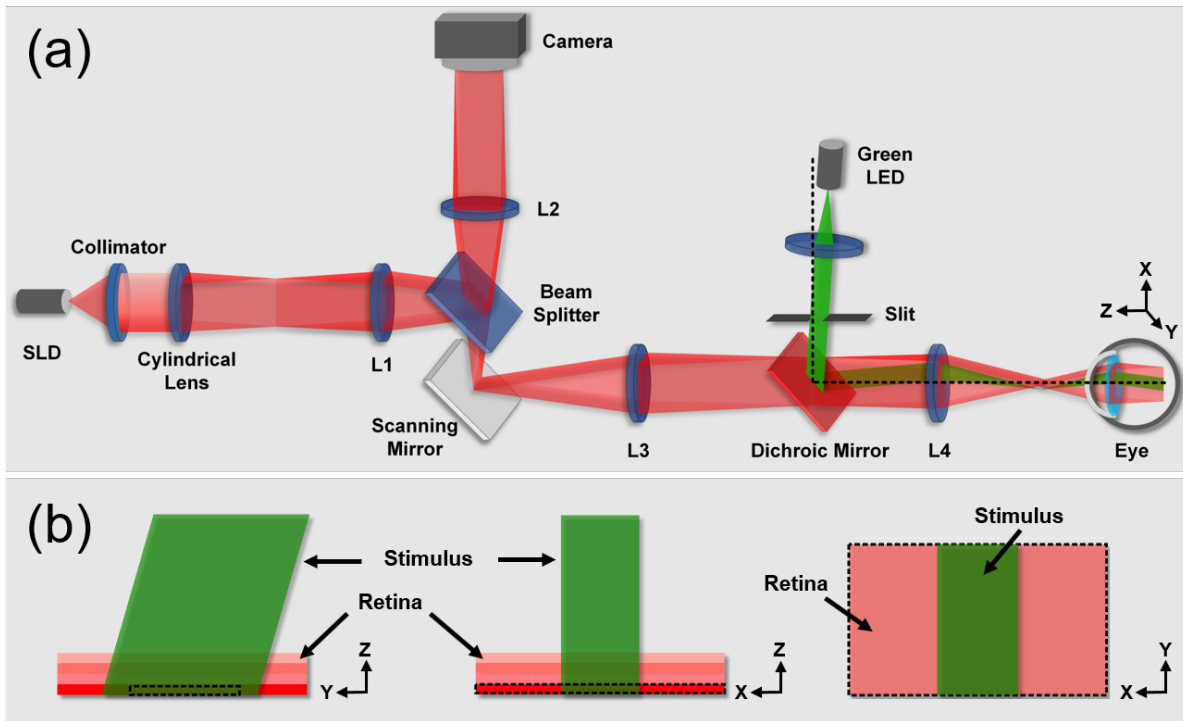


Fig. 5.1. (a) Schematic of the line-scan ophthalmoscope for *in vivo* super-resolution imaging. The illumination for retinal imaging is produced by a SLD. The line profile of illumination scanned across the retina is produced by the cylindrical lens. L1–L4 are lenses with focal lengths of 80, 400, 80, and 25 mm, respectively. The black-dashed line represents the virtual optical axis for a perpendicular stimulation on the retina. The oblique stimulation is then achieved by applying an “off-axis” setup in the stimulation path. (b) Illustration of the oblique stimulation and retina: right-side view (left), front view (middle), and top view (right) of the oblique stimulation and retina. The black-dashed rectangles

represent the imaging area on the photoreceptor layer of retina. (a) and (b) Share the same coordinates.

Figure 5.1(a) shows a schematic diagram of the line-scan super-resolution ophthalmoscope. The light source is a near-infrared superluminescent diode (SLD-35-HP; Superlum Ireland, Inc.) with a center wavelength at 830 nm and a bandwidth of 60 nm. The light entering the frog pupil had a ~2 mm beam diameter, with a ~2.5 mW power. A focused line in the X-direction, produced by a cylindrical lens, scanned across the retina in the Y-direction under the control of a scanning galvanometer mirror (GVS001; Thorlabs, Inc.). Due to the line focus illumination and microsecond-level exposure time, the illumination power applied to the retina was well below the maximum permissible exposure determined by the ANSI and IEC laser safety standards [128-130]. The line profile reflected from the retina was recorded by a high-speed two-dimensional (2-D) CMOS camera (FastCam Mini AX50; Photron, Inc.). To achieve fast recording speed for *in vivo* imaging, the line scanning was performed in one dimension (Y-direction) for super-resolution imaging. A total of 255 line-profiles were acquired to reconstruct one super-resolution image. In this experiment, the imaging speed of the camera was set at 30,000 frames/s (fps), corresponding to a 100-fps speed for VSD-based super-resolution imaging.

A fiber-coupled light-emitting diode with a central wavelength at 505 nm (M505F1; Thorlabs, Inc.) was employed to produce the green flash used for retinal stimulation. The visible stimulation was obliquely delivered to the retina to elicit TRP (Fig. 5.1(b)) and its incident angle on the retina was adjusted by a kinetic mount (KC1; Thorlabs, Inc.) that held both the fiber tip and the collimator. To better distinguish the stimulus-evoked photoreceptor movement from background, only the retinal area at the center of the field of view was illuminated by the visible stimulation (middle and left panel in Fig. 5.1(b)). The

localized stimulation was achieved by placing a slit at the conjugate plane of the retina in the stimulation path (Fig. 5.1(a)). The stimulating power was first measured by a power meter (PM200; Thorlabs, Inc.) placed at the rear focal plane of the lens before the eye (L4 in Fig. 5.1(a)) and was then converted to stimulation intensity on the retina [131].

5.3 Results

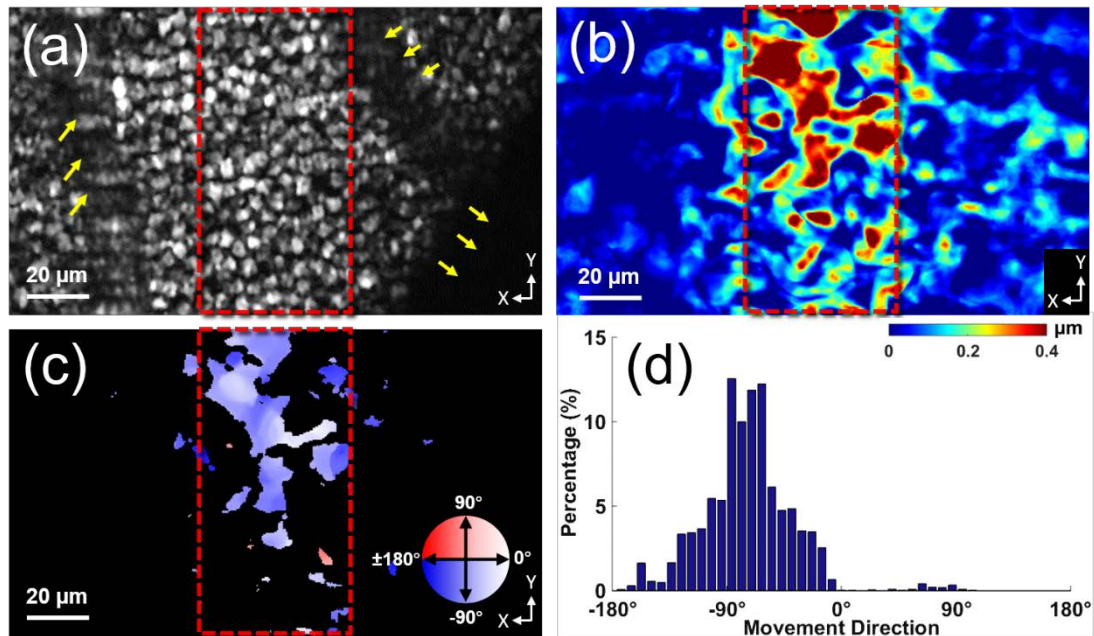


Fig. 5.2. *In vivo* TRP evoked by a localized oblique stimulation. (a) Representative *in vivo* super-resolution image of the photoreceptor layer (Video 1). Yellow arrowheads indicate retinal blood vessels. Representative magnitude map (b) and direction map (c) of photoreceptor movement recorded at time 0.4 s after the onset of stimulation. The inset color map in (c) shows the colors that represent different movement directions. The black area represents the retinal locations where no reliable movements can be detected. The red-dashed rectangles in (a), (b), and (c) represent the stimulated retinal area. (d) Histogram of movement directions in (c). (a), (b), and (c) Share the same coordinates with Fig. 5.1 (Video 1, MPEG, 287 KB (URL: <https://doi.org/10.1117/1.JBO.23.5.050502.1>)).

Figure 5.2 shows *in vivo* TRP correlated with oblique visible stimulation. Figure 5.2(a) shows a representative image of the photoreceptor layer acquired by the VSD-based super-resolution ophthalmoscope with an imaging speed of 100 frames/s and a field of view of 100 μm × 200 μm on the retina. Individual photoreceptors were clearly imaged

with subcellular spatial resolution and millisecond temporal resolution, which allowed quantitative measurement and dynamic monitoring of photoreceptor movements. To elicit TRP, a rectangular stimulation pattern was obliquely projected onto the retina and stimulated a retinal area that has a width of $\sim 50\ \mu\text{m}$ at the center of the field of view (red-dashed rectangle in Fig. 5.2(a)).

To quantify TRP, we calculated the magnitude and direction map of photoreceptor movements based on the retinal images using the optical flow code developed by *Sun et al* [53]. Optical flow is a well-established method for measuring object movements between two images. Therefore, it can accurately identify the process of photoreceptor movement through sequential retinal images [1,56]. A $3\text{-}\sigma$ threshold and a temporal window generated from the movement magnitude maps were applied to exclude potential spatial and temporal noise in the movement direction map [1,73]. Figures 5.2(b) and 5.2(c) are representative magnitude and direction map of the photoreceptor movements evoked by the localized stimulation. As Figs. 5.2(b) and 5.2(c) match Fig. 5.2(a), the red-dashed rectangles shown in Figs. 5.2(b) and 5.2(c) also represent the stimulated retinal area. Therefore, Figs. 5.2(b) and 5.2(c) reveal that robust photoreceptor movements were primarily confined within the stimulated retinal region. The distribution of movement direction in Fig. 5.2(c) was further analyzed to illustrate the correlation between the directions of photoreceptor movements and oblique stimulation. As shown in Fig. 5.2(d), most stimulus-evoked photoreceptor movements had a direction close to -90° , indicating the photoreceptors moved toward the incident stimulation, which was consistent with our previous *in vitro* observation of TRP [1,54,56].

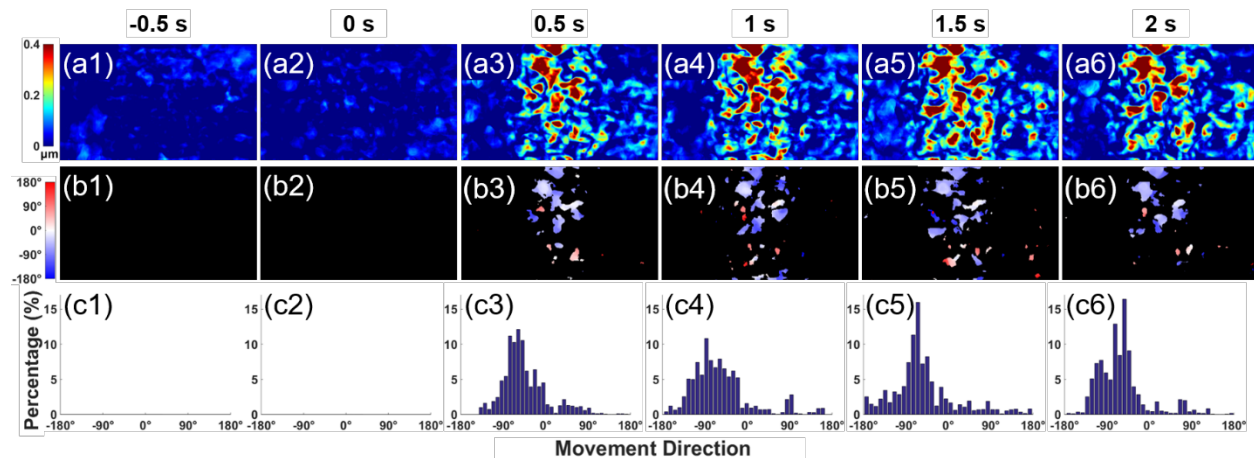


Fig. 5.3. Spatiotemporal dynamics of *in vivo* TRP evoked by localized oblique stimulation. Magnitude maps of photoreceptor movement obtained before (a1–a2), during (a3), and after (a4–a6) the stimulation (Video 2). Direction maps of photoreceptor movement obtained before (b1–b2), during (b3), and after (b4–b6) the stimulation (Video 3). (c) Histograms of the movement direction corresponded to the movement direction maps in (b). The stimulation started at time 0 s and lasted for 500 ms (Video 2, MPEG, 791 KB [URL: <https://doi.org/10.1117/1.JBO.23.5.050502.2>]; Video 3, MPEG, 336 KB (URL: <https://doi.org/10.1117/1.JBO.23.5.050502.3>)).

To illustrate the spatiotemporal dynamics of TRP, representative magnitude and direction maps of photoreceptor movement selected from different phases of the experiment are shown in Fig. 5.3. As the stimulation onset was set as 0 s and the stimulation period lasted for 0.5 s, Fig. 5.3 covers the photoreceptor movements before, during, and after the stimulation. Figure 5.3(a) demonstrates that robust photoreceptor movements were only observed after the onset of stimulation and within the stimulated retinal area. Figures 5.3(b) and 5.3(c) further proved the direction of stimulus-evoked photoreceptor movement was consistently toward the direction of incident stimulation during and after the stimulation period. It was also noticed that some of the stimulated retinal regions did not present reliable movements during the recording period and some other regions presented opposite movement direction at certain time points (pink areas in Figs. 5.2(c) and 5.3(b)). Similar phenomena were observed in our previous *in vitro* TRP

studies using different imaging modalities, including OCT, confocal, and light microscopies [1,56]. These phenomena are speculated to be related to the complex structure of the retina, and accurate oblique stimulation and actual intensity control for each single photoreceptor are difficult due to inevitable light scattering and coherent mechanical interaction among neighboring photoreceptors.

The correlation between photoreceptor movement magnitude and stimulation intensity was further investigated. Three stimulation intensities, i.e., 1.97×10^5 , 0.67×10^5 , and 0.197×10^5 photons $\cdot \mu\text{m}^{-2} \cdot \text{ms}^{-1}$, were tested as a pilot study. Our previous *in vivo* intrinsic optical signal (IOS) studies showed such stimulations could activate significant but different retinal responses [52]. The flash duration was set to 500 ms for eliciting robust photoreceptor movements. As the line-scan modality fulfilled a fast recording speed, a time-magnitude course was used to reflect the dynamics of photoreceptors with a 10-ms temporal resolution [1]. Figure 4 shows the results obtained from a group of six samples. Each trace in Fig. 5.4(a) is the mean of 12 time-magnitude courses and is accompanied by the standard deviations of data about the mean (colored area). The relationship of the standard deviation amplitudes to the waveform in each trace indicates general similarity between the results obtained from different samples. The waveforms of all three traces are flat and stable in the pre-stimulus phase and exhibit an immediate and significant rise upon the initiation of the stimulation. However, the waveforms also show that different stimulation intensity remarkably changed the response of the photoreceptor.

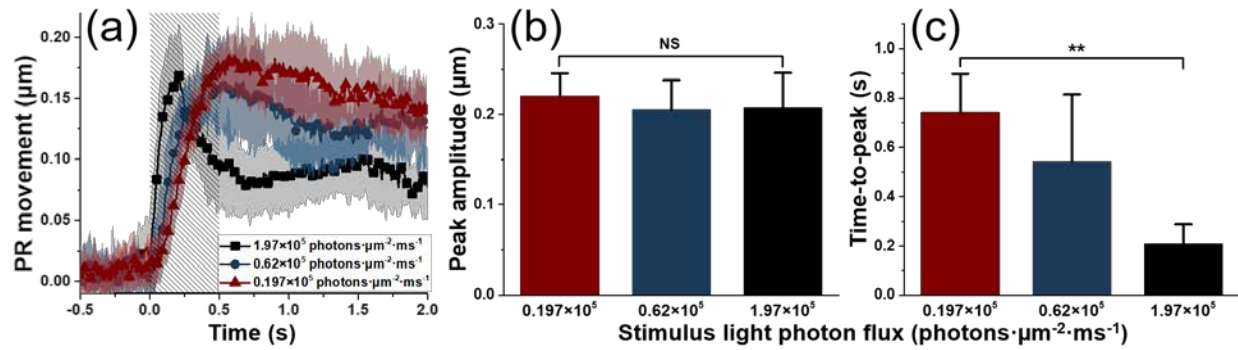


Fig. 5.4. Characteristics of photoreceptor movement correlated with stimulation intensities. (a) The time-magnitude courses of photoreceptor movement corresponded to three increasing stimulation intensities as, respectively, indicated by the legend. Each trace is an average of 12 datasets recorded from six different retinal samples. The colored area that accompanies each trace illustrates the standard deviations. Shaded area represents the 500-ms stimulation. PR: photoreceptor. The means and standard deviations of peak amplitude (b) and time-to-peak (c) of the traces in (a). Significance was determined by a one-way ANOVA with post-hoc Tukey honestly significant difference test for multiple comparisons, ** $p < 0.01$, NS, not significant, $n = 12$ retinal locations for each stimulus intensity.

To better illustrate the difference caused by increasing stimulation intensity, two parameters, peak amplitude (the maximum value of photoreceptor movement magnitude) and time-to-peak (time taken to reach the peak amplitude) of the waveforms, were compared. The results in Fig. 5.4(b) show that the difference between peak amplitudes of the three traces was statistically insignificant, suggesting the peak amplitude is irrelevant to the variation of stimulation intensities within a certain range. However, as shown in Fig. 5.4(c), the time-to-peak values were significantly reduced by higher stimulus intensity, indicating brighter stimulus results in earlier saturation of the photoreceptor movement. These results suggested an intimate correlation between photoreceptor movement and phototransduction as the accelerated photoreceptor response might be the consequence of more rhodopsin and additional amounts of cascaded reactions activated by strong stimulation [24]. Similar effects were observed in our previous IOS and rod OS shrinkage studies, supporting that photoreceptor movement is a major

component of IOS and the unbalanced rod OS shrinkage is the mechanical source of TRP [46,52,55].

5.4 Discussion

In summary, this study demonstrated the feasibility of using a line-scan VSD-based super-resolution ophthalmoscope for *in vivo* imaging of TRP. Compared with traditional structure illumination microscopy, the VSD-based approach provides a compact, cost-efficient, and phase-artifact-free strategy to achieve super-resolution retinal imaging. The line-scan imaging modality achieved a fast recording speed for retinal activity. Corresponding to variable light intensity stimuli, it was observed that the TRP peak amplitude was not significantly sensitive to the stimulus light intensity, whereas TRP time-to-peak value was significantly sensitive to stimulus light intensity, i.e., reduced time-to-peak value corresponding to enhanced stimulus intensity. This observation indicates that the rod-dominated TRP was closely related to phototransduction in rod photoreceptors, and therefore reflected the functionality of rod photoreceptors. Further investigation of the *in vivo* properties of TRP may provide a high spatial resolution IOS imaging method for functional mapping of rod physiology. Our recent study has revealed a tight correlation between stimulus-evoked TRP and photoreceptor IOS changes in freshly isolated retinal tissues [54]. Previous studies have revealed IOS changes in both photoreceptors and inner retinal layers [74,77,132,133], and emerging functional OCT enabled depth-resolved detection of photoreceptor IOS from inner retinal IOSs [46,73]. We anticipate that better investigation of the *in vivo* properties, including physical and physiological mechanisms and spatial and temporal dynamics, of stimulus-evoked TRP in animal models will provide valuable information for advanced instrument development and better

stimulation protocol designs for pursuing *in vivo* IOS imaging of human retina, enabling early detection of AMD, in which rod photoreceptor dysfunction occurs first, and other eye diseases.

Acknowledgments

This research was supported in part by NIH R01 EY023522, NIH R01 EY024628, and NIH P30 EY001792.

CHAPTER VI. *IN VIVO* SUPER-RESOLUTION IMAGING OF HUMAN RETINA WITH VIRTUALLY STRUCTURED DETECTION

Abstract: High-resolution imaging of human retina is important for the clinical diagnosis of eye diseases. In this work, we integrated virtually structured detection (VSD) technique with scanning laser ophthalmoscopy to achieve an *in vivo* super-resolution imaging of human retina. The VSD technique allows a digital implementation of super-resolution imaging. It largely improves system compactness and facilitates a phase-artifact free approach to achieve super-resolution imaging. A line-scanning imaging modality was employed to improve the temporal resolution and the two-dimensional sub-frame images acquired at a frame rate of 25 kHz level allow an explicit registration of intra-frame eye movements. By using these techniques, we demonstrated *in vivo* super-resolution imaging of human cone photoreceptors at different foveal eccentricities with millisecond-level temporal resolution and minimum intra-frame distortions.

6.1 Introduction

In vivo visualization of human retinal structures is important for clinical diagnosis of retinal diseases. However, high-resolution retinal imaging has been challenging due to the relatively low numerical aperture, aberration and rapid movement of human eye. Adaptive optics (AO) has been applied to compensate the aberration of the eye and has successfully enabled a desirable identification of retinal structures, such as photoreceptors, ganglion cells and nerve fibers [134,135]. However, the AO system is complex and requires pupil dilation to achieve high resolution. Therefore, the clinical deployment of AO is limited. Scanning-based AO imaging modalities, such as AO scanning laser ophthalmoscopy (AO-SLO) and AO optical coherence tomography (AO-

OCT), can also be vulnerable for the eye movements. Though multiple image registration algorithms have been developed to remove the inter-frame distortion, it is still difficult for the scanning-based AO to remove the intra-frame distortions when a ground truth reference is inaccessible and the overall registration quality can be affected as the selected reference frame is not necessarily free from intra-frame distortion [60,61].

Structured illumination microscopy (SIM) improves the imaging resolution by involving extended bandwidth of the spatial frequency of the sample to surpass the diffraction-limited resolution. It has been widely applied in super-resolution imaging of biological tissues [63,64,136]. However, the realization of super-resolution imaging by SIM requires a complicated modulation of the illumination pattern and a relatively static sample [137,138]. Therefore, a direct application of SIM for *in vivo* retinal imaging is challenging.

Virtually structured detection (VSD) based scanning laser microscopy (SLM) provides an alternative way to achieve equivalent SIM. The VSD approach does not require physical modulation of the illumination pattern. Instead, the super-resolution imaging is achieved by modulating the sub-frame images recorded by a two-dimensional (2D) camera in a digital fashion [65,66]. Such mechanism enables a compact and phase-artifact free strategy to achieve super-resolution imaging. Moreover, the direct-current component of the spatial frequency, predominately from the cornea reflection, is suppressed by the frequency shift which further makes VSD an desirable technique for *in vivo* retinal imaging. Recently, we demonstrated VSD-based SLO with a line-scanning modality for *in vivo* super-resolution imaging of animal retina and observed stimulus-evoked photoreceptor responses with subcellular-level spatial resolution and millisecond-level temporal resolution [3,126]. For human retinal imaging, the involuntary eye

movements, such as tremors and micro-saccades, can cause severe image distortions at low imaging speed [58,59]. A line-scanning imaging modality can dramatically improve the imaging speed and therefore reduce the artifacts caused by the eye movements. Moreover, the 2D sub-frame images recorded with temporal resolution at microsecond-level are essentially free from image distortions caused by the eye movements. Therefore, it further enables a registration of intra-frame distortions. In this letter, we report the experimental validation of VSD combined with the line-scanning SLO as a feasible method to achieve *in vivo* super-resolution imaging in human eye.

6.2 Methods

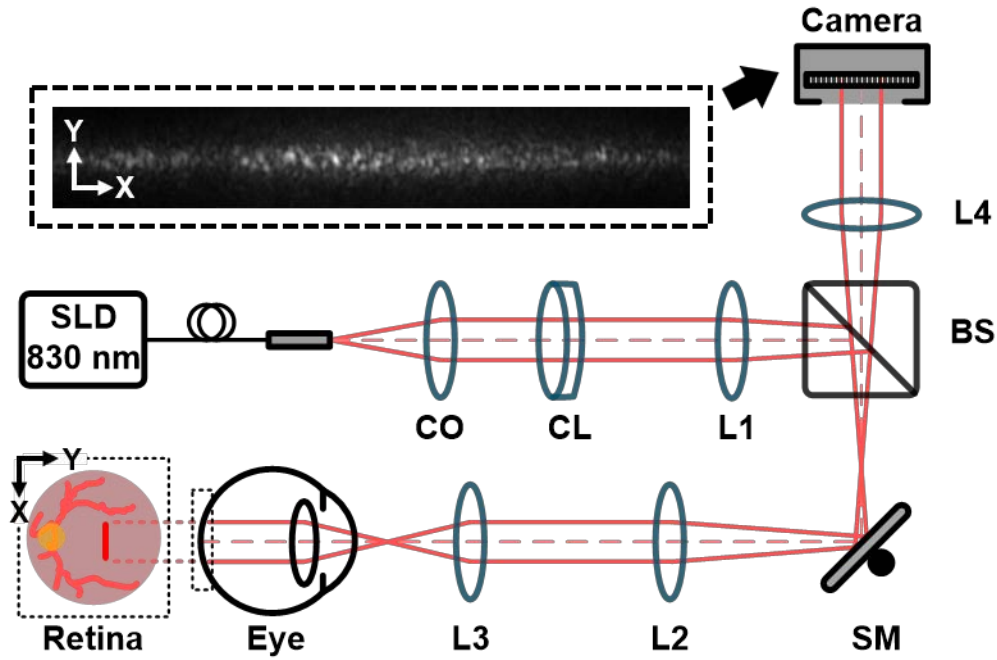


Fig. 6.1. Schematic diagram of the imaging system setup. SLD: superluminescent diode; CO: collimator; CL: cylindrical lens; L1–L4: lens; BS: beam splitter; SM: scanning mirror. A representative 2D sub-frame image is shown in the dash-rectangle at the top.

The schematic diagram of the VSD-based SLO system is shown in Figure 6.1. A near-infrared superluminescent diode (SLD-35-HP, Superlum) with a bandwidth of 60 nm and a central wavelength of 830 nm was used as the light source. The line illumination was

achieved by using a cylindrical lens. The galvo scanning mirror (GVS011, Thorlabs) was placed near the conjugate plane of pupil to minimize the vignetting effect. The reflected light from retina was descanned by the scanning mirror and relayed to the image plane of the retina on a 2D CMOS camera (FastCam Mini Ax50, Photron). In this system, as shown in Fig. 6.1, the camera was oriented in the X-direction and the scanning was performed along the Y-direction. Therefore, a resolution improvement would be expected in the Y-direction. The 2D sub-frame images were acquired at a speed of 25,000 frames/second (fps) to achieve a fast full-frame imaging speed of retina with a reasonable signal-to-noise ratio. The illumination light beam has a width of ~ 2.75 mm at the surface of cornea to achieve a best focus on the retina [139]. The illumination power at cornea was ~ 2.5 mW, which is below exposure safety limit required by the American National Standards Institute (ANSI). Human subject without any known ocular diseases was involved in the experiment with informed consent. During the imaging, the subject stayed in a room with minimized light level and the average pupil size was measured as ~ 5 mm. A dim red fixation target was used to reduce the eye motion.

6.3 Results

Figs. 6.2(a) and 6.2(b) are representative single-frame images reconstructed from a same dataset acquired at $\sim 4.2^\circ$ eccentricity, with a field of view (FOV) of $\sim 76 \times 436$ μm on retina and an imaging speed of 200 fps. As the human eye movements have a frequency as high as 100 Hz, the possible image distortions caused by eye movements was minimized at such imaging speed. Fig. 6.2(a) shows an equivalent wide-field (EWF) image obtained by sequentially superimposing raw sub-frame images along the scanning direction. Fig. 6.2(b) shows the corresponding super-resolution image reconstructed with

the VSD technique. As shown in Fig. 6.2(a), the photoreceptor mosaic cannot be well distinguished in the EWF image. In comparison, VSD image (Fig. 6.2(b)) exhibits a better image quality. To better illustrate the improvement, intensity profiles of the dashed lines in Figs. 6.2(c) and 6.2(d) and the spatial spectrum of Figs. 6.2(a) and 6.2(b) along non-scanning (f_x) and scanning (f_y) directions are shown in Figs. 6.2(e) - 2(h), respectively. In Fig. 6.2(e), the intensity profiles show that the photoreceptors cannot be well resolved at the non-scanning direction (X-direction) in both EWF and VSD images. However, in Fig. 6.2(f), the comparison between blue and red curves implies better resolution and contrast for VSD image than the EWF image in the scanning direction (Y-direction). The observations are further substantiated by the spatial spectral profiles shown in Figs. 6.2(g) and 6.2(h). In Fig. 6.2(g), the similarity between the spectral profiles of EWF and VSD images along f_x indicates a negligible improvement of the VSD image in the non-scanning direction. In Fig. 6.2(h), a local peak in the spectral profile of the VSD image along f_y can be observed at 0.12 cycles/ μm (Yellott's ring), which is in agree with the spatial frequency of the cone photoreceptor density at $\sim 4.6^\circ$ eccentricity [140-142]. However, the peak cannot be observed in the spectral profile of EWF image, indicating the photoreceptors cannot be well resolved in the EWF image. Additionally, the overall spectral amplitude and width were increased along f_y for the VSD image, which affirms that the VSD technique shifted sample spectrum into the passband of the optical imaging system. In consequence, the overall contrast of the VSD image (Fig. 6.2(b), 0.89) is better than that of the EWF image (Fig. 6.2(a), 0.33).

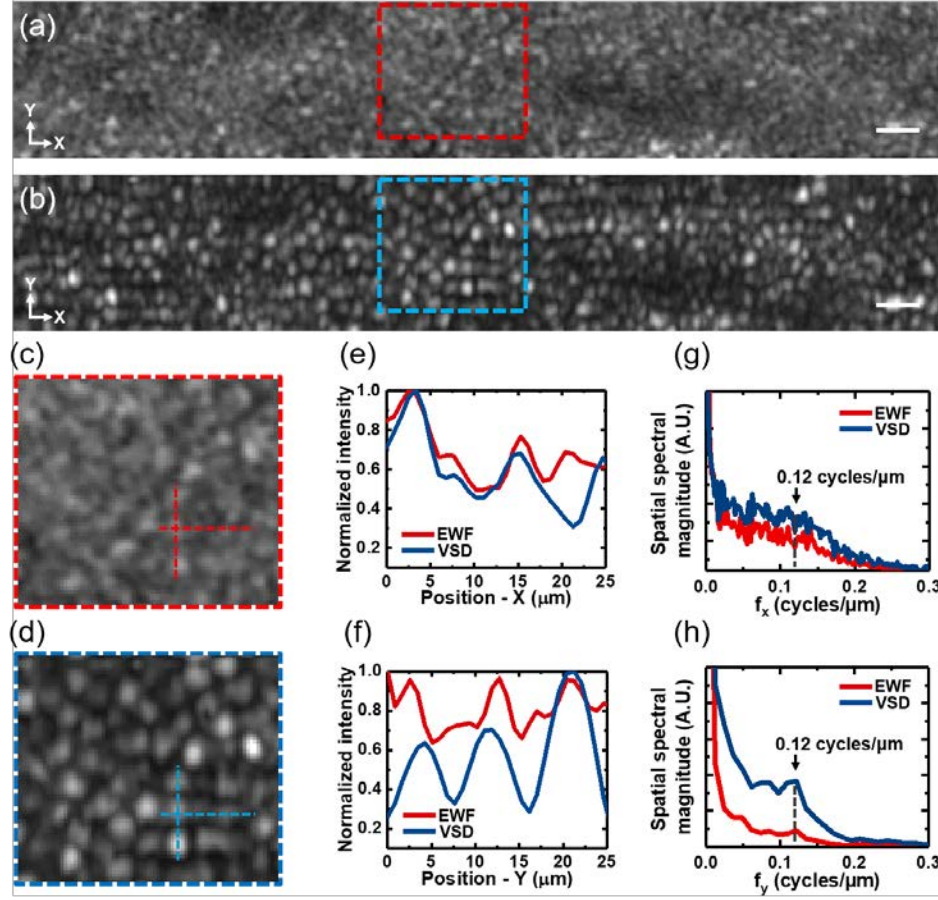


Fig. 6.2. Comparative *in vivo* imaging of human photoreceptors. Single-frame (a) EWF and (b) VSD image of human cone photoreceptor mosaic at $\sim 4.2^\circ$ eccentricity with a FOV of $\sim 76 \times 436 \mu\text{m}$ on retina. The scanning was in Y-direction. (c) Magnified view of the red-dashed rectangle in (a). (d) Magnified view of the blue-dashed rectangle in (b). (e) Reflective intensity profiles along the horizontal dashed lines in (c) and (d). (f) Reflective intensity profiles along the vertical dashed lines in (c) and (d). Spatial frequency profiles of (a) and (b) along (g) f_x direction and (h) f_y direction. f_x and f_y are the spatial frequency coordinates in non-scanning and scanning direction, respectively. Scale bars represent $\sim 20 \mu\text{m}$ on retina.

The eye movement-related image distortions become significant when a large FOV, corresponding to a lower imaging speed, is adopted. Fig. 6.3(a) shows a representative retinal image acquired at 40 fps with a FOV of $\sim 408 \times 436 \mu\text{m}$. Due to the eye movement, significant intra-frame distortions can be observed at the bottom of the image. For the VSD-based super-resolution imaging, a 2D sub-frame image is obtained at each scanning location. In this work, the sub-frame images were recorded at a rate (25 kHz) that is

multiple orders higher than the highest frequency of eye movements (~ 100 Hz). Thus, the sub-frame images were free from eye movement-related distortions. By sequentially comparing the adjacent sub-frame images, the retinal shift caused by the eye movements can be identified. The shift information further facilitated a registration between sub-frame images to compensate the retinal shift. Fig. 6.3(b) shows that a continuous retinal shift in the X-direction were detected in Fig. 6.3(a). With such shift information, the sub-frame images first underwent corresponding shifts in the opposite directions to compensate the retinal shift and were then used for VSD processing. Fig. 6.3(c) shows the reconstructed VSD image after the registration of intra-frame distortions. Enlarged comparison of the distorted area before and after intra-frame registration are shown in Figs. 6.3(d) and 6.3(e). The abnormal pattern of photoreceptors in Fig. 6.3(d) were corrected in Fig. 6.3(e).

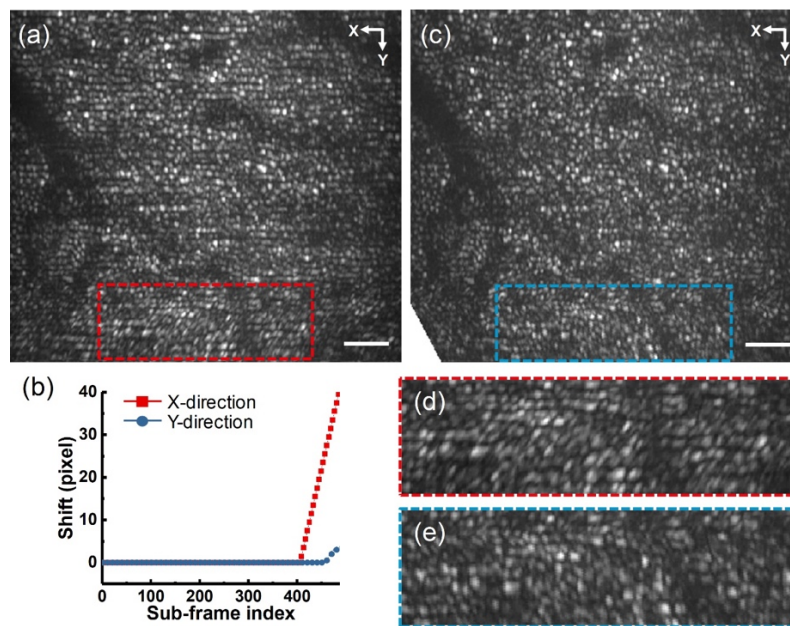


Fig. 6.3. (a) A representative VSD image with intra-frame distortions at the bottom of the image. Focus is at the photoreceptor layer. (b) The absolute retinal shift in each sub-frame image, with the first sub-frame image as a reference. (c) VSD image after the registration of intra-frame distortions. (d) Magnified view of the red-dashed rectangle in (a) to show the image distortions. (e) Magnified view of the blue-dashed rectangle in (b) to show the registration performance. Scanning direction was along Y-axis. Scale bars represent $\sim 50 \mu\text{m}$ on retina.

Single-frame photoreceptor images acquired at $\sim 4^\circ$, 3° , 2° , and 1° eccentricities from fovea are shown in Fig. 6.4. These representative images were determined with minimum intra-frame distortions by the pre-mentioned method. The comparison between EWF (Fig. 6.4(a)) and VSD (Fig. 6.4(b)) images shows that the VSD images have overall better image qualities than the EWF images at different retinal locations. Specifically, the values of image contrast for the EWF images are 0.34 (Fig. 6.4(a1)), 0.32 (Fig. 6.4(a2)), 0.28 (Fig. 6.4(a3)), and 0.29 (Fig. 6.4(a4)) respectively. In comparison, the VSD images present significantly improved contrasts of 0.91 (Fig. 6.4(b1)), 0.90 (Fig. 6.4(b2)), 0.86 (Fig. 6.4(b3)), and 0.85 (Fig. 6.4(b4)), respectively. The peak signal-to-noise ratio (SNR) in the EWF images are ~ 67.7 dB (Fig. 6.4(a1)), ~ 71.1 dB (Fig. 6.4(a2)), ~ 69.2 dB (Fig. 6.4(a3)), and ~ 43.2 dB (Fig. 6.4(a4)), respectively. While the peak SNR in the VSD images are ~ 94.4 dB (Fig. 6.4(b1)), ~ 92.8 dB (Fig. 6.4(b2)), ~ 91.6 dB (Fig. 6.4(b3)), and ~ 89.2 dB (Fig. 6.4(b4)), respectively [126]. The VSD images also present better SNR than the EWF images. Additionally, due to the improvement in VSD image quality, the projection of micro-capillary structures, which cannot be observed in the EWF images, are clearly revealed in the VSD images, as indicated by the yellow arrowheads in Fig. 6.4(b). Detailed photoreceptor structures in the white-dashed squares in Figs. 6.4(a) and 6.4(b) are shown in Figs. 6.4(c) and 6.4(d). The photoreceptors mosaics cannot be well resolved in the EWF images. But in VSD images, clear photoreceptor pattern can be resolved up to $\sim 1^\circ$ eccentricity temporal to fovea. Thanks to the improvement of image quality and resolution in the VSD images, cone photoreceptor densities can be measured at the corresponding locations in Fig. 6.4(b). The data shown in Fig. 6.4(e) present a general accordance with the cone densities in the literature [140,142].

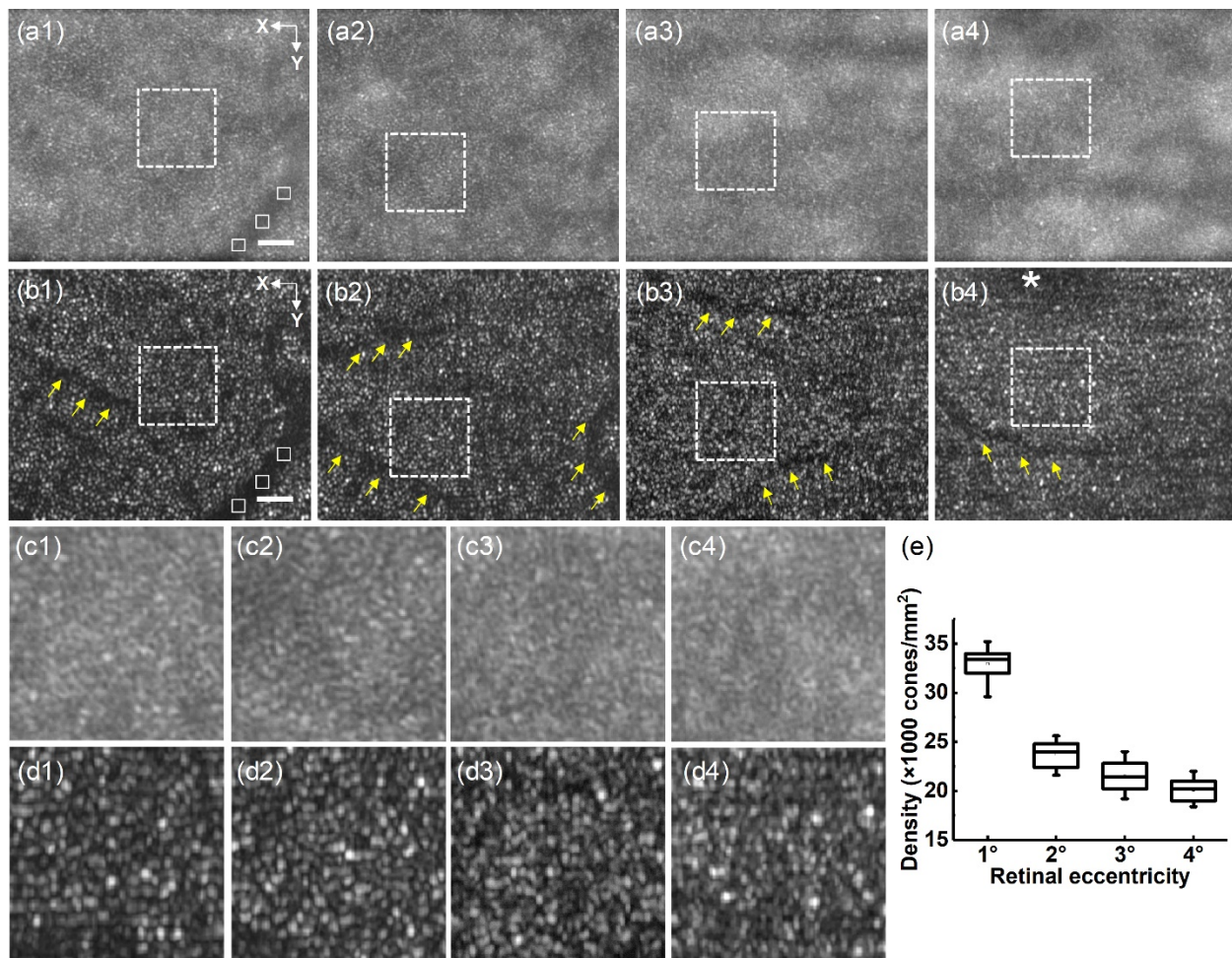


Fig. 6.4. Comparison of single-frame EWF and VSD images acquired at different retinal locations with focus at the photoreceptor layer. (a1 – a4) EWF images obtained from $\sim 4^\circ$, 3° , 2° , and 1° eccentricities temporal to fovea, respectively. (b1 – b4) VSD images corresponded to (a1 – a4), respectively. Yellow arrowheads indicate the projections of micro-capillary structure revealed by the VSD technique. The white asterisk in (b4) indicates fovea. The white-solid squares in (a1) and (b1) are used to estimate the noise level for calculating the peak SNRs. (c1 – c4) Magnified view of the areas indicated by the white-dashed squares in (a1 – a4), respectively. (d1 – d4) Magnified view of the areas indicated by the white-dashed squares in (b1 – b4), respectively. (e) Cone photoreceptor densities measured from VSD images recorded at different retinal eccentricities (temporal to fovea). Scale bars represent $\sim 50 \mu\text{m}$ on retina.

6.4 Discussion

In conclusion, we developed a VSD-based super-resolution SLO with a line-scanning modality for human retinal imaging. The VSD technique enabled a compact and cost-efficient setup for the imaging system. The digital implementation of intensity modulation

further enabled a phase-artifact free approach to achieve super-resolution imaging. The millisecond-level temporal resolution enabled by the line-scanning modality minimized the effect of the involuntary eye movements. Though the distortions caused by eye movements were inevitable when a large FOV was adopted, the intrinsic mechanism of VSD, i.e., recording with 2D sub-frame images, enabled an objective registration of the intra-frame distortions. As a result of these advantages offered by VSD technique and line-scanning modality, the VSD images exhibited significantly improved image quality, in the aspects of resolution, contrast and SNR, compared with that of the EWF images. Photoreceptor at different retinal locations were successfully resolved without using any AO. We aware that the resolution improvement of the current system setup is anisotropic due to the line-scanning modality. However, the results showed that a balance between imaging speed and image quality improvement was reasonably achieved. The results in Fig. 6.4 show that the resolution of the current system reaches its limit at $\sim 1^\circ$ eccentricity from fovea. Consequently, the cone photoreceptor densities measured at $\sim 1^\circ$ eccentricity ($\sim 34,000$ cones/mm²) are lower than the average data ($\sim 40,000$ cones/mm²) in the literature [140,142]. Such limitation can be attributed to the sensitivity and SNR of the CMOS camera. As a proof-of-concept study, the system was constructed with all commercially available components. Further optimization of the system, such as customized optical/system design, can further improve the super-resolution imaging performance and promise a convenient deployment for clinics.

Funding

National Institutes of Health (NIH) (R01 EY030101, R01 EY023522, P30 EY001792);
Unrestricted grant from Research to Prevent Blindness; Richard and Loan Hill
endowment.

CHAPTER VII. DISCUSSION AND CONCLUSION

In this dissertation, characteristics of photoreceptor-IOS were quantitatively investigated and an imaging platform for human retinal studies was developed. The research in this dissertation provide a better understanding of the basic principles of photoreceptor-IOS and promise a high spatiotemporal resolution method for functional mapping of photoreceptor physiology.

7.1 Physiological origin of photoreceptor-IOS

The physiological origin of TRP-associated photoreceptor-IOS was first investigated by using a low-sodium medium perfusion. The low-sodium medium perfusion abolishes the ERG responses but maintains the early phases of phototransduction cascades. Comparative studies showed that the ERG responses were successfully abolished by the low-sodium medium perfusion but the TRP responses were preserved. Further experiments showed that the TRP responses had an earlier onset time than the ERG a-wave. The results indicated that the TRP-associated photoreceptor-IOS has a physiological origin in the phototransduction cascades before the hyperpolarization of photoreceptor outer segment membrane, which include the sequential activation of rhodopsin, transducin and PDE, and the hydrolysis of cGMP.

The relationship between photoreceptor-IOS and PDE was further investigated by using a retinal degeneration mouse model (rd10) with a spontaneous PDE deficiency in Chapter III. Comparing the spatiotemporal characteristics of photoreceptor-IOS responses in WT and rd10, we found that the deficiency of PDE did not affect the photoreceptor-IOS in rd10 mouse at the age of P14. Our previous studies of photoreceptor-IOS with high temporal resolution showed that the onset of photoreceptor-

IOS is less than 4 ms. Considering the phototransduction is a cascaded reaction, our experimental results further suggest that the physiological origin of photoreceptor-IOS is earlier than the activation of PDE. The possibilities include stimulus-evoked activities of rhodopsin, transducin, and/or the distribution of the phospholipids in the disc membranes. Further studies that involve rhodopsin- and/or transducin-correlated mutant mouse model are desirable to specify the physiological origin of photoreceptor-IOS.

7.2 Physical origin of photoreceptor-IOS

In the studies described in Chapter IV, light and electron microscopic studies were conducted to investigate the physical properties of the light-induced photoreceptor outer segment changes. It is interesting to see that the visible light stimulation elicited a length shrinkage but did not change the diameter of the rod outer segments. The observation demonstrated that the outer segment itself can trigger the structural change, indicating physical origin of the light-induced outer segment changes was within the outer segment. Further histological studies substantiated the observation by showing that the inner segments did not exhibit significant light-induced structural changes.

There are many previous studies demonstrated light-induced structural changes of photoreceptors with different imaging modalities and experimental protocols [75,82,84,87]. However, they did not provide a direct view of the structural change. TEM can provide a direct observation of the intracellular structures at a nanometer-level resolution and thus facilitate a direct observation and comparison of the lamellar structure of the outer segment discs. Our statistical analysis of the TEM images shows that a light-induced decrease of the inter-disc space, not the disc thickness, was correlated with the overall shrinkage of the outer segments. Though the mechanism behind the inter-disc

space shrinkage is still unknown, this study provides a better understanding about the phototransduction and the structural principle of the light-induced outer segment changes.

7.3 *In vivo* demonstration of TRP

In our previous studies, *in vitro* TRP has been observed in frog and mouse retina. However, *in vivo* observation of TRP is important to substantiate its capability as a biomarker for reflecting retinal functionality. In Chapter V, we demonstrate *in vivo* TRP for the first time in a living animal eye. As our *in vitro* studies show that TRP has a relatively low magnitude and a fast response time course, the VSD-based super-resolution technique and a line-scan SLO were applied to image the *in vivo* TRP. Our analysis showed that the spatiotemporal characteristics of *in vivo* TRP were basically consistent with that of *in vitro* TRP. The successful demonstration of *in vivo* TRP in animal model promises a biomarker for the objective assessment of photoreceptor functionality in human eye. Therefore, an imager that can provide human retinal images with high spatiotemporal resolution is needed.

7.4 *In vivo* super-resolution imaging of human retina

The *in vivo* imaging of human retinal structures with a high resolution is challenging. The aberration, low NA and rapid involuntary movement of human eye can significantly reduce the image quality. For a long time, AO techniques are employed to compensate the aberration of human eye and have successfully demonstrated retinal structures, such as photoreceptors and ganglion cells. However, AO systems are usually physical large, complex, expensive and difficult to handle. Therefore, the clinic deployment of AO technique is still not available. In Chapter VI, a VSD-based super-resolution SLO with a line-scan imaging modality was designed and developed for human retinal imaging.

Due to the digital implementation of super-resolution, the system is much compact and easy to operate. We successfully demonstrated unambiguous identifications of photoreceptor mosaics at different locations of retina. By using the line-scan technique, the imaging speed can achieve more than 200 frames/s with a desirable FOV. With these advantages, the imaging system developed in this research promises an effective platform to investigate the photoreceptor-IOS in human retina.

In conclusion, this dissertation study enhanced our understanding of photoreceptor-IOS regarding its physiological and anatomical properties. *In vivo* observation of TRP in animal model was demonstrated for the first time. The feasibility of using VSD-based super-resolution technique to image photoreceptor mosaic in human eye was also demonstrated. Further animal and human studies are necessary to reveal the physiological and physical mechanisms of photoreceptor-IOS and how they are correlated with different retinal diseases. With the theoretical and instrumental development, photoreceptor-IOS imaging can enable a parallel monitoring of morphology and functionality of the retina with high resolution and promises an effective biomarker for the early diagnosis and treatment assessment of retinal diseases.

CITED LITERATURE

1. Y. Lu, B. Wang, D. R. Pepperberg, and X. Yao, "Stimulus-evoked outer segment changes occur before the hyperpolarization of retinal photoreceptors," *Biomedical optics express* **8**, 38-47 (2017).
2. Y. Lu, J. Benedetti, and X. Yao, "Light-Induced Length Shrinkage of Rod Photoreceptor Outer Segments," *Transl Vis Sci Technol* **7**, 29 (2018).
3. Y. Lu, C. Liu, and X. Yao, "In vivo super-resolution imaging of transient retinal phototropism evoked by oblique light stimulation," *Journal of biomedical optics* **23**, 050502 (2018).
4. D. S. Friedman, B. J. O'Colmain, B. Munoz, S. C. Tomany, C. McCarty, P. T. de Jong, B. Nemesure, P. Mitchell, J. Kempen, and G. Eye Diseases Prevalence Research, "Prevalence of age-related macular degeneration in the United States," *Arch Ophthalmol* **122**, 564-572 (2004).
5. G. R. Jackson, C. Owsley, and C. A. Curcio, "Photoreceptor degeneration and dysfunction in aging and age-related maculopathy," *Ageing research reviews* **1**, 381-396 (2002).
6. R. D. Jager, W. F. Mieler, and J. W. Miller, "Age-related macular degeneration," *New England Journal of Medicine* **358**, 2606-2617 (2008).
7. P. N. Dimitrov, L. D. Robman, M. Varsamidis, K. Z. Aung, G. A. Makeyeva, R. H. Guymer, and A. J. Vingrys, "Visual function tests as potential biomarkers in age-related macular degeneration," *Investigative ophthalmology & visual science* **52**, 9457-9469 (2011).
8. J. S. Sunness, R. W. Massof, M. A. Johnson, N. M. Bressler, S. B. Bressler, and S. L. Fine, "Diminished foveal sensitivity may predict the development of advanced age-related macular degeneration," *Ophthalmology* **96**, 375-381 (1989).
9. C. A. Curcio, N. E. Medeiros, and C. L. Millican, "Photoreceptor loss in age-related macular degeneration," *Investigative ophthalmology & visual science* **37**, 1236-1249 (1996).
10. D. C. Hood, K. Holopigian, V. Greenstein, W. Seiple, J. Li, E. E. Sutter, and R. E. Carr, "Assessment of local retinal function in patients with retinitis pigmentosa using the multi-focal ERG technique," *Vision Res* **38**, 163-179 (1998).
11. Vaegan, F. Billson, S. Kemp, M. Morgan, M. Donnelley, and P. Montgomery, "Macular Electroretinograms - Their Accuracy, Specificity and Implementation for Clinical Use," *Aust J Ophthalmol* **12**, 359-372 (1984).
12. X. Yao, T. Son, T.-H. Kim, and Y. Lu, "Functional optical coherence tomography of retinal photoreceptors," *Experimental Biology and Medicine* **243**, 1256-1264 (2018).
13. X. Yao and B. Wang, "Intrinsic optical signal imaging of retinal physiology: a review," *Journal of biomedical optics* **20**, 090901 (2015).
14. A. Swaroop, D. Kim, and D. Forrest, "Transcriptional regulation of photoreceptor development and homeostasis in the mammalian retina," *Nat Rev Neurosci* **11**, 563-576 (2010).
15. H. Kolb, "Gross anatomy of the eye" (January 25, 2012, 2012), retrieved <https://webvision.med.utah.edu/book/part-i-foundations/gross-anatomy-of-the-eye/>.

16. H. Kolb, "How the retina works: Much of the construction of an image takes place in the retina itself through the use of specialized neural circuits," *American scientist* **91**, 28-35 (2003).
17. H. Kolb, "Photoreceptors" (2013), retrieved <https://webvision.med.utah.edu/book/part-ii-anatomy-and-physiology-of-the-retina/photoreceptors/>.
18. G. Wald, P. K. Brown, and I. R. Gibbons, "The problem of visual excitation," *J Opt Soc Am* **53**, 20-35 (1963).
19. R. H. Steinberg, S. K. Fisher, and D. H. Anderson, "Disc morphogenesis in vertebrate photoreceptors," *J Comp Neurol* **190**, 501-508 (1980).
20. D. Mustafi, A. H. Engel, and K. Palczewski, "Structure of cone photoreceptors," *Prog Retin Eye Res* **28**, 289-302 (2009).
21. Y. Fu and K. W. Yau, "Phototransduction in mouse rods and cones," *Pflugers Arch* **454**, 805-819 (2007).
22. T. D. Lamb and E. N. Pugh, Jr., "Phototransduction, dark adaptation, and rhodopsin regeneration the proctor lecture," *Invest Ophthalmol Vis Sci* **47**, 5137-5152 (2006).
23. E. N. Pugh Jr and T. D. Lamb, "Phototransduction in vertebrate rods and cones: molecular mechanisms of amplification, recovery and light adaptation," in *Handbook of biological physics* (Elsevier, 2000), pp. 183-255.
24. V. Y. Arshavsky, T. D. Lamb, and E. N. Pugh Jr, "G proteins and phototransduction," *Annual review of physiology* **64**, 153-187 (2002).
25. J. Corneveaux, "Representation of molecular steps in photoactivation" (2007), retrieved <https://commons.wikimedia.org/wiki/File:Phototransduction.png>.
26. I. Perlman, "The electroretinogram: ERG" (2019), retrieved <https://webvision.med.utah.edu/book/electrophysiology/the-electroretinogram-erg/>.
27. M. M. Moschos and E. Nitoda, "The Role of mf-ERG in the Diagnosis and Treatment of Age-Related Macular Degeneration: Electrophysiological Features of AMD," *Semin Ophthalmol* **33**, 461-469 (2018).
28. M. Seeliger, U. Kretschmann, E. Apfelstedt-Sylla, K. Ruther, and E. Zrenner, "Multifocal electroretinography in retinitis pigmentosa," *Am J Ophthalmol* **125**, 214-226 (1998).
29. P. Lachapelle, J. M. Little, and R. C. Polomeno, "The photopic electroretinogram in congenital stationary night blindness with myopia," *Invest Ophthalmol Vis Sci* **24**, 442-450 (1983).
30. D. R. Pepperberg, P. K. Brown, M. Lurie, and J. E. Dowling, "Visual pigment and photoreceptor sensitivity in the isolated skate retina," *J Gen Physiol* **71**, 369-396 (1978).
31. R. D. Penn and W. A. Hagins, "Signal transmission along retinal rods and the origin of the electroretinographic a-wave," *Nature* **223**, 201-204 (1969).
32. A. J. Sillman, H. Ito, and T. Tomita, "Studies on the mass receptor potential of the isolated frog retina. II. On the basis of the ionic mechanism," *Vision Res* **9**, 1443-1451 (1969).

33. R. F. Miller and J. E. Dowling, "Intracellular responses of the Muller (glial) cells of mudpuppy retina: their relation to b-wave of the electroretinogram," *J Neurophysiol* **33**, 323-341 (1970).
34. E. A. Newman, "Current source-density analysis of the b-wave of frog retina," *J Neurophysiol* **43**, 1355-1366 (1980).
35. B. Oakley, 2nd and D. G. Green, "Correlation of light-induced changes in retinal extracellular potassium concentration with c-wave of the electroretinogram," *J Neurophysiol* **39**, 1117-1133 (1976).
36. D. C. Hood, J. G. Odel, C. S. Chen, and B. J. Winn, "The multifocal electroretinogram," *J Neuroophthalmol* **23**, 225-235 (2003).
37. Y. C. Li, W. X. Cui, X. J. Wang, F. Amthor, R. W. Lu, A. Thompson, and X. C. Yao, "Intrinsic optical signal imaging of glucose-stimulated insulin secreting beta-cells," *Opt Express* **19**, 99-106 (2011).
38. X. C. Yao, W. X. Cui, Y. C. Li, W. Zhang, R. W. Lu, A. Thompson, F. Amthor, and X. J. Wang, "Functional imaging of glucose-evoked rat islet activities using transient intrinsic optical signals," *J Mod Opt* **59**(2012).
39. B. Chance, Q. Luo, S. Nioka, D. C. Alsop, and J. A. Detre, "Optical investigations of physiology: a study of intrinsic and extrinsic biomedical contrast," *Philos Trans R Soc Lond B Biol Sci* **352**, 707-716 (1997).
40. A. Grinvald, E. Lieke, R. D. Frostig, C. D. Gilbert, and T. N. Wiesel, "Functional architecture of cortex revealed by optical imaging of intrinsic signals," *Nature* **324**, 361-364 (1986).
41. L. B. Cohen, R. D. Keynes, and B. Hille, "Light scattering and birefringence changes during nerve activity," *Nature* **218**, 438-441 (1968).
42. R. W. Lu, Q. X. Zhang, and X. C. Yao, "Circular polarization intrinsic optical signal recording of stimulus-evoked neural activity," *Opt Lett* **36**, 1866-1868 (2011).
43. X. C. Yao, A. Foust, D. M. Rector, B. Barrowes, and J. S. George, "Cross-polarized reflected light measurement of fast optical responses associated with neural activation," *Biophys J* **88**, 4170-4177 (2005).
44. K. Bizheva, R. Pflug, B. Hermann, B. Povazay, H. Sattmann, P. Qiu, E. Anger, H. Reitsamer, S. Popov, J. R. Taylor, A. Unterhuber, P. Ahnelt, and W. Drexler, "Optophysiology: depth-resolved probing of retinal physiology with functional ultrahigh-resolution optical coherence tomography," *Proc Natl Acad Sci U S A* **103**, 5066-5071 (2006).
45. D. Ts'o, J. Schallek, Y. Kwon, R. Kardon, M. Abramoff, and P. Soliz, "Noninvasive functional imaging of the retina reveals outer retinal and hemodynamic intrinsic optical signal origins," *Jpn J Ophthalmol* **53**, 334-344 (2009).
46. B. Wang, Y. Lu, and X. Yao, "In vivo optical coherence tomography of stimulus-evoked intrinsic optical signals in mouse retinas," *Journal of biomedical optics* **21**, 096010-096010 (2016).
47. Q. X. Zhang, R. W. Lu, Y. G. Li, and X. C. Yao, "In vivo confocal imaging of fast intrinsic optical signals correlated with frog retinal activation," *Opt Lett* **36**, 4692-4694 (2011).
48. X. C. Yao and Y. C. Li, "Functional imaging of retinal photoreceptors and inner neurons using stimulus-evoked intrinsic optical signals," *Methods Mol Biol* **884**, 277-285 (2012).

49. R. F. Cooper, W. S. Tuten, A. Dubra, D. H. Brainard, and J. I. W. Morgan, "Non-invasive assessment of human cone photoreceptor function," *Biomed Opt Express* **8**, 5098-5112 (2017).
50. D. Hillmann, H. Spahr, C. Pfaffle, H. Sudkamp, G. Franke, and G. Huttmann, "In vivo optical imaging of physiological responses to photostimulation in human photoreceptors," *Proc Natl Acad Sci U S A* **113**, 13138-13143 (2016).
51. F. Zhang, K. Kurokawa, A. Lassoued, J. A. Crowell, and D. T. Miller, "Cone photoreceptor classification in the living human eye from photostimulation-induced phase dynamics," *Proc Natl Acad Sci U S A* **116**, 7951-7956 (2019).
52. Q. X. Zhang, R. W. Lu, C. A. Curcio, and X. C. Yao, "In vivo confocal intrinsic optical signal identification of localized retinal dysfunction," *Invest Ophthalmol Vis Sci* **53**, 8139-8145 (2012).
53. D. Sun, S. Roth, and M. J. Black, "Secrets of optical flow estimation and their principles," in *Computer Vision and Pattern Recognition (CVPR), 2010 IEEE Conference on*, (IEEE, 2010), 2432-2439.
54. R. Lu, A. M. Levy, Q. Zhang, S. J. Pittler, and X. Yao, "Dynamic near-infrared imaging reveals transient phototropic change in retinal rod photoreceptors," *J Biomed Opt* **18**, 106013 (2013).
55. X. Zhao, D. Thapa, B. Wang, Y. Lu, S. Gai, and X. Yao, "Stimulus-evoked outer segment changes in rod photoreceptors," *Journal of biomedical optics* **21**, 065006-065006 (2016).
56. B. Wang, Q. Zhang, R. Lu, Y. Zhi, and X. Yao, "Functional optical coherence tomography reveals transient phototropic change of photoreceptor outer segments," *Opt Lett* **39**, 6923-6926 (2014).
57. R. H. Webb and G. W. Hughes, "Scanning laser ophthalmoscope," *IEEE Trans Biomed Eng* **28**, 488-492 (1981).
58. R. Ditchburn and B. Ginsborg, "Involuntary eye movements during fixation," *The Journal of physiology* **119**, 1-17 (1953).
59. M. Ezenman, P. Hallett, and R. Frecker, "Power spectra for ocular drift and tremor," *Vision research* **25**, 1635-1640 (1985).
60. P. Bedggood and A. Metha, "De-warping of images and improved eye tracking for the scanning laser ophthalmoscope," *PloS one* **12**, e0174617 (2017).
61. C. R. Vogel, D. W. Arathorn, A. Roorda, and A. Parker, "Retinal motion estimation in adaptive optics scanning laser ophthalmoscopy," *Optics express* **14**, 487-497 (2006).
62. A. Uji, S. Ooto, M. Hangai, S. Arichika, and N. Yoshimura, "Image quality improvement in adaptive optics scanning laser ophthalmoscopy assisted capillary visualization using B-spline-based elastic image registration," *PLoS One* **8**, e80106 (2013).
63. M. G. Gustafsson, "Surpassing the lateral resolution limit by a factor of two using structured illumination microscopy," *Journal of microscopy* **198**, 82-87 (2000).
64. M. G. Gustafsson, L. Shao, P. M. Carlton, C. R. Wang, I. N. Golubovskaya, W. Z. Cande, D. A. Agard, and J. W. Sedat, "Three-dimensional resolution doubling in wide-field fluorescence microscopy by structured illumination," *Biophysical journal* **94**, 4957-4970 (2008).

65. J. Lu, W. Min, J.-A. Conchello, X. S. Xie, and J. W. Lichtman, "Super-resolution laser scanning microscopy through spatiotemporal modulation," *Nano letters* **9**, 3883-3889 (2009).
66. R.-W. Lu, B.-Q. Wang, Q.-X. Zhang, and X.-C. Yao, "Super-resolution scanning laser microscopy through virtually structured detection," *Biomedical optics express* **4**, 1673-1682 (2013).
67. W. Stiles and B. Crawford, "The luminous efficiency of rays entering the eye pupil at different points," *Proceedings of the Royal Society of London. Series B, Containing Papers of a Biological Character* **112**, 428-450 (1933).
68. K. P. Hofmann, R. Uhl, W. Hoffmann, and W. Kreutz, "Measurements on fast light-induced light-scattering and -absorption changes in outer segments of vertebrate light sensitive rod cells," *Biophys Struct Mech* **2**, 61-77 (1976).
69. H. Kühn, N. Bennett, M. Michel-Villaz, and M. Chabre, "Interactions between photoexcited rhodopsin and GTP-binding protein: kinetic and stoichiometric analyses from light-scattering changes," *Proceedings of the National Academy of Sciences* **78**, 6873-6877 (1981).
70. D. R. Pepperberg, M. Kahlert, A. Krause, and K. P. Hofmann, "Photic modulation of a highly sensitive, near-infrared light-scattering signal recorded from intact retinal photoreceptors," *Proc Natl Acad Sci U S A* **85**, 5531-5535 (1988).
71. M. Kahlert, D. R. Pepperberg, and K. P. Hofmann, "Effect of bleached rhodopsin on signal amplification in rod visual receptors," *Nature* **345**, 537-539 (1990).
72. K. P. Hofmann, A. Schleicher, D. Emeis, and J. Reichert, "Light-induced axial and radial shrinkage effects and changes of the refractive index in isolated bovine rod outer segments and disc vesicles: physical analysis of near-infrared scattering changes," *Biophys Struct Mech* **8**, 67-93 (1981).
73. Q. Zhang, R. Lu, B. Wang, J. D. Messinger, C. A. Curcio, and X. Yao, "Functional optical coherence tomography enables in vivo physiological assessment of retinal rod and cone photoreceptors," *Sci Rep* **5**, 9595 (2015).
74. X. Yao and B. Wang, "Intrinsic optical signal imaging of retinal physiology: a review," *J Biomed Opt* **20**, 090901 (2015).
75. J. E. Brown and L. H. Pinto, "Ionic mechanism for the photoreceptor potential of the retina of *Bufo marinus*," *J Physiol* **236**, 575-591 (1974).
76. M. E. Burns and D. A. Baylor, "Activation, deactivation, and adaptation in vertebrate photoreceptor cells," *Annu Rev Neurosci* **24**, 779-805 (2001).
77. X. C. Yao and Y. B. Zhao, "Optical dissection of stimulus-evoked retinal activation," *Opt Express* **16**, 12446-12459 (2008).
78. H. P. Scholl and E. Zrenner, "Electrophysiology in the investigation of acquired retinal disorders," *Surv Ophthalmol* **45**, 29-47 (2000).
79. N. Otsu, "Threshold Selection Method from Gray-Level Histograms," *Ieee T Syst Man Cyb* **9**, 62-66 (1979).
80. Y. G. Li, L. Liu, F. Amthor, and X. C. Yao, "High-speed line-scan confocal imaging of stimulus-evoked intrinsic optical signals in the retina," *Opt Lett* **35**, 426-428 (2010).
81. Q. X. Zhang, J. Y. Wang, L. Liu, and X. C. Yao, "Microlens array recording of localized retinal responses," *Opt Lett* **35**, 3838-3840 (2010).

82. J. Heller, T. J. Ostwald, and D. Bok, "The osmotic behavior of rod photoreceptor outer segment discs," *J Cell Biol* **48**, 633-649 (1971).
83. N. Yagi, "Structural changes in rod outer segments of frog and mouse after illumination," *Exp Eye Res* **116**, 395-401 (2013).
84. J. Heller, T. J. Ostwald, and D. Bok, "Effect of illumination on the membrane permeability of rod photoreceptor discs," *Biochemistry* **9**, 4884-4889 (1970).
85. D. C. Mitchell and B. J. Litman, "Effect of ethanol and osmotic stress on receptor conformation. Reduced water activity amplifies the effect of ethanol on metarhodopsin II formation," *J Biol Chem* **275**, 5355-5360 (2000).
86. T. M. Vuong, C. Pfister, D. L. Worcester, and M. Chabre, "The transducin cascade is involved in the light-induced structural changes observed by neutron diffraction on retinal rod outer segments," *Biophys J* **52**, 587-594 (1987).
87. H. Asai, T. Chiba, S. Kimura, and M. Takagi, "A light-induced conformational change in rod photoreceptor disc membrane," *Exp Eye Res* **21**, 259-267 (1975).
88. E. Hessel, A. Herrmann, P. Muller, P. P. Schnetkamp, and K. P. Hofmann, "The transbilayer distribution of phospholipids in disc membranes is a dynamic equilibrium evidence for rapid flip and flop movement," *Eur J Biochem* **267**, 1473-1483 (2000).
89. Y. Zhi, R. Lu, B. Wang, Q. Zhang, and X. Yao, "Rapid super-resolution line-scanning microscopy through virtually structured detection," *Optics letters* **40**, 1683-1686 (2015).
90. Y. Zhi, B. Wang, and X. Yao, "Super-resolution scanning laser microscopy based on virtually structured detection," *Critical Reviews™ in Biomedical Engineering* **43**(2015).
91. B. Wang, R. Lu, Q. Zhang, and X. Yao, "Breaking diffraction limit of lateral resolution in optical coherence tomography," *Quant Imaging Med Surg* **3**, 243-248 (2013).
92. D. Nagy, B. Schönfish, E. Zrenner, and H. Jägle, "Long-term follow-up of retinitis pigmentosa patients with multifocal electroretinography," *Investigative ophthalmology & visual science* **49**, 4664-4671 (2008).
93. Y. Qin, G. Xu, and W. Wang, "Dendritic abnormalities in retinal ganglion cells of three-month diabetic rats," *Current eye research* **31**, 967-974 (2006).
94. J. Schallek, H. Li, R. Kardon, Y. Kwon, M. Abramoff, P. Soliz, and D. Ts'o, "Stimulus-evoked intrinsic optical signals in the retina: spatial and temporal characteristics," *Investigative ophthalmology & visual science* **50**, 4865-4872 (2009).
95. V. Srinivasan, M. Wojtkowski, J. Fujimoto, and J. Duker, "In vivo measurement of retinal physiology with high-speed ultrahigh-resolution optical coherence tomography," *Optics letters* **31**, 2308-2310 (2006).
96. B. Chang, N. Hawes, M. Pardue, A. German, R. Hurd, M. Davisson, S. Nusinowitz, K. Rengarajan, A. Boyd, and S. Sidney, "Two mouse retinal degenerations caused by missense mutations in the β -subunit of rod cGMP phosphodiesterase gene," *Vision research* **47**, 624-633 (2007).
97. M. Samardzija, H. Wariwoda, C. Imsand, P. Huber, S. R. Heynen, A. Gubler, and C. Grimm, "Activation of survival pathways in the degenerating retina of rd10 mice," *Experimental eye research* **99**, 17-26 (2012).

98. R. Barhoum, G. Martinez-Navarrete, S. Corrochano, F. Germain, L. Fernandez-Sanchez, E. J. De la Rosa, P. de La Villa, and N. Cuenca, "Functional and structural modifications during retinal degeneration in the rd10 mouse," *Neuroscience* **155**, 698-713 (2008).
99. C. Gargini, E. Terzibasi, F. Mazzoni, and E. Strettoi, "Retinal organization in the retinal degeneration 10 (rd10) mutant mouse: a morphological and ERG study," *Journal of Comparative Neurology* **500**, 222-238 (2007).
100. M. E. Pennesi, K. V. Michaels, S. S. Magee, A. Maricle, S. P. Davin, A. K. Garg, M. J. Gale, D. C. Tu, Y. Wen, and L. R. Erker, "Long-term characterization of retinal degeneration in rd1 and rd10 mice using spectral domain optical coherence tomography," *Investigative ophthalmology & visual science* **53**, 4644-4656 (2012).
101. Q.-X. Zhang, Y. Zhang, R.-W. Lu, Y.-C. Li, S. J. Pittler, T. W. Kraft, and X.-C. Yao, "Comparative intrinsic optical signal imaging of wild-type and mutant mouse retinas," *Optics express* **20**, 7646-7654 (2012).
102. A. B. Fulton, R. M. Hansen, and O. Findl, "The development of the rod photoresponse from dark-adapted rats," *Investigative ophthalmology & visual science* **36**, 1038-1045 (1995).
103. C. Portera-Cailliau, C. Sung, J. Nathans, and R. Adler, "Apoptotic photoreceptor cell death in mouse models of retinitis pigmentosa," *Proceedings of the National Academy of Sciences* **91**, 974-978 (1994).
104. M. D. Abramoff, R. F. Mullins, K. Lee, J. M. Hoffmann, M. Sonka, D. B. Critser, S. F. Stasheff, and E. M. Stone, "Human photoreceptor outer segments shorten during light adaptation," *Invest Ophthalmol Vis Sci* **54**, 3721-3728 (2013).
105. S. E. G. Nilsson, "An electron microscopic classification of the retinal receptors of the leopard frog (*Rana pipiens*)," *Journal of ultrastructure research* **10**, 390-416 (1964).
106. L. D. Carter-Dawson and M. M. Lavail, "Rods and cones in the mouse retina. I. Structural analysis using light and electron microscopy," *Journal of Comparative Neurology* **188**, 245-262 (1979).
107. N. P. Boyer, C. Chen, and Y. Koutalos, "Preparation of living isolated vertebrate photoreceptor cells for fluorescence imaging," *Journal of visualized experiments: JoVE* (2011).
108. C. Chen, Y. Jiang, and Y. Koutalos, "Dynamic behavior of rod photoreceptor disks," *Biophysical journal* **83**, 1403-1412 (2002).
109. B. M. Tam, L. L. Yang, T. H. Bogéa, B. Ross, G. Martens, and O. L. Moritz, "Preparation of *Xenopus laevis* retinal cryosections for electron microscopy," *Experimental eye research* **136**, 86-90 (2015).
110. Q.-X. Zhang, R.-W. Lu, J. D. Messinger, C. A. Curcio, V. Guarcello, and X.-C. Yao, "In vivo optical coherence tomography of light-driven melanosome translocation in retinal pigment epithelium," *Scientific reports* **3**(2013).
111. J. USUKURA and E. YAMADA, "Molecular organization of the rod outer segment. A deep-etching study with rapid freezing using unfixed frog retina," *Biomedical Research* **2**, 177-193 (1981).
112. S. E. G. Nilsson, "The ultrastructure of the receptor outer segments in the retina of the leopard frog (*Rana pipiens*)," *Journal of ultrastructure research* **12**, 207-231 (1965).

113. K. Bachhuber and D. Frösch, "Electron microscopy of melamine-embedded frog retina: evidence for the overall crystalline organization of photoreceptor outer segments," *Journal of Microscopy* **133**, 103-109 (1984).
114. S. J. Fliesler, M. E. Rayborn, and J. G. Hollyfield, "Membrane morphogenesis in retinal rod outer segments: inhibition by tunicamycin," *The Journal of cell biology* **100**, 574-587 (1985).
115. J. L. Brubacher, A. P. Vieira, and P. A. Newmark, "Preparation of the planarian *Schmidtea mediterranea* for high-resolution histology and transmission electron microscopy," *Nature protocols* **9**, 661 (2014).
116. G. Jones, "Electron microscopy of frog photoreceptor outer segments after fixation with aldehydes," *Journal of cell science* **16**, 199-219 (1974).
117. P. D. Calvert, K. J. Strissel, W. E. Schiesser, E. N. Pugh Jr, and V. Y. Arshavsky, "Light-driven translocation of signaling proteins in vertebrate photoreceptors," *Trends in cell biology* **16**, 560-568 (2006).
118. O. Strauss, "The retinal pigment epithelium in visual function," *Physiological reviews* **85**, 845-881 (2005).
119. J. I. Korenbrot, D. T. Brown, and R. A. Cone, "Membrane characteristics and osmotic behavior of isolated rod outer segments," *The Journal of Cell Biology* **56**, 389-398 (1973).
120. I. Nir and D. C. Pease, "Ultrastructural aspects of discs in rod outer segments," *Experimental eye research* **16**, 173-182 (1973).
121. W. Hagins, R. Penn, and S. Yoshikami, "Dark current and photocurrent in retinal rods," *Biophysical journal* **10**, 380-412 (1970).
122. F. Billson, S. Kemp, M. Morgan, and P. MONTGOMERY, "Macular electroretinograms: their accuracy, specificity and implementation for clinical use," *Clinical & Experimental Ophthalmology* **12**, 359-372 (1984).
123. J. Li, M. O. Tso, and T. T. Lam, "Reduced amplitude and delayed latency in foveal response of multifocal electroretinogram in early age related macular degeneration," *British journal of ophthalmology* **85**, 287-290 (2001).
124. C. Owsley, C. Huisinigh, M. E. Clark, G. R. Jackson, and G. McGwin Jr, "Comparison of visual function in older eyes in the earliest stages of age-related macular degeneration to those in normal macular health," *Current eye research* **41**, 266-272 (2016).
125. J. Siderov and A. L. Tiu, "Variability of measurements of visual acuity in a large eye clinic," *Acta Ophthalmologica* **77**, 673-676 (1999).
126. C. Liu, Y. Zhi, B. Wang, D. Thapa, Y. Chen, M. Alam, Y. Lu, and X. Yao, "In vivo super-resolution retinal imaging through virtually structured detection," *Journal of biomedical optics* **21**, 120502-120502 (2016).
127. Y. Lu, C. Liu, and X. Yao, "In vivo observation of transient photoreceptor movement correlated with oblique light stimulation," *Proc SPIE Int Soc Opt Eng* **10497**(2018).
128. I. Commission, "Safety of laser products–Part 1: Equipment classification and requirements," (IEC, 2014).
129. F. C. Delori, R. H. Webb, and D. H. Sliney, "Maximum permissible exposures for ocular safety (ANSI 2000), with emphasis on ophthalmic devices," *JOSA A* **24**, 1250-1265 (2007).

130. D. J. Fechtig, B. Grajciar, T. Schmoll, C. Blatter, R. M. Werkmeister, W. Drexler, and R. A. Leitgeb, "Line-field parallel swept source MHz OCT for structural and functional retinal imaging," *Biomedical optics express* **6**, 716-735 (2015).
131. R. Douglas and N. Marshall, "A review of vertebrate and invertebrate ocular filters," in *Adaptive mechanisms in the ecology of vision* (Springer, 1999), pp. 95-162.
132. Y. C. Li, C. Strang, F. R. Amthor, L. Liu, Y. G. Li, Q. X. Zhang, K. Keyser, and X. C. Yao, "Parallel optical monitoring of visual signal propagation from the photoreceptors to the inner retina layers," *Opt Lett* **35**, 1810-1812 (2010).
133. X.-C. Yao, "Intrinsic optical signal imaging of retinal activation," *Japanese journal of ophthalmology* **53**, 327-333 (2009).
134. Z. Liu, K. Kurokawa, F. Zhang, J. J. Lee, and D. T. Miller, "Imaging and quantifying ganglion cells and other transparent neurons in the living human retina," *Proceedings of the National Academy of Sciences* **114**, 12803-12808 (2017).
135. A. Roorda, F. Romero-Borja, W. J. Donnelly III, H. Queener, T. J. Hebert, and M. C. Campbell, "Adaptive optics scanning laser ophthalmoscopy," *Optics express* **10**, 405-412 (2002).
136. M. Yamanaka, N. I. Smith, and K. Fujita, "Introduction to super-resolution microscopy," *Microscopy* **63**, 177-192 (2014).
137. D. Karadaglić and T. Wilson, "Image formation in structured illumination wide-field fluorescence microscopy," *Micron* **39**, 808-818 (2008).
138. J. H. Park, J. Y. Lee, and E. S. Lee, "Enhancing the isotropy of lateral resolution in coherent structured illumination microscopy," *Biomedical optics express* **5**, 1895-1912 (2014).
139. W. J. Donnelly and A. Roorda, "Optimal pupil size in the human eye for axial resolution," *JOSA A* **20**, 2010-2015 (2003).
140. C. A. Curcio, K. R. Sloan, R. E. Kalina, and A. E. Hendrickson, "Human photoreceptor topography," *Journal of comparative neurology* **292**, 497-523 (1990).
141. J. I. Yellott Jr, "Spectral analysis of spatial sampling by photoreceptors: topological disorder prevents aliasing," *Vision research* **22**, 1205-1210 (1982).
142. L. Sawides, A. de Castro, and S. A. Burns, "The organization of the cone photoreceptor mosaic measured in the living human retina," *Vision research* **132**, 34-44 (2017).

APPENDICES

UIC ACC and IRB approval for animal and human study:



Office of Animal Care and
Institutional Biosafety Committees (MC 672)
Office of the Vice Chancellor for Research
206 Administrative Office Building
1737 West Polk Street
Chicago, Illinois 60612-7227

March 3, 2015

Xincheng Yao
Bioengineering
M/C 063

Dear Dr. Yao:

The protocol indicated below was reviewed at a convened ACC meeting in accordance with the Animal Care Policies of the University of Illinois at Chicago on 12/16/2014. *The protocol was not initiated until final clarifications were reviewed and approved on 2/27/2015. The protocol is approved for a period of 3 years with annual continuation.*

Title of Application: Intrinsic Optical Signal Imaging of Retinal Function

ACC Number: 14-201

Initial Approval Period: 2/27/2015 to 12/16/2015

Current Funding: Portions of this protocol are supported by the funding sources indicated in the table below.

Number of funding sources: 3

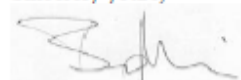
Funding Agency	Funding Title			Portion of Proposal Matched
NIH	Functional Imaging of Retinal Photoreceptors			All matched
Funding Number	Current Status	UIC PAF NO.	Performance Site	Funding PI
ROI EY023522 (years 1-5)	Pending	201503177	UIC	Xincheng Yao
Funding Agency	Funding Title			Portion of Proposal Matched
NIH	Super-Resolution Ophthalmoscopy for in Vivo Retinal Imaging			All matched
Funding Number	Current Status	UIC PAF NO.	Performance Site	Funding PI
ROI EY024628 (years 1-3)	Pending	201503176	UIC	Xincheng Yao
Funding Agency	Funding Title			Portion of Proposal Matched

<i>NSF- National Science Foundation</i>	<i>Simultaneous of Photoreceptor and Post-Photoreceptor Responses in the Retina</i>			<i>All matched</i>
Funding Number	Current Status	UIC PAF NO.	Performance Site	Funding PI
<i>CBET-1055889</i>	<i>Pending</i>	<i>201504507</i>	<i>UIC</i>	<i>Xincheng Yao</i>

This institution has Animal Welfare Assurance Number A3460.01 on file with the Office of Laboratory Animal Welfare (OLAW), NIH. This letter may only be provided as proof of IACUC approval for those specific funding sources listed above in which all portions of the funding proposal are matched to this ACC protocol.

In addition, all investigators are responsible for ensuring compliance with all federal and institutional policies and regulations related to use of animals under this protocol and the funding sources listed on this protocol. Please use OLAW's "What Investigators Need to Know about the Use of Animals" (<http://grants.nih.gov/grants/olaw/InvestigatorsNeed2Know.pdf>) as a reference guide. Thank you for complying with the Animal Care Policies and Procedures of UIC.

Sincerely yours,



Bradley Merrill, PhD
Chair, Animal Care Committee

BM/mbb

cc: BRL, ACC File, Jin-Hong (Robert) Chang, PAF 201503177, 20150317, 201504507



**Approval Notice
Amendment – Expedited Review
UIC Amendment # 5**

October 21, 2019

Xincheng Yao, PhD
Bioengineering
Phone: (312) 413-2016 / Fax: (312) 996-4644

RE: Protocol # 2016-0556
“Fundus photography employing trans-palpebral and trans-scleral illumination”

Dear Dr. Yao:

Please ensure you, the Principal Investigator; Felix Chau and Devrim Toslak have completed CITI Information Privacy and Security (IPS) Health Privacy (HIPAA) Basic Course, which is required because this study involves the use of protected health information. *Please refer to the UIC Policy regarding this mandatory requirement as of October 1, 2019.*

Appendix P form Please be kindly reminded that when adding new staff, please reflect the name(s) on the Appendix P with all of the currently approved project staff as well. *The Appendix P form should never only reflect the name(s) of the new staff being added.*

Your application was reviewed and approved on October 21, 2019. The amendment to your research may now be implemented.

Please note the following information about your approved amendment:

Amendment Approval Date: October 21, 2019

Amendment:

Summary: UIC Amendment #5 dated and received October 15, 2019, is an investigator initiated amendment involving the addition of Yiming Lu (grated access to OPRSLive) as Key Research Personnel. An Appendix P form was submitted.

Please be sure to:

- Use only the IRB-approved and stamped consent document(s) and/or HIPAA Authorization form(s) when enrolling subjects.
- Use your research protocol number (2016-0556) on any documents or correspondence with the IRB concerning your research protocol.

Page 1 of 2

UNIVERSITY OF ILLINOIS AT CHICAGO
Office for the Protection of Research Subjects

201 AOB (MC 672)
1737 West Polk Street
Chicago, Illinois 60612

Phone (312) 996-1711



→ Review and comply with the [policies](#) of the UIC Human Subjects Protection Program (HSPP) and the guidance [Investigator Responsibilities](#).

Please note that the IRB has the right to ask further questions, seek additional information, or monitor the conduct of your research and the consent process.

Please be aware that if the [scope of work](#) in the grant/project changes, the protocol must be amended and approved by the UIC IRB before the initiation of the change.

We wish you the best as you conduct your research. If you have any questions or need further help, please contact the OPRS at (312) 996-1711 or me at (312) 355-2939. Please send any correspondence about this protocol to OPRS via [OPRS Live](#).

Sincerely,

Jewell Hamilton, MSW
IRB Coordinator, IRB # 3
Office for the Protection of Research Subjects

cc: Thomas Royston, Bioengineering, M/C 063

Page 2 of 2

UNIVERSITY OF ILLINOIS AT CHICAGO
Office for the Protection of Research Subjects

201 AOB (MC 672)
1737 West Polk Street
Chicago, Illinois 60612

Phone (312) 996-1711

Permission to reuse Chapter II:


Author and End-User Reuse Policy

OSA's policies afford authors, their employers, and third parties the right to reuse the author's Accepted Manuscript (AM) or the final publisher Version of Record (VoR) of the article as outlined below:

Reuse purpose	Article version that can be used under:		
	Copyright Transfer	Open Access Publishing Agreement	CC BY License
Reproduction by authors in a compilation or for teaching purposes short term	AM	VoR	VoR
Posting by authors on arXiv or other preprint servers after publication (posting of preprints before or during consideration is also allowed)	AM	VoR	VoR
Posting by authors on a non-commercial personal website or closed institutional repository (access to the repository is limited solely to the institutions' employees and direct affiliates (e.g., students, faculty), and the repository does not depend on payment for access, such as subscription or membership fees)	AM	VoR	VoR
Posting by authors on an open institutional repository or funder repository	AM after 12 month embargo	VoR	VoR
Reproduction by authors or third party users for non-commercial personal or academic purposes (includes the uses listed above and e.g. creation of derivative works, translation, text and data mining)	Authors as above, otherwise by permission only. Contact copyright@osa.org .	VoR	VoR
Any other purpose, including commercial reuse on such sites as ResearchGate, Academia.edu, etc. and/or for sales and marketing purposes	By permission only. Contact copyright@osa.org .	By permission only. Contact copyright@osa.org	VoR

In addition, we allow authors to post their manuscripts on the Cornell University Library's arXiv site prior to submission to OSA's journals.

Permission to reuse Chapter IV:



Attribution-NonCommercial-NoDerivatives 4.0 International (CC BY-NC-ND 4.0)


This is a human-readable summary of (and not a substitute for) the [license](#). [Disclaimer](#).

You are free to:


Share — copy and redistribute the material in any medium or format

The licensor cannot revoke these freedoms as long as you follow the license terms.


Under the following terms:



Attribution — You must give [appropriate credit](#), provide a link to the license, and [indicate if changes were made](#). You may do so in any reasonable manner, but not in any way that suggests the licensor endorses you or your use.



NonCommercial — You may not use the material for [commercial purposes](#).



NoDerivatives — If you [remix, transform, or build upon](#) the material, you may not distribute the modified material.

No additional restrictions — You may not apply legal terms or [technological measures](#) that legally restrict others from doing anything the license permits.

Permission to reuse Chapter V:

SPIE. DIGITAL LIBRARY

CONFERENCE PROCEEDINGS

PAPERS


PRESENTATIONS

JOURNALS ▾

EBOOKS

HELP | ADVANCED SEARCH >

Search Digital Library



Creative Commons (CC BY 4.0)—Gold Open Access

For articles published under CC BY 4.0, users are free to share (copy, distribute, and transmit), to remix (adapt), and to make commercial use of the Article under the following conditions:

Attribution: Users must attribute the contribution in the manner specified by the author or licensor (but not in any way that suggests that they or their use of the Article is endorsed by the Author or licensor). See citation formatting [below](#).

Notice: For any reuse or distribution, users must make clear to others the license terms of this work, preferably using a link to the Creative Commons webpage.

The full legal code of the CC BY 4.0 license can be found at <http://creativecommons.org/licenses/by/4.0/legalcode>.

A human-readable summary of the CC BY 4.0 license is available at <https://creativecommons.org/licenses/by/4.0/>.

SPIE Copyright

For articles published under SPIE copyright, authors, or their employers in the case of works made for hire, retain the following rights:

- All proprietary rights other than copyright, including patent rights.
- The right to make and distribute copies of the Paper for internal purposes.
- The right to use the material for lecture or classroom purposes.
- The right to prepare derivative publications based on the Paper, including books or book chapters, journal papers, and magazine articles, provided that publication of a derivative work occurs subsequent to the official date of publication by SPIE.

Thus, authors may reproduce their original figures and text in new publications. The SPIE source publication should be referenced; see citation formatting [below](#).

Permission to reuse Fig. 1.1(A):

WEBVISION

The Organization of the Retina and Visual System

ABOUT/FAQ

Q: What is Webvision? **A:** Webvision was one of the first, if not *the* first online textbook. It has since evolved into an interactive, dynamic blog hosted on [WordPress](#) that covers all things related to the bioscience of the visual system.

Q: Can I use images and/or content from Webvision? What is the copyright? **A:** All copyright for chapters belongs to the individual authors who created them. However, for non-commercial, academic purposes, images and content from the [chapters portion of Webvision](#) may be used with a non-exclusive rights under a Attribution, Noncommercial 4.0 International ([CC BY-NC](#)) Creative Commons license. Cite Webvision, <http://webvision.med.utah.edu/> as the source. Commercial applications need to obtain license permission from the administrator of Webvision and are generally declined unless the copyright owner can/wants to donate or license material. Use online should be accompanied by a link back to the original source of the material. All imagery or content associated with [blog posts](#) belong to the authors of said posts, except where otherwise noted.

Permission to reuse Figs. 1.1(B) and 1.1(C):

License Number	4705151161533
License date	Nov 09, 2019
Licensed Content Publisher	Springer Nature
Licensed Content Publication	Nature Reviews Neuroscience
Licensed Content Title	Transcriptional regulation of photoreceptor development and homeostasis in the mammalian retina
Licensed Content Author	Anand Swaroop et al
Licensed Content Date	Aug 1, 2010
Type of Use	Thesis/Dissertation
Requestor type	academic/university or research institute
Format	print and electronic
Portion	figures/tables/illustrations
Number of figures/tables/illustrations	2
High-res required	no
Will you be translating?	no
Circulation/distribution	1 - 29
Author of this Springer Nature content	no
Title	Quantitative investigation of stimulus-evoked intrinsic optical signal responses in retinal photoreceptors
Institution name	University of Illinois at Chicago
Expected presentation date	Dec 2019
Portions	Figure 1
Requestor Location	Yiming Lu 1905 W Taylor St Chicago, IL 60608 United States Attn:
Total	0.00 USD

Permission to reuse Fig. 1.2(A):

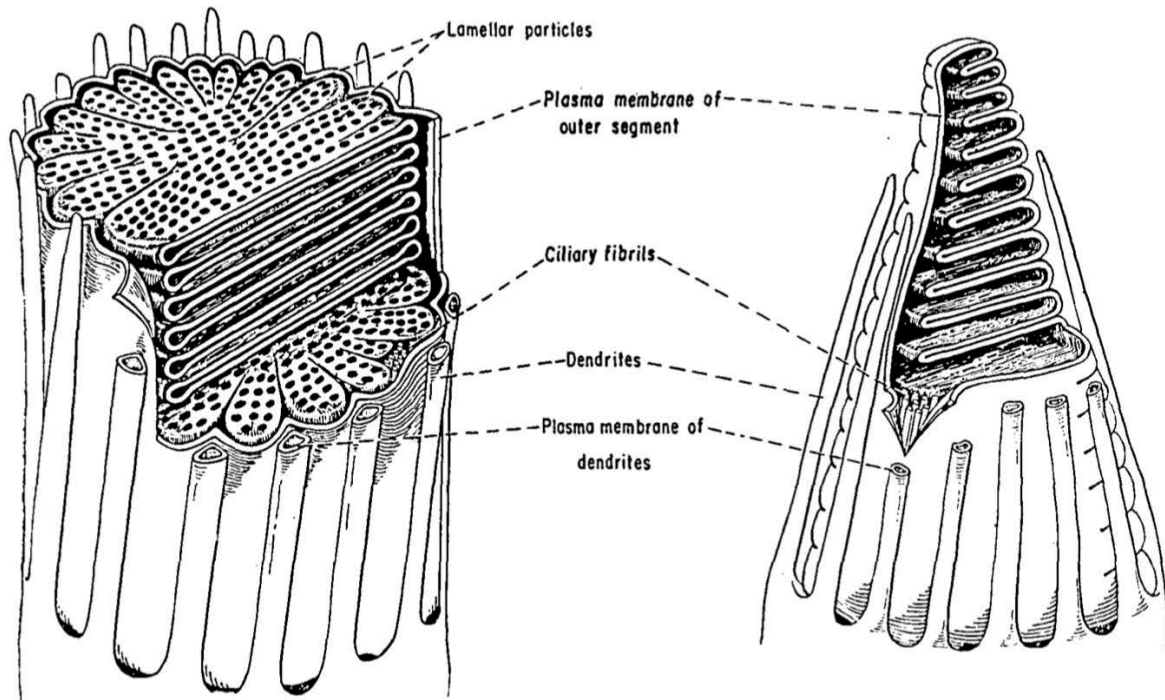


Fig. 13

Citation

George Wald, Paul K. Brown, Ian R. Gibbons, "The Problem of Visual Excitation," J. Opt. Soc. Am. **53**, 20-35 (1963); <https://www.osapublishing.org/josa/abstract.cfm?URI=josa-53-1-20>



Image © 1963 Optical Society of America and may be used for noncommercial purposes only. Report a [copyright concern regarding this image](#).

OSA[®]
The Optical Society


Permission to reuse Fig. 1.2.(B):

License Number	4705170119463
License date	Nov 10, 2019
Licensed Content Publisher	John Wiley and Sons
Licensed Content Publication	Journal of Comparative Neurology
Licensed Content Title	Disc morphogenesis in vertebrate photoreceptors
Licensed Content Author	Don H. Anderson, Steven K. Fisher, Roy H. Steinberg
Licensed Content Date	Oct 9, 2004
Licensed Content Volume	190
Licensed Content Issue	3
Licensed Content Pages	18
Type of Use	Dissertation/Thesis
Requestor type	University/Academic
Format	Print and electronic
Portion	Figure/table
Number of figures/tables	1
Original Wiley figure/table number(s)	Figure 1
Will you be translating?	No
Title of your thesis / dissertation	Quantitative investigation of stimulus-evoked intrinsic optical signal responses in retinal photoreceptors
Expected completion date	Dec 2019
Expected size (number of pages)	1
Requestor Location	Yiming Lu 1905 W Taylor St Chicago, IL 60608 United States Attn: EU826007151
Publisher Tax ID	
Total	0.00 USD

Permission to reuse Fig. 1.3:

File information	Structured data
<div>Captions Edit</div> <div>English Add a one-line explanation of what this file represents</div>	
Description	Representation of molecular steps in photoactivation (modified from Leskov et al., 2000). Depicted is an outer membrane disk in a rod. Step 1: Incident photon (hv) is absorbed and activates a rhodopsin by conformational change in the disk membrane to R*. Step 2: Next, R* makes repeated contacts with transducin molecules, catalyzing its activation to G* by the release of bound GDP in exchange for cytoplasmic GTP. The α and γ subunits Step 3: G* binds inhibitory γ subunits of the phosphodiesterase (PDE) activating its α and β subunits. Step 4: Activated PDE hydrolyzes cGMP. Step 5: Guanylyl cyclase (GC) synthesizes cGMP, the second messenger in the phototransduction cascade. Reduced levels of cytosolic cGMP cause cyclic nucleotide gated channels to close preventing further influx of Na ⁺ and Ca ²⁺ .
Date	10 December 2007
Source	http://en.wikipedia.org/wiki/File:Phototransduction.png
Author	Jason J. Corneveaux, wiki user: Caddymob (talk)
Permission (Reusing this file)	<p>I, the copyright holder of this work, hereby publish it under the following licenses:</p> <div>  <p>Permission is granted to copy, distribute and/or modify this document under the terms of the GNU Free Documentation License, Version 1.2 or any later version published by the Free Software Foundation; with no Invariant Sections, no Front-Cover Texts, and no Back-Cover Texts. A copy of the license is included in the section entitled GNU Free Documentation License.</p> </div> <div> <p>This file is licensed under the Creative Commons Attribution 3.0 Unported license.</p> <div>  <p>CC SOME RIGHTS RESERVED</p> </div> <p>You are free:</p> <ul style="list-style-type: none"> • to share – to copy, distribute and transmit the work • to remix – to adapt the work <p>Under the following conditions:</p> <ul style="list-style-type: none"> • attribution – You must give appropriate credit, provide a link to the license, and indicate if changes were made. You may do so in any reasonable manner, but not in any way that suggests the licensor endorses you or your use. <p><i>You may select the license of your choice.</i></p> </div>
Other versions	Derivative works of this file: Phototransduction uk.png

Permission to reuse Fig. 1.4:



Confirmation Number: 11859361
Order Date: 10/14/2019

Customer Information

Customer: Yiming Lu
Account Number: 3001535736
Organization: Yiming Lu
Email: ylu33@uic.edu
Phone: +1 (312) 996-6040
Payment Method: Invoice

This is not an invoice

Order Details

JOURNAL OF GENERAL PHYSIOLOGY. ONLINE

Billing Status:
N/A

Order detail ID:	72043441	Permission Status:	✔ Granted
ISSN:	1540-7748	Permission type:	Republish or display content
Publication Type:	Journal	Type of use:	Thesis/Dissertation
Volume:		Order License Id:	4687840382168
Issue:		Requestor type	Academic institution
Start page:		Format	Print, Electronic
Publisher:	ROCKEFELLER UNIVERSITY PRESS	Portion	image/photo
Author/Editor:	Society of General Physiologists	Number of images/photos requested	1
		The requesting person/organization	Yiming Lu
		Title or numeric reference of the portion(s)	Figure 3. ERG waveform
		Title of the article or chapter the portion is from	Introduction
		Editor of portion(s)	NA
		Author of portion(s)	Yiming Lu
		Volume of serial or monograph	NA
		Page range of portion	NA
		Publication date of portion	NA
		Rights for	Main product
		Duration of use	Life of current edition
		Creation of copies for the disabled	no
		With minor editing privileges	no
		For distribution to	Worldwide
		In the following language(s)	Original language of publication
		With incidental promotional use	no
		Lifetime unit quantity of new product	Up to 499
		Title	Quantitative investigation of stimulus-evoked intrinsic optical signal responses in retinal photoreceptors
		Institution name	University of Illinois at Chicago
		Expected presentation date	Dec 2019

Note: This item was invoiced separately through our [RightsLink service](#). [More info](#)

\$ 0.00

Total order items: 1

Order Total: \$0.00

Permission to reuse Fig. 1.5(A):

License Number	4705190147579
License date	Nov 10, 2019
Licensed Content Publisher	Springer Nature
Licensed Content Publication	Springer eBook
Licensed Content Title	Functional Imaging of Retinal Photoreceptors and Inner Neurons Using Stimulus-Evoked Intrinsic Optical Signals
Licensed Content Author	Xin-Cheng Yao, Yi-Chao Li
Licensed Content Date	Jan 1, 2012
Type of Use	Thesis/Dissertation
Requestor type	academic/university or research institute
Format	print and electronic
Portion	figures/tables/illustrations
Number of figures/tables/illustrations	1
Will you be translating?	no
Circulation/distribution	1 - 29
Author of this Springer Nature content	no
Title	Quantitative investigation of stimulus-evoked intrinsic optical signal responses in retinal photoreceptors
Institution name	University of Illinois at Chicago
Expected presentation date	Dec 2019
Portions	Figure 2
Requestor Location	Yiming Lu 1905 W Taylor St Chicago, IL 60608 United States Attn:
Total	0.00 USD
Terms and Conditions	

Permission to reuse Figs. 1.6:

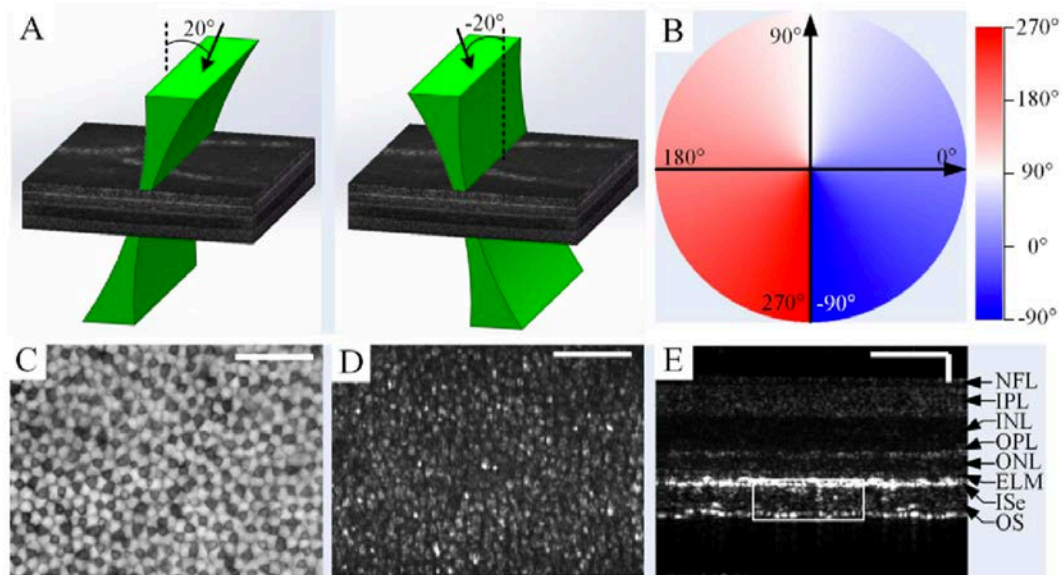


Fig. 2.

Citation

Benquan Wang, Qiuxiang Zhang, Rongwen Lu, Yanan Zhi, Xincheng Yao, "Functional optical coherence tomography reveals transient phototropic change of photoreceptor outer segments," Opt. Lett. **39**, 6923-6926 (2014);
<https://www.osapublishing.org/ol/abstract.cfm?URI=ol-39-24-6923>

Image © 2014 Optical Society of America and may be used for noncommercial purposes only. Report a [copyright concern regarding this image](#).

OSA[®]
The Optical Society

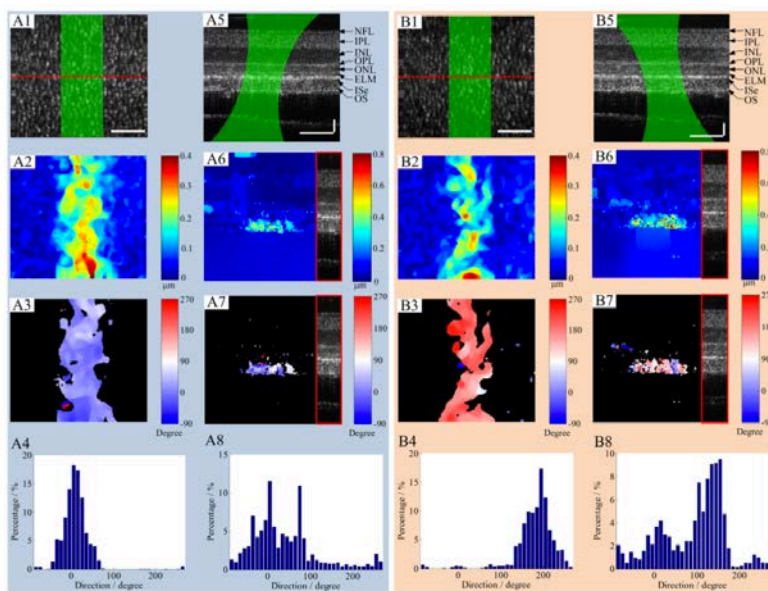


Fig. 3.

Citation

Benquan Wang, Qiuxiang Zhang, Rongwen Lu, Yanan Zhi, Xincheng Yao, "Functional optical coherence tomography reveals transient phototropic change of photoreceptor outer segments," Opt. Lett. **39**, 6923-6926 (2014);
<https://www.osapublishing.org/ol/abstract.cfm?URI=ol-39-24-6923>

Image © 2014 Optical Society of America and may be used for noncommercial purposes only. Report a [copyright concern regarding this image](#).

OSA[®]
The Optical Society

VITA

NAME: YIMING LU

EDUCATION: M.S., BIOMEDICAL ENGINEERING, TIANJIN UNIVERSITY (2014)
B.E., BIOMEDICAL ENGINEERING, TIANJIN UNIVERSITY (2011)

AWARDS: CCTS PRE-DOCTORAL EDUCATION FOR CLINICAL AND TRANSLATIONAL SCIENTISTS FELLOWSHIP, UIC (2018)

PUBLICATIONS: Y. LU, T. H. KIM, AND X. YAO. COMPARATIVE STUDY OF WILD-TYPE AND RD10 MICE REVEALS TRANSIENT INTRINSIC OPTICAL SIGNAL RESPONSE BEFORE PHOSPHODIESTERASE ACTIVATION IN RETINAL PHOTORECEPTORS. EXPERIMENTAL BIOLOGY AND MEDICINE (ACCEPTED, 2019)

Y. LU, C. LIU, AND X. YAO. IN VIVO SUPER-RESOLUTION IMAGING OF TRANSIENT RETINAL PHOTOTROPISM EVOKED BY OBLIQUE LIGHT STIMULATION. JOURNAL OF BIOMEDICAL OPTICS 23(5), 050502. (2018)

Y. LU, J. BENEDETTI, AND X. YAO. LIGHT-INDUCED LENGTH SHRINKAGE OF ROD PHOTORECEPTOR OUTER SEGMENTS. TRANSLATIONAL VISION SCIENCE & TECHNOLOGY 7(6), 29-29 (2018)

Y. LU, B. WANG, D. R. PEPPERBERG, AND X. YAO. STIMULUS-EVOKED OUTER SEGMENT CHANGES OCCUR BEFORE THE HYPERPOLARIZATION OF RETINAL PHOTORECEPTORS. BIOMEDICAL OPTICS EXPRESS 8(1), 38-47 (2017)

X. YAO, T. SON, T. H. KIM, AND Y. LU, FUNCTIONAL OPTICAL COHERENCE TOMOGRAPHY OF RETINAL PHOTORECEPTORS. EXPERIMENTAL BIOLOGY AND MEDICINE 243: 1254–1262 (2018)

T. SON, M. ALAM, D. TOSLAK, B. WANG, Y. LU, AND X. YAO. FUNCTIONAL OPTICAL COHERENCE TOMOGRAPHY OF NEUROVASCULAR COUPLING INTERACTIONS IN THE RETINA. JOURNAL OF BIOPHOTONICS E201800089 (2018)

T. H. KIM, T. SON, Y. LU, M. ALAM, AND X. YAO, COMPARATIVE OPTICAL COHERENCE TOMOGRAPHY

ANGIOGRAPHY OF WILD-TYPE AND RD10 MOUSE RETINAS. TRANSLATIONAL VISION SCIENCE & TECHNOLOGY 7(6), 42 (2018)

D. THAPA, B. WANG, Y. LU, T. SON, AND X. YAO. ENHANCEMENT OF INTRINSIC OPTICAL SIGNAL RECORDING WITH SPLIT SPECTRUM OCT. JOURNAL OF MODERN OPTICS 64(17), 1800-1807 (2017)

T. SON, B. WANG, D. THAPA, Y. LU, Y. CHEN, D. CAO, AND X. YAO. OPTICAL COHERENCE TOMOGRAPHY ANGIOGRAPHY OF STIMULUS-EVOKED HEMODYNAMIC RESPONSES IN INDIVIDUAL RETINAL LAYERS. BIOMEDICAL OPTICS EXPRESS 7(8), 3151-3162 (2016)

B. WANG, Y. LU, AND X. YAO. IN VIVO OPTICAL COHERENCE TOMOGRAPHY OF STIMULUS-EVOKED INTRINSIC OPTICAL SIGNALS IN MOUSE RETINAS. JOURNAL OF BIOMEDICAL OPTICS 21(9), 096010 (2016)

C. LIU, Y. ZHI, B. WANG, D. THAPA, M. ALAM, Y. LU AND X. YAO. IN VIVO SUPER-RESOLUTION RETINAL IMAGING THROUGH VIRTUALLY STRUCTURED DETECTION. JOURNAL OF BIOMEDICAL OPTICS 21(12), 120502-120502 (2016)

X. ZHAO, D. THAPA, B. WANG, Y. LU, S. GAI, X. YAO. STIMULUS-EVOKED OUTER SEGMENT CHANGES IN ROD PHOTORECEPTORS. JOURNAL OF BIOMEDICAL OPTICS 21(6), 065006 (2016)

PRESENTATIONS: YIMING LU, BENQUAN WANG, XINCHENG YAO. COMPARATIVE INVESTIGATION OF STIMULUS-EVOKED ROD OUTER SEGMENT MOVEMENT AND RETINAL ELECTROPHYSIOLOGICAL ACTIVITY. SPIE PHOTONICS WEST. SAN FRANCISCO, CA. FEBRUARY 2017

YIMING LU, CHANGGENG LIU, XINCHENG YAO. IN VIVO SUPER-RESOLUTION IMAGING OF STIMULUS-EVOKED TRANSIENT RETINAL PHOTORECEPTOR MOVEMENT IN RANA PIPIENS. ARVO IMAGING IN THE EYE CONFERENCE. BALTIMORE, MD. MAY 2017.